ABSTRACT

MODELING, DESIGN AND FABRICATION OF THIN-FILM MICROCRYSTALLINE SILICON SOLAR CELLS

by
Wei Chen

The modeling, design and fabrication of low-cost thin-film microcrystalline silicon(μc-Si) solar cells is studied in this thesis. The cell, considered in this investigation, utilizes low-cost glass as the substrate and microcrystalline Si (μc-Si) as the active layer. A comprehensive refractive index (n) and extinction coefficient (k) model of silicon as function of doping, temperature and wavelength is developed to assist the optical design of the cell. In order to obtain acceptable short circuit current density (Jsc) from the cell, it is found that the thickness of the silicon thin film should be more than 10μm. To get the best light trapping effect, the surface of the cell should be double-side or front-side textured. The density of the texture pits should be as high as possible and the bottom angle of the texture pits should be as small as possible. However, the depth of the texture pits does not have too much influence on the overall performance of the cell.

A model and corresponding software are developed to investigate the electronic properties of the material /device built using low cost μc-Si. This model divides the defect regions inside the material into different categories according to the defect levels in them. Therefore, this model is able to deal with various kinds of defects and defect clusters. The software uses finite element method to solve time-dependent continuity equations with different boundary conditions to get the carrier distribution inside the materials and hence the I-V characteristics of the devices. It is found that, to get

satisfying thin film μc-Si thin film cell, the grain size of the film should be about 10μm, and the surface recombination velocities at the grain boundaries should be less than 1000cm/s. The requirement on the minority carrier lifetime is not rigid because of better tolerance of thin-film solar cells to this property.

Some critical fabrication steps in making such a thin film solar cell are also investigated. An Al-involved crystallization / grain enhancement procedure using optical processing is used to get large-grain μc-Si thin films. This process involves both a-Si/Al reaction and Al diffusion inside Si. It can produce μc-Si at temperatures lower than the softening point of low-cost glass within a much shorter duration compared with other crystallization / grain enhancement techniques. Crystallization of Si film can start at temperatures as low as 200°C when Al is involved. However, to get strong crystallization and grain enhancement, the processing temperature should be more than 450°C. At temperature around 500°C, the crystallization becomes much stronger. The local melting at the Si-Al interface may cause this crystallization.

MODELING, DESIGN AND FABRICATION OF THIN-FILM MICROCRYSTALLINE SILICON SOLAR CELLS

by

Wei Chen

A Dissertation
Submitted to the Faculty of
New Jersey Institute of Technology and
Rutgers, The State University of New Jersey - Newark
in Partial Fulfillment of the Requirements for the Degree of
Doctor of Philosophy in Applied Physics

Federated Physics Department

May 2000

APPROVAL PAGE

MODELING, DESIGN AND FABRICATION OF THIN FILM MICROCRYSTALLINE SILICON SOLAR CELLS

Wei Chen

Dr. Nuggehalli M. Ravindra, Dissertation Advisor — Date
Professor of Physics, NJIT

Dr. Bhushan L. Sopori. Dissertation Advisor — Date
Principal Engineer, National Renewable Energy Laboratory, Golden, CO

Dr. William Savin, Committee Member — Date
Professor of Physics, NJIT

Dr. Earl Shaw, Committee Member — Date
Professor, Chairman of Physics Department, Rutgers University, Newark, NJ

Dr. John Federici, Committee Member — Date
Associate Professor of Physics, NJIT

Dr. Oktay Gokce, Committee Member — Date
Research Professor of Physics, NJIT

BIOGRAPHICAL SKETCH

Author: Wei Chen

Degree: Doctor of Philosophy in Applied Physics

Date: May, 2000

Undergraduate and Graduate Education:

- Doctor of Philosophy in Applied Physics,
  New Jersey Institute of Technology, Newark, NJ, 2000

- Master of Science in Physics,
  Nankai University, Tianjin, China, 1994

- Bachelor of Science in Physics,
  Nankai University, Tianjin, China, 1991

Major: Applied Physics

Publications:

1. Bhushan Sopori and Wei Chen, "Influence of distributed defects on the photoelectric characteristics of a large-area device", Journal of Crystal Growth, 210, pp. 375-378 (2000).

2. Bhushan Sopori, Wei Chen, Yi Zhang and Jamal Madjdpour, "High-speed mapping of grown-in defects and their influence in large-area silicon photovoltaic devices," Journal of Crystal Growth, 210, pp. 346-350 (2000).

3. Bhushan Sopori, Wei Chen, Jamal Madjdpour, N. M. Ravindra, "Calculation of Eissivity of Si Wafers," Journal of Electronic Materials, Vol. 28, pp.1385-1389. (1999).

4. Bhushan Sopori, Yi Zhang, Wei Chen, "Process Monitoring in Solar Cell Manufacturing," Ninth Workshop on Crystalline Silicon Solar Cell Materials and Processes, Extended Abstracts and Papers from the Workshop, pp. 74-80, Breckenridge, Colorado(August 1999).

5. Bhushan Sopori, Wei Chen, Yi Zhang, Tess Hemschoot, Jamal Madjdpour, "Extending PVSCAN to Meet the Market Needs for High-Speed, Large-Area Scanning," Ninth Workshop on Crystalline Silicon Solar Cell Materials and Processes, Extended Abstracts and Papers from the Workshop, pp. 135-141, Breckenridge, Colorado(August 1999).

6. N. M. Ravindra, Bhushan Sopori, S. Abedrabbo, Wei Chen, J. C Hensel, A. T. Fiory, "Emissivity Measurements and Modeling in Silicon -- Some Observations," Ninth Workshop on Crystalline Silicon Solar Cell Materials and Processes, Extended Abstracts and Papers from the Workshop, pp. 213-217, Breckenridge, Colorado(August 1999).

7. Bhushan Sopori, Jamal Madjdpour, Yi Zhang, Wei Chen, "PV Optics: An Optical Modeling Tool for Solar Cell and Module Design," Kapur, V. K., et al., eds. Photovoltaics for the 21st Century: Proceedings of the Electrochemical Society International Symposium, Seattle, Washington. Electrochemical Society Proceedings Vol. 99-11, pp. 138-144.(May 1999)

8. Wei Chen, Bhushan Sopori, "Thin Silicon Solar Cell on Glass: Cell Design and Process Physics," V. K. Kapur, et al., eds. Photovoltaics for the 21st Century: Proceedings of the Electrochemical Society International Symposium, Seattle, Washington. Electrochemical Society Proceedings Vol. 99-11 pp. 145-152, (May 1999).

9. Bhushan Sopori, Wei Chen, Jamal Madjdpour, "Emissivity of Bare and Coated Si Wafers: Theoretical Studies," Proceedings of 195th ECS annual meeting, Seattle; WA (May 1999).

10. N. M. Ravindra, S. Abedrabbo, W. Chen, F. M. Tong, A. K. Nanda, A.C. Speranza, "Temperature-Dependent Emissivity of Silicon –Related Materials and Structures," IEEE Transactions on Semiconductor Manufacturing, vol. 11, No. 1(1998).

11. Bhushan Sopori, Wei Chen, Yi Zhang, "Development of a Thin-Film Crystalline-Silicon Solar Cell," AIP CONFERENCE PROCEEDINGS 0094-243X 1999, ISSUE 462, Edited by: Al-Jassim, M., Thornton, J. P., Gee, J. M., pp. 437-442 National Center for Photovoltaics 15th photovoltaics program review meeting; Denver, CO(Sep., 1998).

12. Bhushan Sopori, Wei Chen, T. Tan, P. Plekhanov, "Overcoming the Efficiency-Limiting Mechanisms in Commercial Si Solar Cells," AIP CONFERENCE PROCEEDINGS 0094-243X 1999, ISSUE 462, Edited by: Al-Jassim, M.; Thornton, J. P.; Gee, J. M., pp. 341-347, National Center for Photovoltaics 15th photovoltaics program review meeting; Denver, CO(Sep., 1998).

13. Bhushan Sopori, Jamal Madjdpour, Wei Chen, Yi Zhang, "Light-Trapping in a-Si Solar Cells: Summary of the Results from PV Optics," AIP CONFERENCE

PROCEEDINGS 0094-243X 1999, ISSUE 462, Edited by: Al-Jassim, M., Thornton, J. P., Gee, J. M, pp. 291-296, National Center for Photovoltaics 15th photovoltaics program review meeting; Denver; CO(Sep., 1998).

14. Bhushan Sopori, Jamal Madjdpour, Yi Zhang, Wei Chen, S. Guha, J. Yang, A. Banerjee, S. Hegedus, "Optical Modeling of a-Si Solar Cells," Branz, H. M., et al., eds. Amorphous and Heterogeneous Silicon Thin Films: Fundamentals to Devices, Materials Research Society Symposium Proceedings, Vol. 557, pp. 755-760.(Apr., 1998).

15. Bhushan Sopori, Wei Chen, N. M. Ravindra, S. Abedrabbo, "Modeling emissivity of rough and textured silicon wafers," Journal of Electronic Materials, vol. 27, no.12. pp. 1341-6 (1998).

16. Bhushan Sopori, Jamal Madjdpour, Wei Chen, "On the Performance Limiting Behavior of Defect Clusters in Commercial Silicon Solar Cells," Proceeding of 2nd World Conference on Photovoltaic solar energy conversion, edited by Schmid, J., pp. 152-155, Vienna, Austria (1998).

17. Bhushan Sopori, Jamal Madjdpour, Wei Chen, "Applications of "PV Optics" for Solar Cell and Module Design," J. Schmid, et al., eds. 2nd World Conference on Photovoltaic Solar Energy Conversion: Proceedings of the International Conference, pp. 156-159, Vienna, Austria(1998).

18. Bhushan Sopori, Wei Chen, Karen Nemire, J. Gee, S. Ostapenko, "Influence of Defect Clusters on the Performance of Silicon Solar Cells," S. Ashok, et al., eds. Defect and Impurity Engineered Semiconductors and Devices II, Materials Research Society Symposium Proceedings, Vol. 510, pp. 505-510, San Francisco, CA (Apr., 1998).

19. Bhushan Sopori, Wei Chen, N. M. Ravindra, "Theoretical Analysis of the Minority Carrier Lifetime in a Multicrystalline Wafer With Spatially Varying Defect Distribution," 2nd Symposium on Defect and impurity engineering semiconductors and devices, Materials Research Society Symposium Proceedings, Vol. 510, pp. 373-380, San Francisco, CA (Apr., 1998).

20. Bhushan Sopori, Wei Chen, Martha Symko, "Spatial Nonuniformities in the Minority-Carrier Diffusion Length/Lifetime: Measurement and Implications on a Large- Area Device Performance," Proceedings of Advanced workshop on Silicon recombination lifetime characterization methods, Edited by Gupta, D. C.; Bacher, F. R.; Hughes, W. M., pp. 328-346 (1998).

21. S. A.bedrabbo, J. C. Hensel, A.T.Fiory, B. Sopori, W. Chen, N. M. Ravindra, "Perspectives on Emissivity Measurements and Modeling in Silicon," Materials Science in Semiconductor Processing, vol. 1, 187-193 (1998).

22. Bhushan Sopori, Wei Chen, Jamal Madjdpour, Martha Symko, "A Thin-Film Silicon Solar Cell: Design and Processing Approach," Thin-film structures for photovoltaics, Materials Research Society Symposium Proceedings, vol. 485, edited by Jones, E. D., pp. 101-106, Boston; MA (Dec, 1997).

23. Bhushan Sopori, Jeff Alleman, Wei Chen, Teh Y. Tan, "Grain Enhancement of Thin Silicon Layers Using Optical Processing," 6th Rapid thermal and integrated processing, Materials Research Society Symposium Proceedings, vol. 470, edited by Riley, T. J., pp. 419-424, San Francisco; CA (Apr. 1997).

24. Bhushan Sopori, Jamal Madjdpour, Bolko von Roedern, Wei Chen, Steve. S. Hegedus, "Optical Losses in Amorphous Silicon Solar Cells due to Back Reflectors," S. Wagner, et al., eds. Amorphous and Microcrystalline Silicon Technology 1997, Proceedings of the Materials Research Society Symposium. Vol. 467, pp. 777-782, San Francisco, California.(April, 1997).

25. S. Adedrabbo, N.M. Ravindra, W.Chen, V.Rajasekhar, T. Golta, and O. H. Gpkce, "Temperature Dependent Emissivity of Multilayers on Silicon," 6th Rapid thermal and integrated processing, Materials Research Society Symposium Proceedings, vol. 470, edited by Riley, T. J., pp. 419-424, San Francisco; CA (Apr. 1997)pp. 69-80, Anaheim; CA (1996).

26. W. Chen, M. Oh, S. Abedrabbo, F.M.Tong, W. Schmidt, S. Naraynan, B. Sopori, and N. M. Ravindra, "Emissivity Studies on Polycrystalline Silicon and a-Si/SiO2/Si," Proceeding of Symposium on Transient thermal processing techniques in electronic materials, edited by N. M. Ravindra and R. K. Singh, pp. 81-90, Anaheim; CA (1996).

27. N. M. Ravindra, Wei Chen, Tong, F.-M., Nanda, A., "Emissivity Measurments and Modeling - An Overview," Transient Thermal Processing Techniques in Electronic Materials, Proceeding of Symposium on Transient thermal processing techniques in electronic materials, edited by N.M.Ravindra and R.K.Singh, pp 159-165, Anaheim, CA (1996).

To my beloved family

ACKNOWLEDGEMENT

I wish to express my sincere gratitude to my advisors, Dr. Bhushan Sopori and Professor N. M. Ravindra, who introduced me to the exciting field of semiconductor materials and devices. They have taught me so many things that will be beneficial to me in my whole life. Their friendship and moral support are among the most important resources I relied on during these years.

Special thanks to Professors William Savin, Earl Shaw, John Federici, and Oktay Gokce for serving as members of the committee.

The author is grateful to U.S. Department of Energy Photovoltaic Center of Excellence, for sponsoring this research through sucontract No. DE-Ac36-83CH10093 to NJIT.

I appreciate the friendship, help and suggestions from many people involved in this research, including Anna Duda, Robert Reedy, Rick Maston, Kim Jones and Jamal Madjpour from NREL, Roger Aparicio from Institute of Energy Conversion, University of Delaware, Scott Morrison from MVSystem, Sufian Abedrabbo, Feiming Tong and Yi Zhang from NJIT.

TABLE OF CONTENTS

Chapter **Page**

1 INTRODUCTION 1

2 SI THIN FILM SOLAR CELLS: AN OVERVIEW 10

2.1 Introduction 10

2.2 Some general issues on thin film Si solar cells 11

2.3 Some detailed examples of thin film solar cells 17

2.4 NREL design of thin-film μc-Si solar cell 22

3 OPTICAL DESIGN OF NREL THIN FILM SILICON SOLAR CELLS 24

3.1 Introduction 24

3.2 Methodology 27

3.2.1 A brief description of PV optics 27

3.2.2 Optical properties of Si 30

3.3 The optical design of the cell 35

3.3.1 What will happen when the thin film is used? 35

3.3.2 The surface condition and the thickness 37

3.3.3 More detailed study on texturing 39

3.4 From optical model to electronic model: A discussion 44

3.5 Conclusions 44

4 ELECTRICAL MODELING / DESIGN OF SOLAR CELLS ON NON-PERFECT MATERIALS 45

4.1 Introduction 45

4.2 Defects in PV materials 48

TABLE OF CONTENTS
(Continued)

Chapter **Page**

4.3 Electronic properties of defects 50

4.3.1 Extra Energy Levels Caused by Grain Boundaries 52

4.3.2 Extra energy levels introduced by impurities 54

4.3.3 When the defects are clustered 57

4.3.4 Recombination centers and Traps: 57

4.3.5 Summary–A general picture of defect energy trapping level in PV Si 57

4.4 Minority carriers lifetime study of large area defected materials 59

4.4.1 Introduction 59

4.4.2 Methodology 60

4.4.3 Results and discussion 66

4.5 Effects of defects on the p-n junction 80

4.6 Modeling of the defects in Solar Cells 82

4.6.1 The model 82

4.6.2 Programming 83

4.6.3 Results and discussion 84

4.7 Summary – The least-acceptable material quality of our cells 91

5 FABRICATION OF μC-SI FILM SOLAR CELLS 92

5.1 Introduction 92

5.2 Overview of crystallization techniques 94

5.2.1 Direct Growth of Poly-Si thin films: 94

5.2.2 Grain Enhancement of a-Si thin films: 94

TABLE OF CONTENTS
(Continued)

Chapter **Page**

5.3 Experimental details 98

5.3.1 Processing equipment configuration 98

5.3.2 As-deposited samples structures 101

5.3.3 Processing procedures 101

5.3.4 Characterization of materials 102

5.3.5 Testing-Device formation and characterization 103

5.4 Al-involved mc-Si fabrication at NREL 104

5.4.1 The properties of samples before processing 104

5.4.2 The starting point of crystallization 107

5.4.3 The change of the peaks after processing 108

5.4.4. The effect of high temperatures 110

5.4.5 The effect of thin film quality 117

5.4.6 Summary of experimental results 117

5.5 Discussion: The mechanisms involved in Al induced crystallization 119

5.6 The primary device performance 122

6 CONCLUSIONS AND FUTURE WORK 125

REFERENCES 129

LIST OF TABLES

Table **Page**

Table 2.1. Summary of thin silicon solar cell fabrication methods and performance..10

Table 2.2. Summary of μc-Si growth techniques..... 14

Table 2.3. Some parameters of "STAR" structure thin film solar cell..... 21

Table 4.1. The parameters used in first set of calculation..... 83

Table 4.2. The parameters used in second set of calculation 85

Table 5.1. Comparison of different crystallization methods 96

Table 5.2. The as deposited sample structures 100

Table 5.3. Intensities of different peaks in XRD spectrums of processed HW161-XX samples 110

Table 5.4. Intensities of different peaks in XRD spectrums of processed HW164-XX samples 112

Table 5.5. Intensities of different peaks in XRD spectrums of processed HW165-XX samples 115

Table 5.6. Measured Voc of different devices on different samples 122

LIST OF FIGURES

Figure		Page
Figure 1.1.	Schematic representation of a single p-n junction solar cell.	2
Figure 1.2.	A schematic showing the typical I-V character of a solar cell. The area (in I-V space) of the shaded region is the maximum power the cell can output.	3
Figure 1.3.	The schematic of NREL thin film μc-Si solar cell.	8
Figure 2.1	A schematic showing the structure and fabrication procedures of ZMR solar cell.	17
Figure 2.2.	A schematic showing Martin Green's multi-junction solar cell.	19
Figure 2.3.	A schematic showing "STAR" structure cell.	20
Figure 3.1	Comparison of the transmitted AM1.5 photon flux through a 500-mm-thick Si wafer and a 10-mm-thick wafer. Also shown in the Figure is the photon flux of AM1.5 spectrum.	24
Figure 3.2.	A schematic shows the algorithm PVoptics calculating the optical properties of multi-layer structures.	27
Figure 3.3.	A comparison of the calculated and the measured reflectance – (a), transmittance,- (b) and absorbance – (c), for two samples of different dopant concentrations. The dotted and the solid lines correspond to measured and calculated data, respectively. Wafer thickness = 350 μm	33
Figure 3.4.	Comparison of our calculation results of emissivity and Sato's experimental data.	34
Figure 3.5	The calculated MACD and Metal Loss as functions of cell thickness for double-side polished Si solar cell show in Figure 3.6.	35
Figure 3.6.	The structure of the double-side polished cell used in the calculation.	35
Figure 3.7.	Calculated optical properties of a single junction cell under different surface configurations. The cell structures are shown in the inlet of figures.	37
Figure 3.8.	Calculated MACD vs. Thickness at different surface configurations shown in the inlet of the figure.	38

LIST OF FIGURES
(Continued)

Figure **Page**

Figure 3.9. Calculated Metal loss vs. thickness for different surface configurations. 38

Figure 3.10. The geometry and the terminology used in the texture shape study. . 39

Figure 3.11. The calculated MACD as a function of the height of texture pits. 40

Figure 3.12. The calculated MACD as a function of the bottom angle of texture pits. 41

Figure 3.13. Calculated MACD and Metal Loss as functions of Area Ratio. 42

Figure 4.1. A TEM image of grain boundary. 47

Figure 4.2. A defect map of a 4.25-in x 4.25-in commercial mc-Si wafer. Some highly-defected regions can be observed on the sample. 49

Figure 4.3. Photograph showing chemically delineated structure of a defect cluster. 49

Figure 4.4. Measured energy levels introduced by Ni impurities in Si. 55

Figure 4.5. A schematic showing the sample investigated in lifetime and device properties analysis. 60

Figure 4.6. The energy band model used for boundary condition analysis around a type III region. 62

Figure 4.7. Calculated effective lifetime as a function of surface recombination velocity for a single-region sample. 66

Figure 4.8. The normalized carrier density distribution inside single-region samples with different absorption coefficients. 66

Figure 4.9. Calculated (a) N_0 and (b) effective lifetime as functions of SRV and alpha for a single region sample. 68

Figure 4.10. A three region non-uniform samples considered in lifetime analysis. 69

LIST OF FIGURES
(Continued)

Figure **Page**

Figure 4.11. The total carrier number inside the sample as a function of time from very short to long time. 69

Figure 4.12. The calculated effective lifetime as function of $\tau_{central}$ in 3-region sample. 70

Figure 4.13. The time decay curve of normalized carrier amounts in central and side regions of the three-region sample. 71

Figure 4.14. The calculated effective lifetime as a function of $\tau_{central}$ / τ_{side} and the area ratio of central region to the whole sample. 72

Figure 4.15. The carrier flow from side region to central region as functions of time and $\tau_{central}$ / $\tau_{side.}$ 73

Figure 4.16. A ten-grain sample considered in calculation. 75

Figure 4.17. Calculated effective lifetime as a function of coefficient b in Figure 4.16 (solid line). The dashed line is a linear fitting of the calculated results. 75

Figure 4.18. A comparison of the calculate effective lifetime as function of b in a 3-region sample shown in Figure 4.10 and a 10-region sample shown in Figure 4.16. 76

Figure 4.19. A schematic showing the beam-scanning method proposed in the text. 77

Figure 4.20. The calculated (a) effective lifetime and (b) N_0 as a function of beam position when the beam scanning over a 3-region sample. The beam size is 1 unit in the figure. 78

Figure 4.21. The proposed model of different regions in p-n junction built on non-perfect materials. (a) the model of Type I, II, IV region and relation between them inside a device. (b) the junction at the interface of Type I, II, IV region and Type III region. J_1 and J_2 and given by equation (4.8) and (4.11) respectively. The distribution of carriers inside type III region is not considered. 82

Figure 4.22. The I-V characteristics for different lifetime. The sample thickness is 10 μm. 84

LIST OF FIGURES
(Continued)

Figure **Page**

Figure 4.23. The I-V characteristics for different lifetime when the sample thickness is 200 μm. 84

Figure 4.24. The calculated I-V characteristics foe different grain sizes of a 10-μm-thick cell. S=100. The number represents the grain size (in μm) corresponding to the curve at the lower-left side of the number. 86

Figure 4.25. Calculated Jsc, Voc as functions of grain size of the cell considered in Figure 4.24. 86

Figure 4.26. The calculated I-V characteristics for the same cell considered in Figure 4.24. But the interface recombination velocity here is 1000 cm/s. The number represents the grain size (in μm) corresponding to the curve at the lower-left side of the number. 87

Figure 4.27. The calculated I-V charaters for different grain boundaries SRVs. In the figures, S changes from 1000cm/s to 100cm/s in different curves. The grainsize considered is (a) 5 μm, (b) 0.5 μm). 87

Figure 4.28. Comparison of calculated I-V character of two samples. In one sample, the short-lifetime area is concentrated at the center of the sample. In another sample, this area is divided into 5 regions and uniformly distributed in a 10-region sample. 88

Figure 4.29. The calculated I-V characteristics by different generating distribution. In one sample (represented by dashed curve), the generation is uniformly distributed inside the sample. In the other one (solid line), the same amount of generation is concentrated in only central region. 89

Figure 5.1. Operating principle of optical processing furnace. 98

Figure 5.2. A typical temperature profile used in optical processing. 99

Figure 5.3. System configuration of optical processing furnace. 99

Figure 5.4. Schematic of the mask used for TCO layer deposition. The numbered areas are where the TCO was deposited. These numbers are used to identify the devices on the film. 102

Figure 5.5. XRD spectrum of sample HW165-12, before processing, no structure from crystalline Si can be observed. Two visible peaks are from Al 103

LIST OF FIGURES
(Continued)

Figure **Page**

Figure 5.6. XRD spectrum of sample PE1-6, before processing, no structure from crystalline Si can be observed. Two visible peaks are from Al. 103

Figure 5.7. XRD spectrum of sample HW161-22, before processing, two peaks from Si can be observed. 104

Figure 5.8. XRD spectrum of sample HW164-11, before processing, very weak Si (110) peak is visible in this spectrum. 104

Figure 5.9. XRD spectrum of unprocessed sample HW55-22, a strong Si <220> peak can be observed in this spectrum. 105

Figure 5.10. XRD spectrum of unprocessed sample HW54-11. This sample is already strongly crystallized before processing, and strongly textured in Si<111> direction. 105

Figure 5.11. XRD spectrum of sample HW165-21 after a low temperature optical processing, the weak Si <220> peak shows that the crystallization starts during the processing. 106

Figure 5.12. XRD spectrums of sample HW165-11, before (a) and after (b) processing. The apparent change of Si peak can be seen in these figures. 107

Figure 5.13. XRD spectrum of sample HW54-11 after optical processing. There are almost no changes in the peaks from the XRD spectrum of the unprocessed sample (Figure 5.10). 108

Figure 5.14. XRD spectrums of sample 55-12, before (a) and after (b) processing. The apparent change of Si <111> and Si <220> peaks can be seen in these figures. 108

Figure 5.15. XRD spectrum of sample HW61-21, after processing. 109

Figure 5.16. XRD spectrum of sample HW61-11, after processing. 110

Figure 5.17. XRD spectrum of sample HW61-11, after processing. 110

Figure 5.18. XRD spectrum of sample HW61-12, after processing. 111

LIST OF FIGURES
(Continued)

Figure **Page**

Figure 5.19. Summary of Si <111> and Si <220> peaks in the XRD spectrums of processed samples in HW16x-xx groups. The numbers inside the figure indicates the thickness of the sample referred to. 111

Figure 5.20. XRD spectrum of sample HW164-12, after processing. 112

Figure 5.21. XRD spectrum of sample HW164-21, after processing. 112

Figure 5.22. XRD spectrum of sample HW164-21, after processing. 112

Figure 5.23. The sims profile shows the Si and Al distribution inside thin film of sample HW164-12, after processing. 113

Figure 5.24. The SIMS profile shows the Si and Al distribution inside thin film of sample HW164-21, after processing. 113

Figure 5.25. The SIMS profile shows the Si and Al distribution inside thin film of sample HW164-11, after processing. 114

Figure 5.26. XRD spectrum of sample HW165-21, after processing. 114

Figure 5.27. XRD spectrum of sample HW165-11, after processing. 115

Figure 5.28. XRD spectrum of sample HW165-12, after processing. 115

Figure 5.29. The SIMS profile shows the Si and Al distribution inside thin film of sample HW165-21, after processing. 116

Figure 5.30. Measured reflectance spectrum of sample PE1-7, after optical processing. 117

Figure 5.31. Image shows "pinholes" on the surface of PE1-xx group sample. ... 117

Figure 5.32. Measured I-V curve of device 35 on sample HW161-21. 123

CHAPTER 1

INTRODUCTION

Although there are infinite number of stars in our universe burning the energy and dissipating it into the unknown space in a lavish way, energy never seems to be free to human beings. We always need to pay two things for it:- the work involved (which can be symbolized as money according to Karl Marx) and the quality of the environment. Even worse, the energy in the forms that we can use is becoming less and less.

A cheap, clean and renewable energy source is always desirable. Sunlight is the best candidate for this purpose. On an average, the power from the sun reaching a 1mx1m area on the earth's surface is about 900 W[i]. If a circle of about 100 mile diameter in the desert of Nevada could be covered by modern solar arrays, the electric power generated would satisfy the U.S. demand for electricity. However, without being transformed into other forms of energy, sunlight cannot do anything useful except making us feel warmer. Transforming sunlight into electricity is one method (maybe the major method) to utilize it in a more practical way. Solar cell is a device to accomplish this goal. A solar cell can convert the photons in sunlight into electrical power. Although there are various types of solar cells based on different materials, most of the solar cells made today are built on semiconductors. The simplest semiconductor solar cell consists of a single, homojunction device as illustrated in Figure 1.1. The active part of this device uses a p-type semiconductor as the base region with a thin, n-type emitter as the top layer. A gridded metallic contact (or a transparent conducting oxide (TCO) layer) serves as a top electrode for current collection while allowing light to enter the cell, and the entire backside is covered with a metallic layer that serves as both a back contact and an optical reflector.

The photons absorbed in the semiconductor materials generate electron-hole pairs within the device. These so-called photo-generated carriers are separated by the electric field generated by the p/n junction leading to the flow of an electric current into an external load.

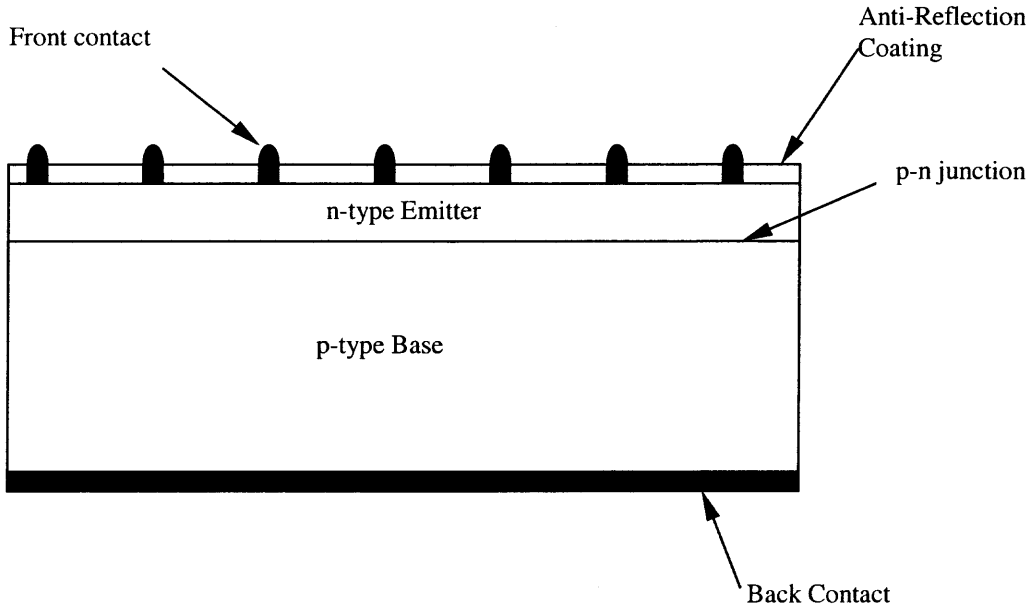

Figure 1.1. Schematic representation of a single p-n junction solar cell.

All solar cells use antireflection coatings and a rough or textured surface to increase photon absorption. For a typical power application, several solar cells are connected in series and parallel arrays to deliver a desired voltage and current. The entire assembly of arrays is encapsulated in a plastic resin using a glass sheet to prevent degradation caused by natural elements. A slightly more complex device structure uses two dissimilar semiconductor materials, one p-type and the other n-type, to form the so-called heterojunction device. Typical examples include CdS(n) / CdTe(p), and CdS(n) /

CuInSe(p) type devices. The use of different semiconductors to form a p-n junction adds constraints in terms of fabrication steps and optimization of the device structure.

Currently semiconductor solar cells are based on a number of semiconductors, including crystalline–Si (c-Si), hydrogenated amorphous-Si (a-Si:H), CdTe, GaAs, and CIS (copper indium diselenide). Of these, c-Si and a-Si:H solar cells and modules are commercially available with c-Si constituting about 85% of the entire commercial market. Recently, CdTe modules have become available commercially. GaAs-based cells and modules are appropriate for concentrator devices. CIS cells appear to offer a promise for low-cost solar cells.

The typical I-V characteristic of a solar cell is shown in Figure 1.2. If there is no external load connected to the cell, the voltage measured at the ends of it is referred to as open-

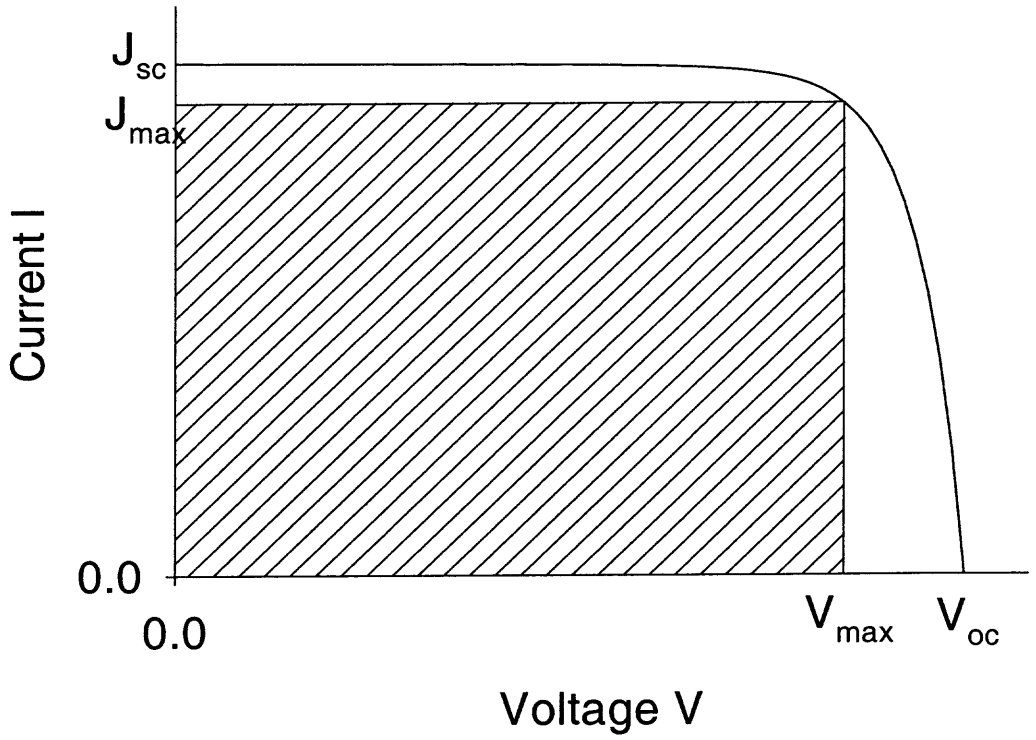

Figure 1.2. A schematic showing the typical I-V character of a solar cell. The area (in I-V space) of the rectangular region is the maximum power the cell can output.

circuit voltage, V_{oc}. Another important parameter in the I-V characteristic of the solar cell is short circuit current density Jsc, which is defined as the current density flowing in the circuit when the external load is zero. When the cell is connected to a non-zero external load, the power delivered to the load depends on the current-voltage characteristics of the device. The power delivered by the cell will be maximized at a voltage lower than V_{oc}. The corresponding voltage and current at this maximum power are referred to as V_{max} and I_{max}, respectively. The ratio (maximum power delivered by the cell / $J_{sc} \times V_{oc}$) is called the fill factor (FF). The intrinsic FF of a solar cell is about 0.8 for Si devices and about 0.85 for direct-bandgap semiconductor devices but the actual FF of the device is often controlled by the cell design.

One of the major problems of the solar cell is its low efficiency. The highest efficiency of Si solar cells available in the commercial market is less than 16%. Another problem with the semiconductor solar cell is that the solar cell can be too expensive in two ways[2]:

1. The cost of materials, fabrication, operation and maintenance of the solar cell can be high with the result that the price of the electricity generated by the solar cells can become a significant issue compared with that of electricity generated from other available sources.
2. The energy cost during cell fabrication can be more than the total electricity that the solar cell can generate in its lifetime. This drawback will make the solar cell a non-viable energy resource.

Getting a high quality device at low cost seems to be a dilemma for every commercial product. Solar cell is not an exception either. Solar cells with efficiency that is close to

theoretical limit have been fabricated in laboratories at very high cost using high quality materials, clean room processing and other expensive techniques in the fabrication process of the solar cells. (Actually, some of the records reported in the literature have exceeded the old theoretical limits. They have changed the theories of the cells[3]). Unfortunately, these high-efficiency solar cells are not practical for commercial purposes because of their high cost. To lower the cost, cheap materials and low-cost processing techniques have to be used. This often yields low-quality devices. However, If the efficiency of the cells is too low, the cost of cell will still be relatively expensive.

To solve this dilemma, PV industry keeps seeking better ways to make low-cost cells with reasonably high efficiencies. This involves the following four objectives:

1. Carefully designed cell structures that will give the best output. For example, in modern cells, AR coating[4] or self-concentrate structure[5] are used to couple as many photons as possible into the cell. Non-planar surfaces/interfaces are utilized to enhance light trapping[6], and buffer layers are adopted to minimize the photon loss at the semiconductor / metal interfaces[7]. The details of all these (and other) configurations are determined by the optical design of the cells. The number of junctions and the positions of them, the doping concentration, the metal contact configurations, the least-acceptable material quality and other properties of the cells are the major features optimized by the electrical design of the cell. Other features such as the thickness of the cell are decided by both the optical and electrical design of the cells. The cell design procedure strongly depends on both optical and electrical modeling of the materials and the device.

2. Low-cost materials with acceptable quality. For example, instead of utilizing high-purity single crystalline silicon ingots, the photovoltaic (PV) industry uses various Si ribbons or poly-Si ingots for device fabrication.
3. Processing techniques that will improve the quality of the starting materials. This includes gettering / passiviation[8] of the materials, recrystallization / grain enhancement[9] of thin films and other techniques.
4. Other low-cost device processing techniques, including junction formation, metallization, AR coating, texturing and wafer handling, etc.

It should be pointed out that these objectives are not independent of each other. For example, the design of the cells will always be limited by the quality of the materials and processing techniques available.

The need for developing better and inexpensive solar cells has led to the development of thin-film solar cells. Normally, thin-film solar cells use substrates/superstrate as the mechanical support for the device and a thin layer of semiconductor as the active layer to generate electricity. In most cases, the substrate does not take part in the generation of electricity.

Thin film solar cells possess the potential to lower the device cost significantly because the material cost of thin film cells can be much lower than that of thick cells. The consumption of the expensive semiconductor material in thin-film devices can be much less compared with that in thick cells and the substrate materials can be very cheap. Especially for large-area usage, the formation of large-area thin-film can be made to cost much less than large cross section ingots or large area ribbons. As to the processing, the

steps required could be fewer in thin-film cell fabrication and the requirements on process environment can be relaxed.

Thin-film structure is preferred because of its inherent electrical benefits. Although thicker cells can absorb more photons, the minority carriers generated by these photons are more likely to be recombined in a thicker cell before they are collected by the external circuit. In addition, the minority carriers are generated mainly by the photons having energy larger than the bandgap of the semiconductor. Because of the high absorption coefficients of the semiconductor, the total amount of photon-generated carriers will not change significantly when the cell thickness exceeds some value. Furthermore, the loss of photon absorption caused by the thin structure can be compensated by proper optical design, as will be shown in the following chapters. It is expected that the efficiency of thin film solar cells will be at least the same as that of thick cells.

However, to develop a thin film solar cell, several critical problems need to be solved, as described here:

1. How to design the structure of the cell so that its' overall performance can be optimized? Optically, the structure of the cell should permit as many as photons as possible in order to generate more minority carriers. Electrically, the structure of the cell should be able to maximize the amount of the minority carriers collected by the external circuit.
2. What materials to be used in the cell? These materials include semiconductors, substrate materials, contact materials and so on. The quantity and the quality of materials should be subject to three categories of constraints – a) the allowance of the

processing techniques, b) the design specifications of the cells, c) the cost of the materials.

3. What processing techniques should be used? The processing techniques should be cost efficient and compatible with the low quality materials. For example, low temperature processing is needed for low-softening-point glass substrates.
4. When the cell structure becomes thin, the effect of surface recombination becomes stronger, how to develop more effective surface passiviation techniques? The defects inside the materials will also play an important role in degrading the performance of the cells. How to lessen the influence of these bulk defects?

The objective of the project described in this thesis is to develop a new thin-film silicon single-junction solar cell. The illustration of this cell is shown in Figure 1.3. The details

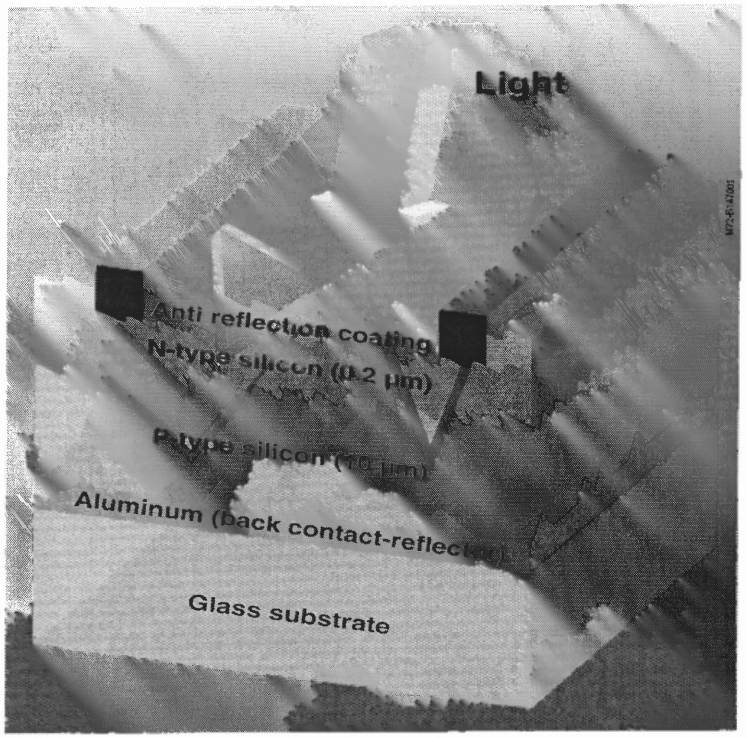

Figure 1.3. The schematic of NREL thin film μc-Si solar cell.

of this cell will be described in the next chapter.

The tasks involved in developing this cell include:

1. Development of a novel, simple design of the cells that is really compatible with the low cost materials and low cost processing procedures.
2. Development of new modeling tools that will help to analyze materials and devices.
3. Development of new processing techniques that are low-cost and low-temperature compatible.

The major work conducted by the author in this project are:

1. Participatition in the design of the solar cell.
2. Development of a new modeling tool for lifetime analysis of non-perfect materials and device properties of the cell fabricated on non-perfect Si thin films.
3. Detailed study of optical processing techniques and its applications to the back contact formation and crystallization of films.

The details of this work will be described in other chapters.

The thesis will be organized as follows: In the second chapter, the details of some thin-film Si solar cells developed by other groups will be reviewed. The third chapter will concentrate on the optical features of the cell that we developed – the thickness, the interface/surface shape, and so on. The electrical properties of the materials and the devices will be considered in Chapter 4. The software developed in the analysis will also be introduced in this chapter. In the fifth chapter, the major processing techniques used in the cell fabrication will be investigated. The sixth and final chapter will be the conclusions and future work based on the research work performed in this thesis.

CHAPTER 2

SILICON THIN-FILM SOLAR CELLS: AN OVERVIEW

2.1 Introduction

Among all kinds of semiconductor devices, solar cells may have the most diversity. Various types of thin film silicon solar cells have been developed in these years. Their structure and fabrication steps can be very different from the each other. The diversity of the solar cells comes from the flexibility and simplicity (compared with other semiconductor devices) of the device. Table 2.1 summarizes most of the thin-film Si solar cells on various substrates made by different groups in recent years.

The merits of using the thin film structure have been discussed in the first chapter. In this chapter, some general issues concerning the design and fabrication of the thin-film solar cells will be reviewed. Cells developed by various groups will be investigated in detail.

Table 2.1. Summary of thin silicon solar cell fabrication methods and performance

Foreign Substrate

Technique	Temperature	Substrate	Processing	Efficiency	rRmarks
Zone Melt Recrystallisation (ZMR) Mitsubishi Blectric Co.	>1300°C	SiO_2 on MG-Si	LPCVD 50-60 micron active layer, alkaline wet etching, P indiffusion, H passivation by ion implantation, DARC, backside etching for rear electrode	14.2% 100 cm^2 (JQA 1993) 16.4 % 4 cm^2	recystallisation speed = 1 mm/s
FhG-ISE	>1300 °C	Perforated SiO_2 on Si	no seeding, no texture, no defect passivation, interdigitated grid, 30 micron by thermal CVD	6.1% 4 cm^2 (1996)	9.3% by Large Area Recrystallisation (LAR)
	>1300 °C	Graphite	interdigitated grid, reactive ion etching	11.0% 4 cm^2 (1997)	9.3% on ceramic, >17% expected for screenprinting
Solid Phase Crystallisation (SPC) Sanyo Electric Co.	=600 °C	Metal	PECVD p-type a-Si:H (SiH_4), ITO sputtering, evaporation of Ag finger contacts	9.2% 1 cm^2 (1994)	=10um a-Si, 10-600 min. annealing

Table 2.1 (continued). Summary of thin silicon solar cell methods and performance

Technique	temperature	Substrate	Processing	Efficiency	remarks
Liquid Phase Epitaxy (LPE) Astropower inc.	~1000 °C	Graphite cloth	gas phase P indiffusion, PECVD H passivation, photolithographic contacts, DARC	13.4% 1 cm^2 (NREL 1994)	Si directly deposited on substrate, active layer =80 um
		Unknown	$POCl_3$, Al gettering, H passivation, PECVD SiO_2 as ARC	14.6% 1 cm^2 (NREL 1996)	film thickness unknown
		Unknown	unknown	16.6% 1 cm^2 (NREL 1997)	record thin film Si on foreign substrate, no vacuum process
Chemical Vapour Deposition (CVD) Univ. de Neuchatel	=200 °C	textured TCO/glass	3.6 micron uc-Si by PECVD at 100 Mhz (SiH_4), doping by PH_3 and B_2H_6, ZnO/Ag backcontact	8.5% 1 cm^2 (1999) 13.1% a-Si:H/uc-Si 10.7% (1999)	deposition rate < 2 A/s, unstabilized, Stabilized (other substrates possible)
IMEC	>1000 °C	p+ SILSO	20 micron film by thermal CVD, DARC, no texture, SiN passivation, evaporated contacts	13.7% 4 cm^2 (1997)	no H passivation 11.6%, 7.6% on SSP, 10.3% on RGS, 13.2% on EFG
FhG-ISE	>1000°C	Silicon Sheets from Powder (SSP)	First deposition BSF, 30 micron by thermal CVD, no texture, no H passivation, SiN coating	8.00% 4cm^2 (1997)	dep. Rate > 10 um/min., 11.1%on SiLSO, 17.4% on FZ (invested pyramids, local emitter, thermal oxide)
Ecole Polytechnique	=150 °C	Textured TCO/glass	polymorphous standard pin, 0.4-0.8 micron i-layer	9.30%, 0. 1 cm^2	mixed a-Si:H/uc-Si matrix
Canon Co.	200-400 °C	Unknown	Standard nip structures, Ag/ZnO backcontact, > 1 micron thick i-layer, VHF used	7.4% 0.25 cm^2 (1999) 11.5% a-Si:H/uc-Si	Stabilized results
Excimer laser crystallisation Kaneka Co.	=600 °C	Glass	laser crystallisation of 100 nm a-Si by PECVD (B_2H_6/SiH_4), followed by n- and p-type uc-Si and 6 micron intrinsic poly-Si (all PECVD), ITO front contact and Ag fingers	10.1% 0.25 cm^2 (JQA 1997) 12.8% a-Si:H/uc-Si (1997)	>14% expected

2.2 General issues

Although thin-film cells can be made in various configurations and their fabrication procedure can be greatly diversified, there are some common technical issues that need to be considered in the design and fabrication of the cells. In this section, some of these issues will be discussed.

Design / Modeling

Design / modeling of the cell is the most important phase in the development of an acceptable thin-film solar cell. Here, some general concerns of the thin-film cell design and modeling will be presented. Details of the design and modeling developed at NREL will be investigated in the next two chapters.

When the cells become thinner, the absorption of incident light becomes weaker if the surfaces of the cells are kept planar[10]. Light trapping is necessary to enhance the absorption of light in the cell. The most effective way to do trap the light is by using non-planar surfaces in the cell structure. The design of light trapping enhancement structure is a major goal of the optical design of the cell.

Low-cost materials are often used in thin-film Si cells. Unfortunately, low cost thin-film materials usually mean low quality. To get the best electrical output from low-quality materials, the electrical structure of the thin-film device needs to be carefully designed. The minimum requirements on the materials can also be found by electrical designs.

The design of the device strongly depends on the modeling tools that can predict the properties of the device in various configurations with sufficient precision. The implementation of the complicated surface / interface structure makes the optical modeling of such a device difficult using simple optics[11]. Modeling of large-area devices fabricated on materials containing large amount of grain boundaries, impurities and other defects / defect clusters is also a big challenge.

Meanwhile, the structure of the cells is also limited by the materials and processing techniques available to the designer. For example, the thickness of the cell may be limited by the film growth methods. If there is high temperature processing involved in the

fabrication, materials that cannot withstand high temperature processing cannot be used in the cell structure.

Substrate/superstrate materials

The mechanical weakness of thin-film semiconductor requires a substrate / superstrate to support and protect the device. The cost of the substrate/superstrate materials could be a major component of the total cost of the device. The substrate/superstrate's tolerance to process conditions is also a major limitation on the processing techniques that can be used in the fabrication of the cells.

The utilization of cheap materials as the substrate/superstrate of the cell can lower the cost of the final devices greatly. A number of materials, including single-crystalline Si[12], glass[13 14], metallurgical-grade silicon[15], stainless steel[16], graphite[17] and specially prepared ceramics[18], have been used for cell fabrication. However, low-cost substrates often cause problems such as: the tolerance to high process temperatures; impurity diffusion from the substrate to the thin-film; thermal expansion mismatch between the film and the substrate; chemical and mechanical instability of the substrate and so on. To choose appropriate substrate materials is an important issue in the fabrication of low-cost thin polycrystalline Si solar cells.

Film deposition:

Various methods have been deployed to grow thin-film silicon on substrates/superstrates. These methods include CVD, LPE[19], sputtering[20], spray[21], peel[22], and even etching or polishing from the bulk materials. By properly controlling growth conditions, which

usually mean high cost and long growth time, high quality thin-films can be obtained. However, to lower the cost, the depositions must be performed at fairly high speeds and under relaxed conditions. Low cost post-deposition processing is necessary to improve the material quality. In Table 2.2, a summary of the film growth techniques often used for Si films is presented.

Table 2.2. Summary of multi-crystalline (mc) -Si growth techniques

Method	cost	Max. Grow speed	Typical maximum thickness	Crystallized grain size	Film quality
CVD	medium	>10μm/hr	<100 μm	<0.1 μm	depends
LPE	medium	< 5 μm/hr	>100 μm	Could be sc-Si[23]	good
Sputtering	low	~10A/sec	< 1μm	<100A	bad
Spray	low	Very high	<1000 μm	None	bad
Peel	High	N/A	No limit	Could be sc-Si	Good
Etching	High	N/A	No limit	sc_Si	Good

The active layer: amorphous or multi-crystalline Si?

Depending on the growth and post-processing techniques used, the film can have different crystallography — it can be single-crystal[23], multi-crystal or amorphous. Although amorphous Si (a-Si) has many advantages as the thin-film photovoltaic material, a major drawback of a-Si is its instability under optical illumination, which causes degrading of device performance. Instead of classical p-n diode, a p-i-n structure is used in a-Si thin film cells because of the low minority carrier diffusion length in a-Si materials. Multi-crystalline Si thin-film does not have degrading problems. With fairly large grain size, mc-Si thin-film cells can have better performance than a-Si thin-film cells. Since grain boundaries are one of the major defects in polycrystalline materials, enlarging the grain size (hence decreasing the relative amount of grain boundaries) is an effective way to improve the quality of the thin-film. Diminishing the recombination at

the grain boundaries is also an effective way to improve the quality of the micro-crystalline Si (μc-Si) films. However, to grow large grain-size thin-films or to enlarge the grain size of the as-grown film can be very costly. Finding a balance between cost and material quality is a critical issue. Various solar cell structures that combine the merits of both thin-film a-Si solar cell and "classical" thick cell are also being developed.

Material qualities of multi-crystalline active layer

A major issue that relates to the development of μc-Si thin film is the quality of the Si film, especially the grain size of the film. Calculations have shown that efficiencies exceeding 18% can be obtained only if the grain size can be >20 μm. This is about two orders of magnitude larger than that of the typical μc-Si film. Thus, it is necessary to either deposit Si film of considerably large grain size (which is very costly) or enhance the grain size after deposition. Difficulties in achieving a large-grained film are related to the use of low-cost substrates, which normally are not able to tolerate the harsh processing condition required for grain enhancement. One of the approaches to overcoming this problem is to develop high-temperature glass(es) or ceramics that can be thermally matched to Si, and can withstand Si processing temperatures. Several groups are exploring the possibility of developing such glasses.

Post-deposition processing:

To improve the quality of the films deposited, extra process steps need to be performed on the thin film before the fabrication of the device. These steps include recrystallization, grain enhancement, gettering/passivition etc. Recrystallization is the process during

which the a-Si is transformed into crystalline Si. Grain enhancement is the process of the tiny grains in μc-Si growing larger. In many papers, these two processes are not distinguished, and in some practical situations, they are very difficult to be separated. We believe that the mechanisms involved in these procedures could be different in some cases. Gettering is used to remove the impurity atoms from the active layer in the cell and passivation is used to lower the recombination velocity at the device surface/interface (grain boundaries). Since the starting materials of most low-cost solar cells may have very small grains and high density of defects and impurities, these steps are critical to improve the quality of the device. They are also the challenges in the development of thin-film cells.

Other processing steps:

These processing steps include the formation of junctions, metallization, anti-reflection (AR) coating and texturing etc. In thin film solar cells, most p-n junctions are "grown". An n-type layer is deposited on p-type material or vice versa instead of forming the junctions by diffusion or ion-implantation. The most popular AR coating materials used in mc-Si thin film solar cells include ZnO, MgF_2 and Ta_2O_5. All of them have refractive indices close to $\sqrt{n_{Si} n_{air}}$. Normally, in thin-film solar cells, Al or Ag is used for back contact. To minimize the metal loss at the semiconductor/metal interface, a buffer layer (such as ZnO) is present between the semiconductor and back contact. For the front contact, because of the relatively shorter minority carriers diffusion length in thin-film mc-Si materials, the metal grid, which is often used in thick cells, is not used in thin-film

cells. Instead, a TCO layer covering the entire front surface of the cell is used for front contact in most thin-films cells.

2.3 Examples of thin film solar cells

In this section, some thin film solar cells will be reviewed. These cells are selected as representatives of current thin-film technology because they have very unique designs/structures and/or outstanding performance.

ZMR cells

To improve the quality of thin-film materials, recrystallization and grain enhancement process is necessary. The cell shown here is a typical example of how this process will help to improve the cell performance.

Ishihara[24] et. al. have reported impressive results of solar cells fabricated on poly-Si thin-films obtained by Zone Melting Recrystallization (ZMR) technology. The structure of

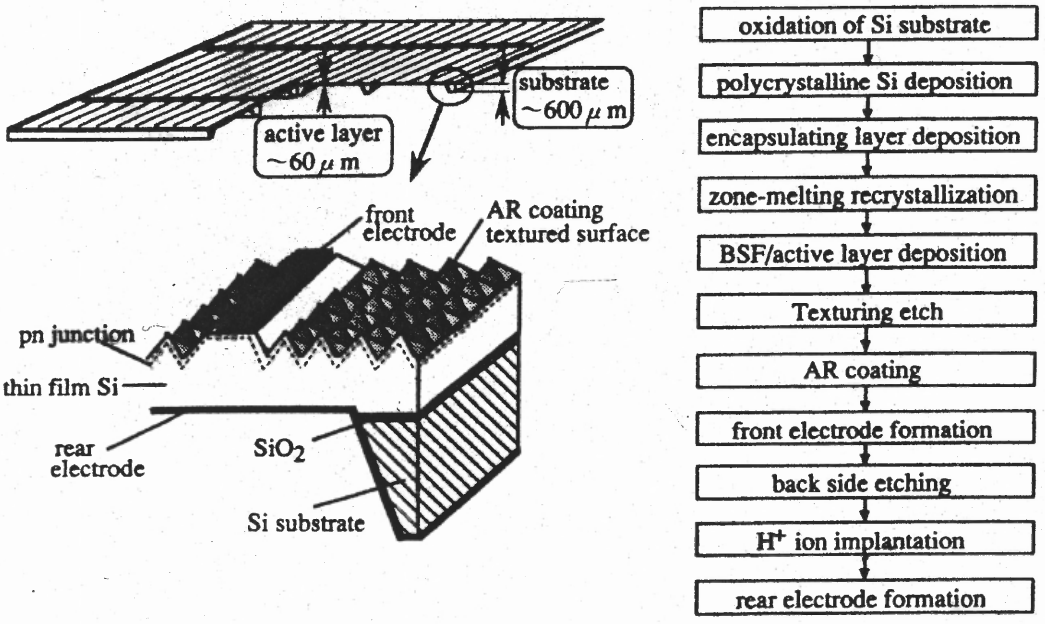

Figure 2.1 A schematic showing the structure and fabrication procedures of ZMR solar cell.

their cells and processing procedure is shown in Figure 2.1. They use a thin layer of SiO_2 on the Si substrate as a stopping layer for impurity diffusion. Over the SiO_2 layer, an a-Si film was grown by LPCVD. Then, a narrow zone on the sample was heated up to about 1200 °C by a line-shaped heat source of carbon strip just above the sample in vacuum. The film inside this zone is melted by heating and then recrystallized after the carbon strip is moved away. By moving the heating source all over the sample, the entire film can be recrystallized. In this study, a (100)-dominated surface was obtained with a scanning speed at $0.2mm \cdot s^{-1}$. A grain size of millimeter to centimeter order was reached. They achieved a high conversion efficiency of more than 14% for a 10×10 cm^2 cell and 16% for 2×2 cm^2 cell.

Martin Green's multi-junction solar cells

By choosing very complicated design and high-cost processing, thin-film solar cells can reach high efficiency. The example here shows the "high-end design" of thin-film cells. Matin Green at the University of New South Wales has developed a multi-junction cell approach to enhance the separation and collection of minority carriers generated. In a multi-junction approach, typically reminiscent of a-Si cell designs, one can take advantage of low material quality of short minority-carrier diffusion length. The structure proposed by Green is illustrated in Figure 2.2. Although the details of the cell material are not known, it is expected that the semiconductor film will consist of hydrogenated micro-crystalline silicon. Such a film consists of polycrystalline-Si with grain size typically <1 μm, hydrogenated grain boundaries, and material that contains a significant amount of amorphous tissue in the film.

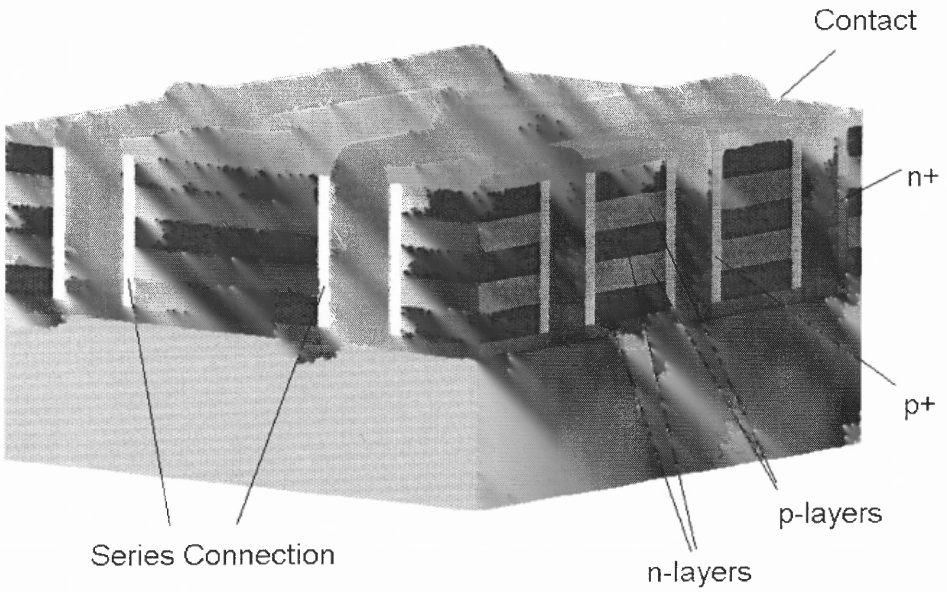

Figure 2.2. A schematic showing Martin Green's multi-junction solar cell

An as-grown cell

With high temperature tolerating substrates (such as c-Si, graphite and quartz), Si thin-films can be grown at high temperatures. These films can form with fairly large grain sizes so that the grain enhancement step may not be necessary in this case.

Zhao[12] et al. reported a thin-film mc-Si solar cell grown on c-Si substrate. A 16-μm-thick n-type active layer was grown by RTCVD at 1130°C. The efficiency of this cell is close to 10% (9.88%).

STAR structure and p-i-n structure mc-Si cells

The structures of most μc-Si thin film solar cells follow that of the "classical" thick cells — using a p-n junction diode as the active device. Several groups[25 26 27] have also developed thin-film μc-Si structure in p-i-n structures.

The Kaneka group has developed a cell configuration called **S**urface **T**exture and enhanced **A**bsorption with a back **R**eflector (STAR)[28]. Figure 2.3 shows a sketch of the STAR cell. It consists of a glass substrate with a back reflector on which an n-type μc-Si film is deposited by plasma CVD process. Next, an i-type poly-Si film is deposited at substrate temperature <550 °C. This layer has no intentional doping but is p-type and has a carrier concentration of approximately $1x10^{15\text{-}16}$ cm^{-3}. This is followed by depositions of a p-type Si film, a layer of ITO, and an Ag-grid electrode. The total thickness of the active layer in STAR structure is less than 5 μm. The thin film is (110) textured and 90% crystallized[28]. The diffusion length of the minority carriers in the film is less than 20 μm. Some of the results obtained on the STAR devices are given in Table 2.3[28].

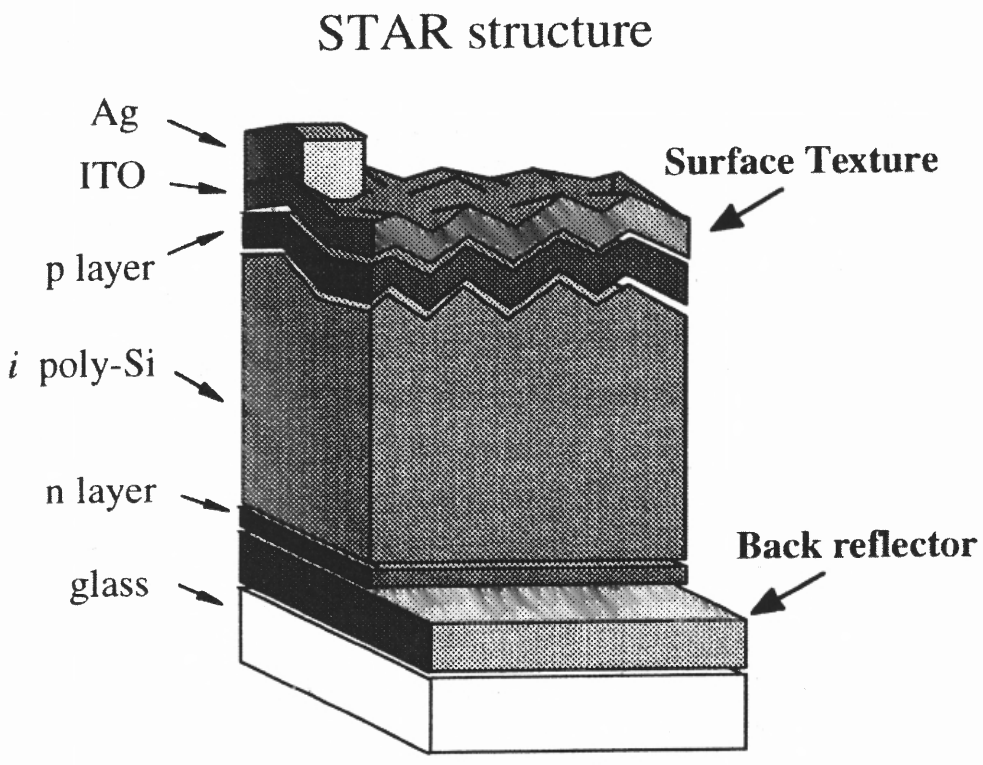

Figure 2.3. A schematic showing "STAR" structure cell

Table 2.3. Some parameters of "STAR" structure thin film solar cell

Thickness (μm)	1.5	2.5	3.5
Jsc (mA/cm^2)	22.9	24.39	26.12
Voc (V)	0.526	0.510	0.480
F.F. (%)	77.2	75.5	74.8
Efficiency (%)	9.3	9.8	9.8

The STAR structure illustrates the feasibility of using the natural roughness of the as-grown μc-Si film for light trapping purposes. Since as grown rough surface is common in thin-films, this is a very encouraging result. It also shows the potential of using very thin-film structures on not so high quality materials.

Shar et al. developed another p-i-n structure cell. In their approach, a p-i-n structure based on hydrogenated microcrystalline silicon (μc-Si:H) and microcrystalline silicon (μc-Si) were grown on SnO_2-coated glass substrates using PECVD method. They reported an efficiency of 7.7 % on a single junction cell. This group also developed a tandem cell structure (so-called "micromorph" structure) with an a-Si top cell on their p-i-n structure with an efficiency >12%.

Some common features can be observed from these cells, such as:

1. Textured surfaces and AR coating are used in most of the designs to enhance photon absorption.

2. <50 μm thick multi-crystalline active layer is sufficient to accommodate low-quality materials

3. Metal back reflectors. A disadvantage of the reflecting metallic back electrode is that it can lead to significant losses due to optical absorption[29]. However, this loss decreases with increase in film thickness.

2.4 NREL design of thin-film μc-Si solar cell

Recently, a new structure has been proposed at NREL that integrates several process advantages in cell design and overcomes many of the substrate related problems. Figure 1.3 is a sketch of the cell. It consists of a p-type Si film, about 10 μm thick, deposited on a metal-coated glass substrate. An n-type junction can be made by any conventional method, followed by an AR coating and front metallization. As illustrated in this figure, the major features of this cell are:

1. 10-μm-thick micro-crystalline thin-film as the active layer; This thin layer can be formed using low cost techniques such as spray technique. The crystallization and grain enhancement steps will be performed to improve the quality of the thin-film. The grain size of the film is about several microns.
2. Al back contact. This Al layer has multiple functions in the cell structure. Optically, it acts as the back reflector of the device. It also helps to release the stress accumulated in the thin-film during the initial deposition. During processing, the Al will induce the crystallization, grain enhancement and formation of the backside texture. It can also do gettering.
3. Glass substrate. Regular glass can be used because all the procedure involved are low-temperature process.
4. Non-planar / Textured interface is used to enhance light trapping.

In the next two chapters, both the optical properties and electrical properties of this design will be studied in detail. In the chapter following them, study on the fabrication procedure of this cell will be presented.

CHAPTER 3

OPTICAL DESIGN OF NREL THIN-FILM SILICON SOLAR CELLS

3.1 Introduction

Like the design of other semiconductor devices, the purpose of solar cell design is to solve two problems: First, what components are needed to fulfill the requirements on device performance? Second, once the first problem is solved, how can the device structure be optimized so that the device can give the best performance?

The optical design of the cell is aimed at solving the second problem for solar cell. As a device that transforms light to electricity, solar cells should trap as many photons as possible to generate more electrical power. The goal of optical design of the solar cell is to optimize the structure of the cells so that the amount of photons collected by the cell can be maximized.

To increase the number of photons collected by the cell, two methods can be considered: The first method has to do with increasing the number of photons input to the cell. This can be done by reducing the light reflected back to the air from the front side of the cell. Anti-reflection (AR) coatings and front side texturing can be utilized to fulfill this goal. To choose appropriate materials for AR coatings and design configuration of the front side texture are among the tasks of optical design for solar cells. Concentrators[5] can also be considered as a way to increase the sunlight input to the cell. The design of the concentrator and the corresponding cells are beyond the scope of this thesis.

The second method involves improving the structure of the device so that the light can travel as long as possible inside the semiconductor layer before it is absorbed by metal or

escapes the device. For thick cells (>100 microns), keeping the light inside the semiconductor layer, until it is absorbed by the semiconductor, is not difficult since the light can be almost totally absorbed in this layer even in just one trip. Figure 3.1 shows the AM1.5 spectrum[2] before and after absorption by a 500-μm-thick double side polished silicon wafer. It can be seen that this wafer absorbs the major part of the AM1.5 spectrum. But for thinner cells, the situation is different. Figure 3.1 also shows the calculated spectrum after AM1.5 radiation passes through a 10-μm-thick Si double-side-planar Si film. It can be seen that the absorption in this thin film is much weaker than that in a thick wafer. In order to keep the light inside the thin film, one must force the light to bounce back and forth inside the semiconductor layer, in other words, "trap" the light in the semiconductor layers where the electricity is generated.

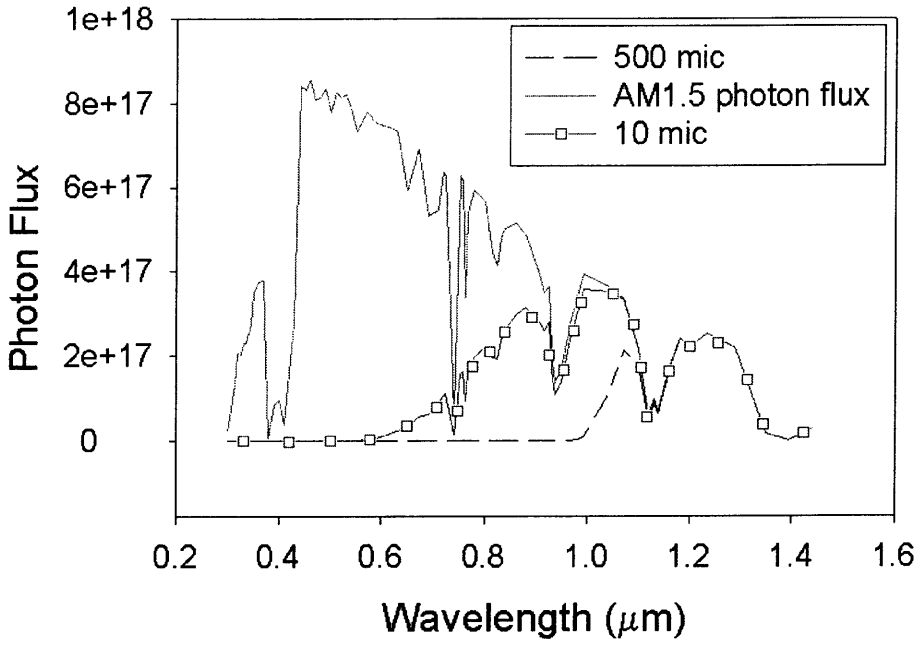

Figure 3.1 Comparison of the transmitted AM1.5 photon flux through a 500-μm-thick Si wafer and a 10-μm-thick wafer. Also shown in the figure is the photon flux of AM1.5 spectrum.

Although multiple reflection of light does happen in double side polished wafers, there is still too much light leaking from this structure. The only way to enhance light trapping is to use rough surfaces/interface instead of planar structures. The shape of the surface / interface of the device will play a critical role in the light trapping process. Finding the most appropriate surface configuration that can maximize light trapping is one of the major goals of optical design of the solar cell. Depending on its morphology, a rough surface can be either Lambertian reflective[30] or geometric reflective (textured). Only the surface/interface structure that is geometric reflective will be investigated in this chapter. Meanwhile, since the metal surface is not totally reflective (especially at the semiconductor / metal interface), part of the light incident on the metal will be absorbed instead of being reflected back to the semiconductor. The photon loss due to metal will become a severe problem when the thickness of the cell decreases[7]. Minimization of the metal loss is also an important task in the design of the solar cell.

In this chapter, optical modeling software, PV optics[11], developed by Sopori at NREL, is used to achieve the best configuration of a single-junction thin film solar cell. A series of calculations have been performed using this software. The results will yield information on the influence of changes in the cell configuration on the optical property of the device and the best configuration for single-junction Si thin film solar cells.

It should be emphasized again that the optical design of the cells is only an optimization process of the cell structure determined by other design procedures. Depending on the structure of the cell, the results of the optical design can be very different in different situations. Here, most of the design work is performed only on the cell structure introduced in Chapter 1.

This chapter will be organized in the following way: A brief introduction to the principle of the software *PVoptics* and a review of Si optical properties will follow this section. Then the results on the thickness and configuration of interface/surface of the cell will be discussed. The final section of this chapter will be conclusions from calculations.

3.2 Methodology

3.2.1 Description of PV optics

PV optics is optical modeling software developed by Sopori et al. at NREL. This software can calculate a variety of optical parameters for multi-layer devices. These parameters include reflectance, transmittance, and distribution of absorbed photons in each layer.

Figure 3.2 is a schematic illustrating the methodology of performing these calculations. A beam of light is incident on the sample that has an arbitrary surface morphology. This beam is split into a large number of beamlets that impinge on a small region of the surface. Each beamlet is permitted to propagate within the sample and we keep track of its entire path while it undergoes reflection, transmission, and absorption.

The following formulae are applied to calculate optical parameters in the bulk and to determine the effects of multilayer coatings. In the semiconductor, the beam propagates as:

$$I_{final} = I_{initial} \cdot e^{-\alpha z} \qquad (3.1)$$

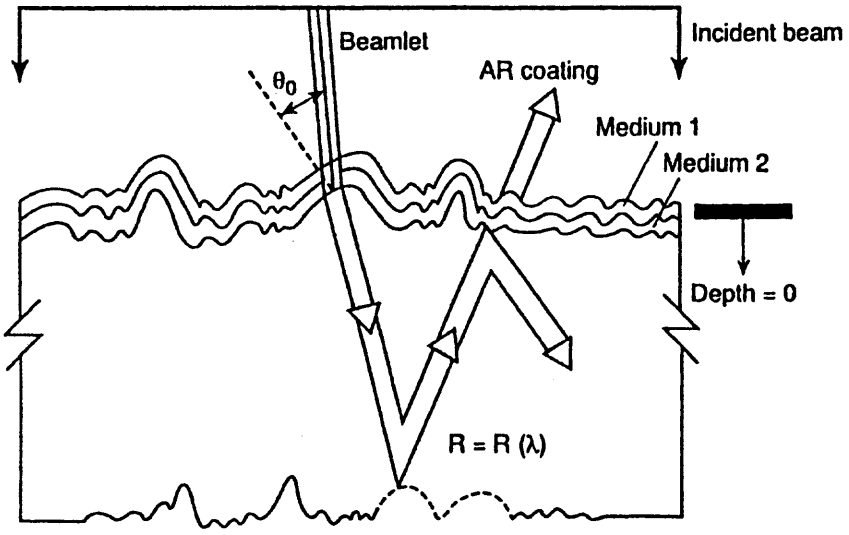

Figure 3.2. A schematic shows the algorithm PVoptics calculates the optical properties of multi-layer structures.

Where

$$\alpha = \frac{4\pi k}{\lambda} \tag{3.2}$$

and extinction coefficient k is the imaginary part of the complex refractive index:

$$n(\lambda) = n - i \cdot k \tag{3.3}$$

At each interface, we use the following equations to determine the propagation path:

$$\cos(\theta_0) = \hat{r}_i \cdot \hat{n} \tag{3.4}$$

$$\cos(\theta_j) = \sqrt{1 - (\frac{n_{j-1}}{n_j})^2 \cdot (1 - \cos(\theta_{j-1})^2)} \tag{3.5}$$

Where θ_0 is the incident angle of the light, $\hat{r}_i$ the direction vector of the incident light, $\hat{n}$ the unit vector perpendicular to the local surface on which the light incident, θ_j the output angle at different layer j (j=1,2,3...), and n_j the refractive index of different layers.

The reflection coefficients for parallel and perpendicular polarization are:

$$r_{\perp} = \frac{r_{1\perp} + A_{\perp} \cdot e^{-i\frac{4\pi}{\lambda} n_1 t_1 \cos(\theta_1)}}{1 + r_{1\perp} \cdot A_{\perp} \cdot e^{-i\frac{4\pi}{\lambda} n_1 t_1 \cos(\theta_1)}} \tag{3.6}$$

$$r_{\parallel} = \frac{r_{1\parallel} + A_{\parallel} \cdot e^{-i\frac{4\pi}{\lambda} n_1 t_1 \cos(\theta_1)}}{1 + r_{1\parallel} \cdot A_{\parallel} \cdot e^{-i\frac{4\pi}{\lambda} n_1 t_1 \cos(\theta_1)}} \tag{3.7}$$

$$r_{j\perp} = \frac{n_{j-1} \cdot \cos(\theta_{j-1}) - n_j \cdot \cos(\theta\ )}{n_{j-1} \cdot \cos(\theta_{j-1}) + n_j \cdot \cos(\theta_j)} \tag{3.8}$$

$$r_{j\parallel} = \frac{n_{j-1} \cdot \cos(\theta_j) - n_j \cdot \cos(\theta_{j-1})}{n_{j-1} \cdot \cos(\theta_j) + n_j \cdot \cos(\theta_{j-1})} \tag{3.9}$$

Where,

$$A_{\perp} = \frac{r_{2\perp} + r_{3\perp} \cdot e^{-i\frac{4\pi}{\lambda} n_2 t_2 \cos(\theta_2)}}{1 + r_{2\perp} \cdot r_{3\perp} \cdot e^{-i\frac{4\pi}{\lambda} n_2 t_2 \cos(\theta_2)}} \tag{3.10}$$

$$A_{\parallel} = \frac{r_{2\parallel} + r_{3\parallel} \cdot e^{-i\frac{4\pi}{\lambda} n_2 t_2 \cos(\theta_2)}}{1 + r_{2\parallel} \cdot r_{3\parallel} \cdot e^{-i\frac{4\pi}{\lambda} n_2 t_2 \cos(\theta_2)}} \tag{3.11}$$

In this manner, each beamlet bounces back and forth within the sample. The net energy absorbed at each plane within the sample is determined. This procedure is continued for each beamlet till the energy in the beam is reduced nearly to zero. This process yields the net reflection, transmission, and absorption in the wafer.

In our calculations, Maximum Achievable Current Density (MACD) is used to evaluate the ability of the device to absorb photons in the semiconductor layers. It is defined as the current density that could be generated if every photon (in AM1.5 spectrum) entering the semiconductor layer would generate a electron-hole pair and this pair contributes to current that is collected by the external circuit. Another parameter, Metal Loss is used to

estimate the amount of photons lost at the semiconductor/metal interface. Metal Loss is defined as the current density that could be generated if every photon (in AM1.5 spectrum) lost at the semiconductor/metal interface would generate a electron-hole pair and this pair results in a current that is collected by the external circuit. Apparently, better devices have higher MACD and lower Metal Loss.

3.2.2 Optical properties of Si

From the last subsection, it can be seen that all the calculations are based on two fundamental optical parameters of materials used in device fabrication: refractive index *n* and extinction coefficient *k*. Among all the materials used in the cell, the semiconductor has the most diverse n and k — these values can change significantly at different doping concentrations and temperatures. A comprehensive model describing the n and k of semiconductors at the desired temperature and doping concentration is essential to the development of optical modeling software of semiconductor devices.

As part of a joint project between NREL and NJIT, the author has successfully developed such an *n-k* model for silicon. This model combines experimental empirical results and theoretical calculations from different sources. Some parameters in these results have been fine-tuned to match the experimental data. This model can give n and k at different doping concentrations and different temperatures over a wide wavelength range with fairly high precision. The details of this model will be described in this sub-section.

a) the refractive index of lightly to medially doped Si:

When Si is not heavily doped (doping concentration<$10^{18}cm^{-3}$), the refractive index of lightly doped Si as a function of temperature and wavelength can be written as[31]:

$$n(\lambda,T)=\sqrt{e_r(T)+b(\lambda,T)} \qquad (3.12)$$

Where,

$$e_r(T) = 11.4445 + 2.7739\times10^{-4}T + 1.7050\times10^{-6}T^2 - 8.1347\times10^{-10}T^3 \quad (3.13)$$

$$b(\lambda,T) = \frac{L(T)}{\lambda^2}(A_0 + A_1T + A_2T^2) \quad (3.14)$$

Where,

$$L(T) = \exp(-3\Delta L(T)/L_{293}) \quad (3.15)$$

and A_0=0.8948, A_1=4.3977×10^{-4}, A_2=7.3835×10^{-8}, $\Delta L(T)/L_{293}$ is given by:

$$\frac{\Delta L(T)}{L_{293}} = -7.1\times10^{-2} + 1.887\times10^{-6}T + 1.934\times10^{-9}T^2 - 4.544\times10^{-13}T^3 \quad (3.16)$$

The extinction coefficient of Si

Depending on the wavelength of light, the dominant light absorption mechanism inside the Si changes. So the expression for the extinction coefficient will have different formalism for different wavelength ranges, as presented below:

λ: 0.4μm--0.6μm

The absorption of photons in this wavelength range is mainly from direct band transition of electronic absorption. The extinction coefficient from this mechanism can be written as[32] :

$$k(h\nu,T) = k_0(h\nu)\exp(T/T_0(h\nu)) \quad (3.17)$$

Where, $k_0(h\nu)$ and $T0(h\nu)$ are given by:

$$k_0(h\nu) = -0.0805 + \exp(-3.1893 + 7.946/(Eg^2 - (h\nu)^2)) \quad (3.18)$$

and

$$T_0(h\nu)=369.9 - exp(-12.92+5.509h\nu) \quad (3.19)$$

Eg is the band gap of Si.

λ: 0.6--1.5μm

The absorption in this range is mainly from phonon-assisted indirect electronic transitions. It can be written as[33]:

$$\alpha_{BG}(h\nu,T)=\sum_{i=1}^{2}[\alpha_{ia}(h\nu,T)+\alpha_{ie}(h\nu,T)]+\sum_{i=3}^{4}\alpha_{ia}(h\nu,T) \quad (3.20)$$

Where, E is the photon energy, T is the absolute temperature, $\alpha_{ia}(h\nu,T)$, and $\alpha_{ie}(h\nu,T)$ are the components associated with the absorption and the emission processes respectively:

$$\alpha_{ia}=\frac{F_i(h\nu-E_g(T)+k\theta_i)}{h\nu[\exp(\theta_i/T)-1]} \quad (3.21)$$

$$\alpha_{ie}=\frac{F_i(h\nu-E_g(T)-k\theta_i)}{h\nu[1-\exp(-\theta_i/T)]} \quad (3.22)$$

The sum is taken over the four types of absorption processes whose phonon energies are found to correspond to temperatures of 212, 670, 1050, and 1420 K.

The function $F_i(x)$ can be written as:

$$F_1(x)=\begin{cases}0.504\sqrt{x}+392(x-0.0055)^2, x\geq 0.0055;\\ 0.504\sqrt{x}, 0\leq x\leq 0.0055\\ 0, x\leq 0\end{cases} \quad (3.23)$$

$$F_2(x)=\begin{cases}18.08\sqrt{x}+5760(x-0.0055)^2, x\geq 0.0055;\\ 18.08\sqrt{x}, 0\leq x\leq 0.0055\\ 0, x\leq 0\end{cases} \quad (3.24)$$

$$F_3(x) = \begin{cases} 536x^2, x \geq 0; \\ 0, x \leq 0 \end{cases} \tag{3.25}$$

$$F_4(x) = \begin{cases} 988x^2, x \geq 0; \\ 0, x \leq 0 \end{cases} \tag{3.26}$$

The free carriers related absorption:

For lightly doped Si, the free carrier absorption can be written as:

$$\alpha_{FC} = 4.15\times10^{-5}\lambda^{1.51}T^{2.95}\exp(-7000/T)$$

It has been found from the experimental data (for example, Sato's data[34]) that the exponents of λ and T are parameters that can be adjusted to fit the actual data.

For heavily doped Si, the high-concentration of free carriers can be treated as plasma. When the temperature is not very high (<500°C), the absorption coefficient from free carriers can be written in empirical formula:

$$\alpha_{FC} = c1\lambda^2 + c2 \qquad \alpha16 = 2.6\times10^{-17}N_e + 1.9$$

$$c1 = 0.6944(\alpha20 - \alpha16) \qquad c2 = \alpha16 - 2.56c1$$

$$\alpha20 = 3.8\times10^{-17}N_e + 2.0$$

Where Ne is the concentration of carriers, which can be written as:

$$N_e(T) = N\left(\frac{1}{2} + \sqrt{\frac{1}{4} + \left(\frac{1.45\times10^{10}}{N}\right)^2\left(\frac{T}{300}\right)^3\left(1.48\times10^{18}\right)^{1-\frac{300}{T}}}\right) \tag{3.27}$$

N is the doping concentration.

For heavily doped Si and at high temperatures, in the long wavelength range, both n and k will be mainly controlled by the free carrier plasma model. A different model will be used to calculate n and k:

$$n_d^2 - k_d^2 = n_p^2 - \frac{4\pi N_e e^2 / m_e}{\omega^2 + g^2} \tag{3.28}$$

$$n_d k_d \omega = \frac{2\pi N_e e^2 g / m_e}{\omega^2 + g^2} \tag{3.29}$$

Where, Ne is the concentration of carriers, g is damping constant rage from 10^{12} to 10^{13}. Figures 3.3 a and b show the measured transmission and reflection of two different samples, Also shown in these figures are the calculated spectra from the above model. Near perfect match between the two sets of data can be observed.

The above model has also been used in the calculation of emissivity of Si wafers[35]. Figure 3.4 shows the calculated the measured emissivity data from Sato[34]. The calculated emissivity from this model is also shown in the figure. It can be seen that two results match very well.

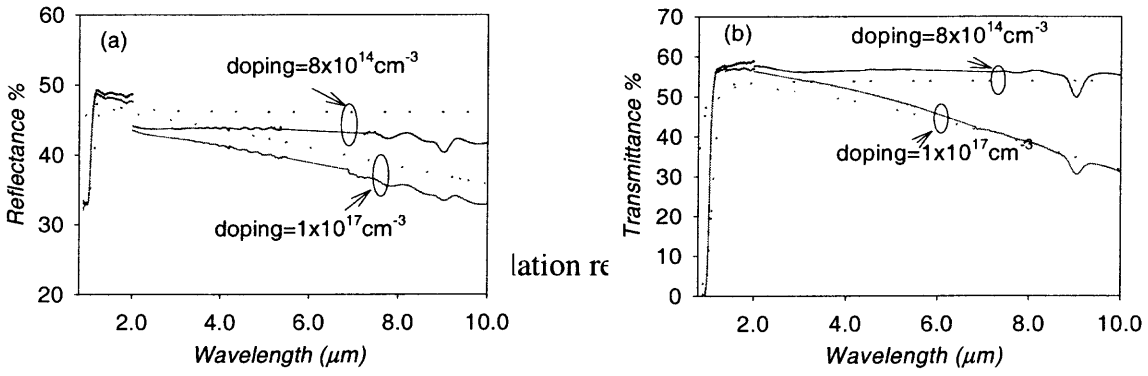

Figure 3.3. A comparison of the calculated and the measured reflectance – (a) and transmittance,- (b), for two samples of different dopant concentrations. The dotted and the solid lines correspond to measured and calculated data, respectively. Wafer thickness = 350 μm.

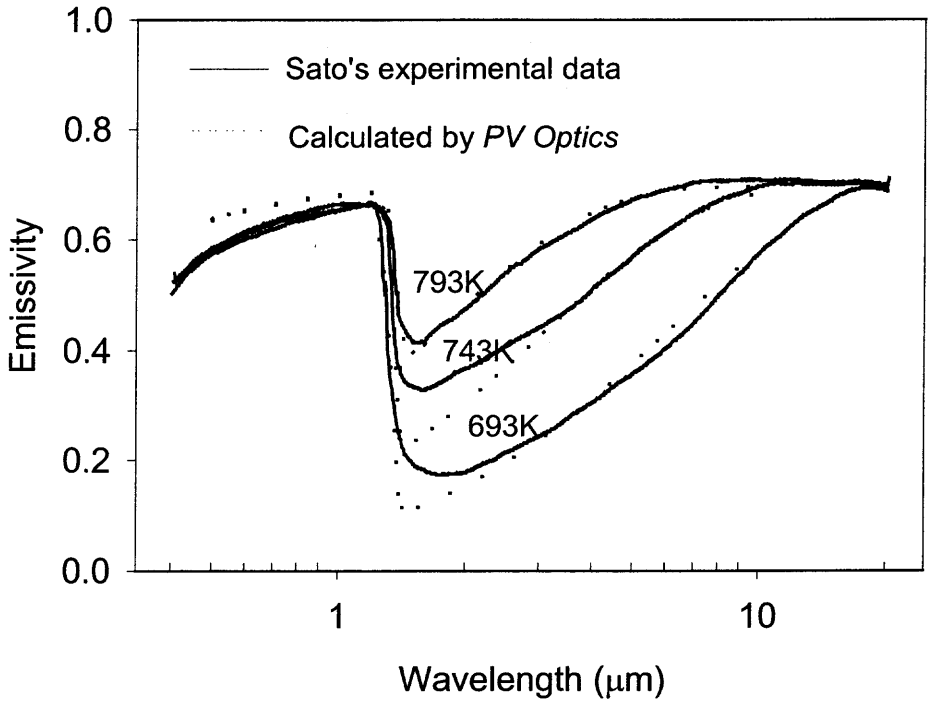

Figure 3.4. Comparison of our calculation results of emissivity and Sato's experimental data.

3.3 The optical design of the cell

The basic structure of our cell is shown in Figure 1.3. In this section, the optics-related features of this cell will be discussed and the best configuration of the cell will be determined through calculations.

3.3.1 What will happen when the thin film is used?

The cells that are being developed in this study use thin poly-Si semiconductor layer as the active layer. When the cell becomes thinner, the distance by which the light beam travels inside the semiconductor layer also decreases if the surfaces of the device are planar. Therefore the MACD should also decrease when the thickness declines. Figure 3.5 shows the calculated MACD as a function of cell thickness for a double side planar

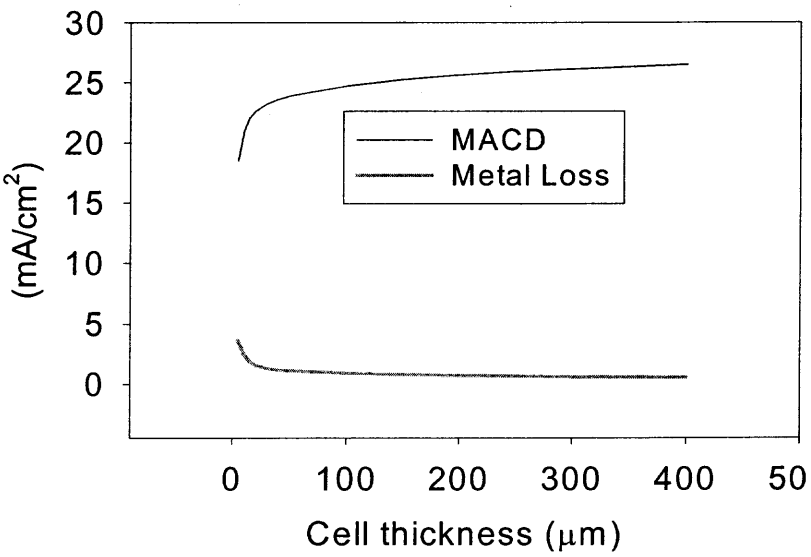

Figure 3.5 The calculated MACD and Metal Loss as functions of cell thickness for double-side polished Si solar cell show in Figure 3.6.

single-junction Si/Al cell. The details of the structure are shown in Figure 3.6. Also shown in Figure 3.5 is the calculated Metal Loss as a function of thickness.

Several conclusions can be drawn from this figure:

1. The MACD will decrease when the thickness of the cell decreases. Further, it will drop more quickly when the thickness of the cell is less than 50 μm. (This thickness can be a dividing point between "optically" thick and thin cells.). For thinner cells, light-trapping features must be included in the design of the cell to get acceptable MACD.

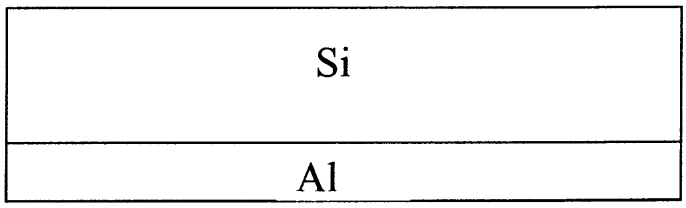

Figure 3.6. The structure of the double-side polished cell used in the calculation.

2. While the MACD reduces with decreasing thickness, the Metal Loss will increase. For thick cells, metal loss can be ignored (it is only less than 5% of MACD), but it must be taken into account for thin cells. Metal loss will be more than 15% of the MACD in thin cells (in other words, if the Metal Loss could be somehow eliminated in thin flim cells, the Jsc would be increased by almost 15%). The reduction of metal loss is also an important issue in the design of a thin film solar cell.

3.3.2 The surface condition and thickness

As pointed out in the introduction to this chapter, in order to increase the photon absorption in thin films, non-flat surface/interfaces need to be adopted. Figure 3.7 a-d shows the calculated optical properties of the cells with the basic structures shown in the inserts of these figures. The MACD and Metal Loss under different conditions are also denoted in these figures. In this calculation, the thickness of the cell considered is 10 μm and the back contact metal is Al. The texture height is 1.2 microns. From this figure, it can be seen that as long as a textured surface is used, the MACD of the device will be higher than that of double-side planar cells, even if metal loss is higher in some cases.

Another observation that can be made from Figure 3.7 is that the MACD will be improved more (about 30%) in double-sided textured or front side textured / backside planar cells. Double side-textured cell will yield the highest MACD. This conclusion suggests that double side textured or front side textured structure should be used in the design of solar cells.

To understand the influence of thickness of a single junction cell on the MACD and Metal Loss, we have performed a series of calculations on differently configured cells. The calculated MACD and Metal Loss are shown as functions of thickness of the cells in

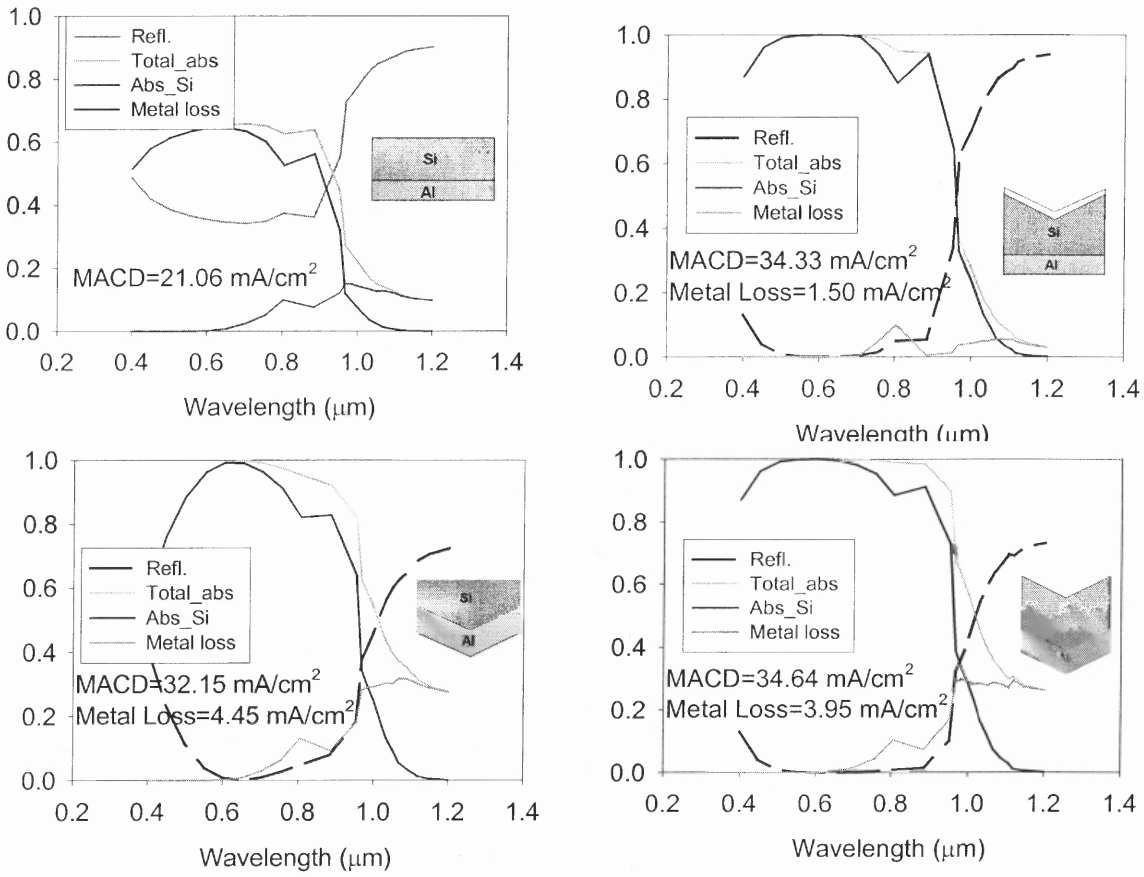

Figure 3.7. Calculated optical properties of a single junction cell under different surface configurations. The cell structures are shown in the inlet of figures.

Figure 3.8 and Figure 3.9 respectively. Three surface configurations are considered: front side textured / back side planar (FTBP), front side planar / backside textured (FPBT) and double side textured (DT). Here, the texture height is 1 μm. Several data points from Keneka's experimental results of Jsc are also shown in Figure 3.8. The calculated results match the experimental data very well. This indicates the accuracy of our calculations.

As we have pointed out, the MACDs in FTBP and DT cells are much higher than that of FPBT cells although the Metal Loss of DT cells is not too different from those of FPBT cells. It can be seen in Figures 3.8 and 3.9 that when the thickness of the cell is in excess of 10 ~ 15 μm, the MACD will not increase much when the cell is made thicker. Thus,

from the view of optical design, the thickness of thin film solar cells should be around 10~20 μm to obtain maximum benefit.

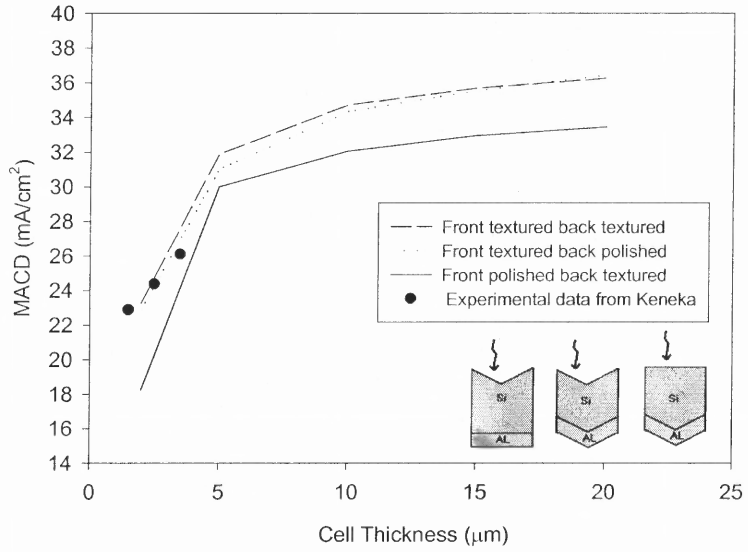

Figure 3.8. Calculated MACD vs. Thickness at different surface configurations shown in the inlet of the figure.

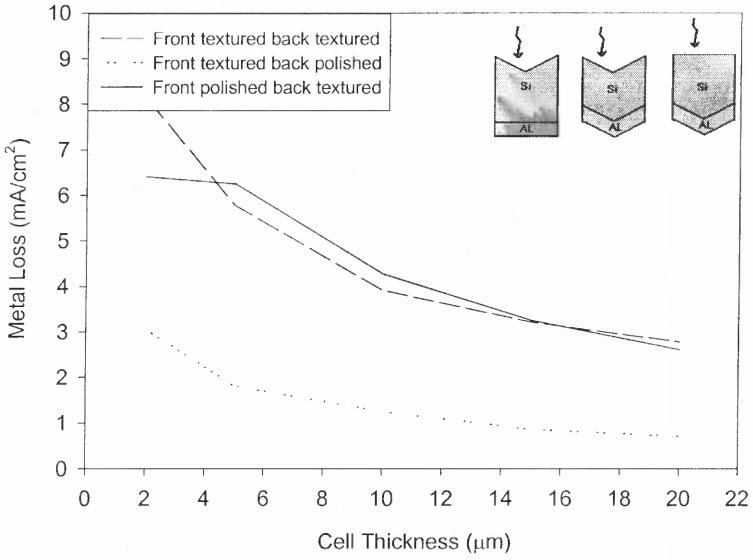

Figure 3.9. Calculated Metal loss vs. thickness for different surface configurations

3.3.3 Detailed study on texturing

There are many processing techniques that can produce texturing in the cells. The results from various methods can be greatly different from each other. In this subsection, we

will discuss the influence of texturing on the properties of thin film solar cells. For the pyramid-shaped texture pits, three parameters will control the properties of the texture structure: the depth, the bottom angle and the density of the texture pits. A set of calculations is performed on the cell structures shown in Figure 3.6 but with different texture configurations.

Before we present the results of calculations, the terminology used in the text will be described. The pyramid-shaped pits on the textured surface are just simply called "texture pits". The geometry parameters of the texture pits such as the depth of the texture pits, and the bottom angle of the texture pits are illustrated in Figure 3.10. When the density of the texture pits is investigated, the ratio between the area of the textured part and the

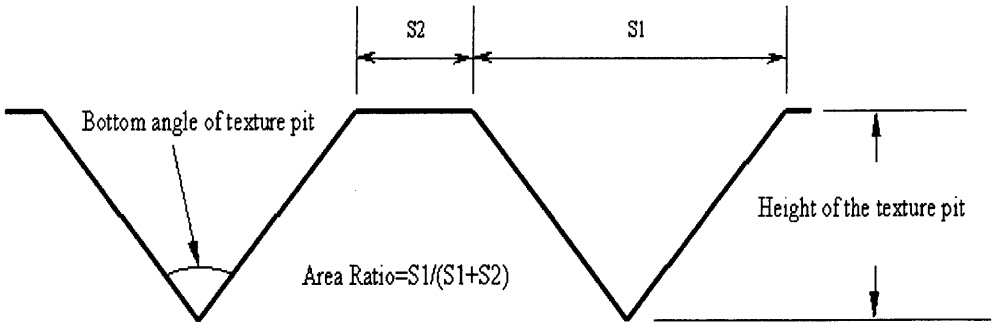

Figure 3.10. The geometry and the terminology used in the texture shape study.

whole area is called "area ratio", as shown in Figure 3.10 (in which the "area" of a region is actually the length of the corresponding region).

a) Influence of the texture height on MACD

Here we are going to investigate the effects of the depth of the texture on the properties of the device. The angle of the texture bottom will be kept unchanged at 70.4° (which is the angle normally obtained by etching methods) but its height will change from 0.1 μm to 2 μm, and the whole surface of the cell is assumed to be covered by pits.

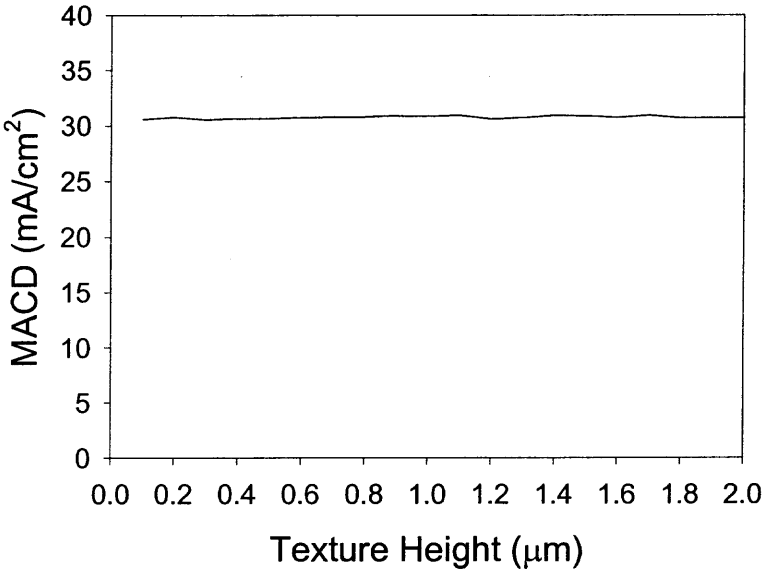

Figure 3.11. The calculated MACD as a function of the height of texture pits.

Figure 3.11 shows the calculated MACD as a function of the texture height. It can be seen from the figure that the MACD does not change too much with the texture height when the bottom angle is kept unchanged. This indicates that very shallow texture pits can be used in the device without degrading the device performance. This conclusion is important to the thin film cell structure, which does not have the luxury of making deep pits on them.

b) Influence of the bottom angle of the texture pits on MACD

The second case investigated here is the influence of the bottom angle of the pits on the cell performance. Unlike the previous case, the height will not change, but the bottom angle will change from 60 degrees to 120 degrees, as shown in Figure 3.10.

Figure 3.12 shows the calculated MACD as a function of the bottom angle of the texture pits. The height of the texture pits used in this calculation is 1μm. From these results, it can be seen that MACD will drop by about 30% when the bottom angle changes from 60 degree to 100 degrees. Therefore, to get better performance, "sharper" texture pits should be used in the cell design.

c) Influence of density of the pits:

In some processing techniques, the texture pits cannot cover the surface totally. This example will investigate the relation between the optical properties of the cells and the density of the pits.

To evaluate the influence of the pit density on the overall performance, the relations between the MACD / Metal Loss and the texture pit density are also evaluated. The results of these calculations are shown in Figure 3.13.

Apparently, linear relations exit between MACD / Metal Loss and area ratio. The MACD

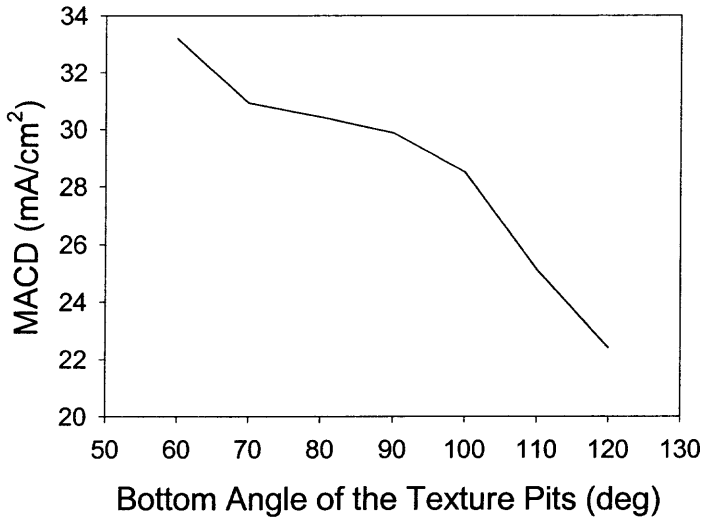

Figure 3.12. The calculated MACD as a function of the bottom angle of texture pits

can be written as a function of "textured area" in the form as:

$$MACD\ (in\ mA/cm^2) = 22.04+0.0984*area\_ratio\ (in\ \%) \quad (3.30)$$

And the metal loss can be written as:

$$Metal\ Loss\ (in\ mA/cm^2) = 1.897+0.013*\ area\_ratio\ (in\ \%) \quad (3.31)$$

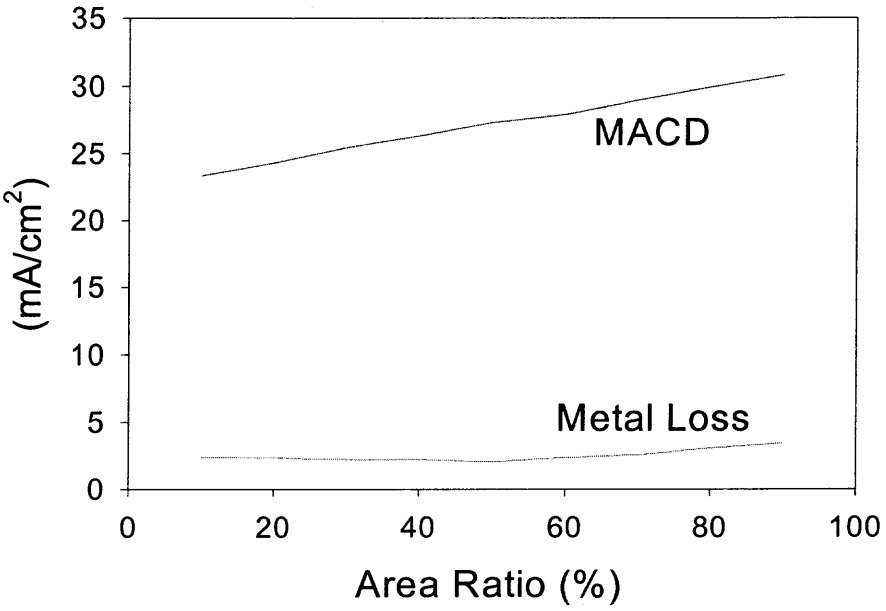

Figure 3.13. Calculated MACD and Metal Loss as functions of Area Ratio.

d) Summary: the shape of the texture pits:

From the last three examples, the ideal textured surface should have high density of textured pits, and the pits should be as "sharp" as possible. On the other hand, the depth of the pits will not change the performance of the device too much. Thus, the ideal texturing process should give dense, sharp and shallow pits.

3.4 From optical model to electronic model: A discussion

In the electronic model of the solar cell, one needs to determine the generation rate at ANY point inside the device in order to solve the continuity equations. However, it is not convenient to determine the distributions of the light intensity (hence the generation rate)

inside the device from light tracing technique although it can reveal fairly precise overall properties of a device. To find the light intensity at a particular point inside the device, we need to register every beamlet passing over this point and/or its nearby region, and then add up the intensities of all of them. This will take tremendous computing power if we want to count a large number of light beams for enough precision.

An alternative way to obtain the distribution of the generation rate is to solve the Maxwell's equations with different boundary conditions inside the device to get the amplitude of the electric field. Then the intensity of the light can also be calculated. By this way, the distribution of the photon number can be determined with fairly high accuracy, although this method may not be suitable for calculating the overall optical properties (for example, T, R and absorption) of the device.

3.5 Conclusions

From the analysis performed in this chapter, we can get some conclusions on the structure of the thin film solar cells:

1. The thickness of the cell should be larger than 10 μm in order to get satisfactory Jsc.
2. The best structure will be front surface textured / backside polished or surface textured / backside textured.
3. The texture pits should be as sharp as possible, and should occupy the entire surface of the cells.

CHAPTER 4

ELECTRICAL MODELING / DESIGN OF SOLAR CELLS ON NON-PERFECT MATERIALS

4.1 Introduction

In this chapter, we will concentrate on the electrical design of thin film μc-Si solar cells. As described in the previous chapters, proper modeling software is the most important tool in the design of a solar cell. Currently, there are various kinds of commercial software that can do almost perfect modeling of electronic properties for solar cells fabricated using single-crystalline materials. However, the device that is being developed in this project is based on thin film μc-Si, which has electrical properties that are very different from single-crystal Si (sc-Si). The commercially available PV modeling software is not suitable to model devices based on μc-Si materials. Furthermore, although sc-Si solar cells usually have much better performance, PV industry prefers using low-cost materials and low-cost processing techniques in solar cell production so that the final cost of the device can be reduced. Unfortunately, low cost materials / low cost processing can introduce many defects into the materials and devices. Proper modeling tools need to be developed for modeling solar cells fabricated on non-perfect materials to assist in the electrical design of the cells.

Electrical modeling of non-perfect materials/devices depends on the understanding of the nature of defects inside materials and their influence on devices. An enormous amount of experimental and theoretical work has been performed to explore the effect of defects on the properties and performance of semiconductor materials/devices. However, only a few theoretical models[36] that relate the properties of defects to the device performance

have been developed. The major difficulties in developing such models arise from the following:

1. The electronic properties of the defects in the semiconductor are still not fully understood.
2. The non-uniformity caused by these defects over large area will make the solution of traditional device modeling equations (A combination of continuity-Poisson equations) very difficult. For samples that have different regions with different properties, only numerical methods can be used to solve differential equations, and at least a 2-D model should be used.

To overcome these difficulties, one must have:

1. Enough information about the electronic properties of the defects (including impurities, dislocations and grain boundaries) in semiconductor materials.
2. Models to describe the defects inside materials and devices.
3. A numerical analysis tool to handle the non-uniformity in materials and devices.

Additionally, as we have pointed out in the previous chapter, a sophisticated optical model which can handle the complex optical designs of today's PV modules is also necessary for a successful electrical modeling of solar cells.

Currently at NREL, a new modeling program, which aims to achieve these goals, is being developed. It is based on several modeling software/programs that are already written by our group, including:

1. A network model[36] that can handle the non-uniformity of large-area devices and materials

2. An optical modeling software that can calculate the optical properties of devices – PVOPTICS[11].
3. A finite element analysis program that can calculate the carrier distribution of large-area non-uniform materials by solving continuity equations.

The major objective of the work described in this chapter is to extend the third product to a modeling program for devices built on large-area non-uniform materials. In this thesis, this modeling program is used to find out the least-acceptable quality of materials in the design of the cells. It is also used to analyze the minority carrier lifetime in non-perfect materials.

It should be pointed out that the purpose of this chapter is to establish a way to relate the properties of defects to those of the final device built on large area materials rather than to develop commercial modeling software. The model and the software presented here may seem to be premature although it does provide insight into the physics involved in the devices. Equally important is that this work is device application oriented instead of being oriented towards materials research. Thus, the detail of the materials is not emphasized.

The chapter will be organized as follows. First the origin and the physical nature of defects inside PV materials will be described. Then the electronic properties of defects in PV materials are reviewed to help in establishing the defect model. This is followed by a discussion on the model calculating the effective lifetime in large area non-uniformity materials. The device model will be presented after the discussion of the lifetime model. The final section will be the summary of the chapter.

4.2 Defects in PV materials

The defects in PV materials can be divided into three categories: grain boundaries, impurities and other defects. In this subsection, the source and properties of these defects will be reviewed.

a) Grain boundaries:

In order to avoid the high cost of growing single-crystal Si ingot, PV industry chooses growing poly-Si bulk materials. Making single Si thin-films is also very costly. Thus, most of the thin film devices are built on a-Si or micro-crystalline Si films. The grain boundaries (GBs) are major defects in most PV Si materials.

It has been observed that atoms line up at the grain boundary in an ordered way, forming a sublattice structure. There are also large size defect points at the GBs[37]. These defects reveal a local stress field and a charge cloud at broken bonds. Figure 4.1 shows a TEM picture of the boundary.

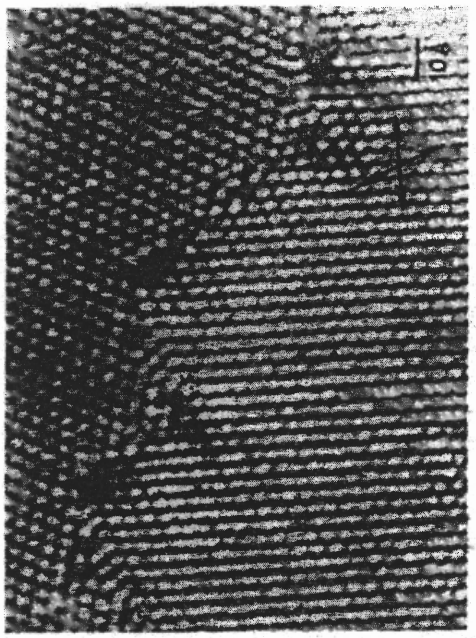

Figure 4.1. An TEM image of grain boundary.

b) Impurities:

PV manufacturers use low-grade feedstock consisting of post-scrap, off spec, and remelt ; most of these materials are rejects from microelectronic industry. The impurities present in the feedstock are carried into melt and into the grown crystal. In general, PV starting material has a high impurity content. Due to low-cost processing techniques utilized in PV industry, impurities could also be brought into the Si in almost every step during material and device processing. Typically, these materials contain C and/or O at near-saturation levels, transition metals in the range of 10^{12}–10^{14} cm^{-3}, and a host of other impurities such as Ti and Va.

c) Dislocations:

PV materials have high concentrations of quench-in, non-equilibrium, and point defects. In some cases, a portion of the ingot may acquire high density of crystal defects (primarily dislocations) and even loose the crystallinity and become multi-crystalline.

d) Defect clusters:

It has been noticed that low-quality μc-Si substrates have a tendency to form clusters of defects. Figure 4.2 is a map of a typical, 4.25in×4.25in, commercial, multicrystalline PV-Si wafer. The wafer has an average defect density of about 10^5 cm^{-2}. However, as can be seen in the figure, there are localized clusters of defects where the defect density can exceed 10^7 cm^{-2}. Previous work has shown that such defects consist of network of dislocations, stacking faults and grain boundaries[38]. Detailed analyses have shown that such defect clusters are sites of impurity precipitates. Figure 4.3 shows a picture of defect clusters in PV materials.

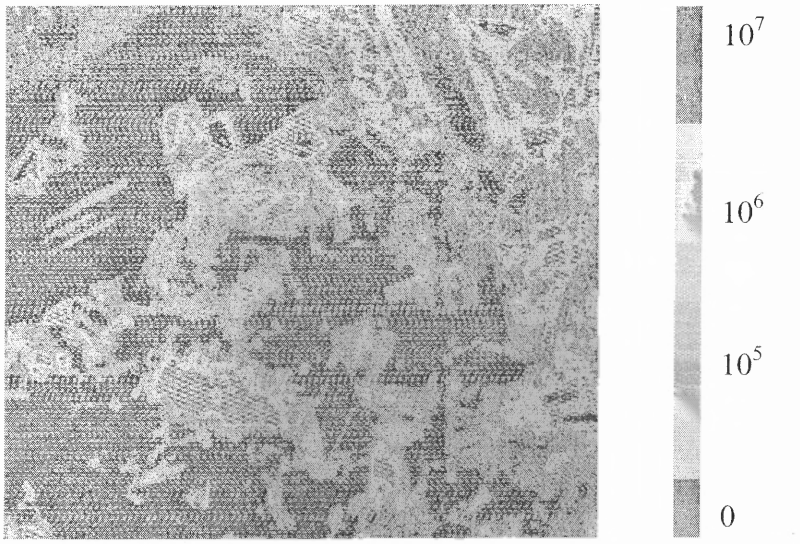

Figure 4.2. A defect map of a 4.25-in x 4.25-in commercial mc-Si wafer. Some high defect density regions can be observed in the sample.

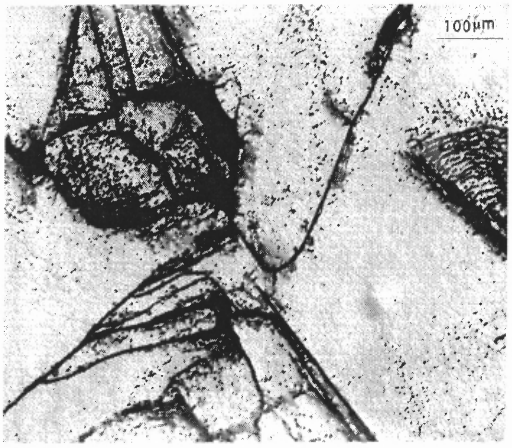

Figure 4.3. Photograph showing chemically delineated structure of a defect cluster.

4.3 Electronic properties of defects

Defects influence the electrical properties of materials and devices through four processes:

First, the energy levels introduced by the defects can act as recombination centers or traps of the carriers. These energy levels can be characterized by three features: a) the density

of the energy levels, b) the distribution of these levels over the energy band gap, c) the capture cross section of the energy level.

Second, The extra energy level itself or the carrier(s) it trapped will bring extra charges to the area around defects. The trapped carriers can come from the neighboring region, or from the extra carriers generated by some other method (for example, light illumination). In most cases, each energy level will carry only one or two +/- electron charge(s).

Third, defects are usually not uniformly distributed inside the material. The interchange of the carriers between different regions that have different defect levels causes the redistribution of the carriers. This in turn will change the properties of the materials / devices.

The fourth process may be the least considered process in the modeling of the defects in PV materials—the scattering of carriers at the defects. This effect may be neglected for low-speed devices like Si solar cells. But, in solar cells fabricated using high-mobility materials (for example, GaAs), the scattering becomes significant. In the high electric field region of non-uniform materials, this effect should also be taken into account.

As we can see from the above discussions, in most cases, defects impact the properties of materials or devices through the energy levels they introduce. For this reason, the energy levels caused by different kinds of defects will be reviewed first in this section. Based on this review, a general picture of the defects will be extracted. The properties of energy levels related to grain boundaries and impurities will be reviewed in detail. For the other kinds of defects, there is no known definite relation between the structure of defects and the energy levels.

Whenever the periodicity of the lattice is disrupted, extra energy levels in the energy band gap could be created[39]. The impurities in the semiconductor will also introduce energy levels into the system. Theoretically, the effect of any defect can be written in one or more terms in the Hamiltonian of the lattice system. When the corresponding Shrödinger equation is solved, this "disturbed" Halmiton will yield extra eigen-values, which correspond to the additional energy levels generated by the defects in the system. The study of defect energy levels was pioneered by Bardeen's work on surface states[40]. Since then, numerous theoretical works have been carried out on the extra states introduced by grain boundaries and impurities. Most of this work concentrated on the origin and the value of the extra states. Many experimental techniques such as quasi-Fermi-level and capacitance transient measurement, admittance spectroscopy, deep level transient spectroscopy (DLTS), capacitance transient, Hall effect, etc., are used to measure the position and the cross section of the extra energy levels.

4.3.1 Extra Energy Levels Caused by Grain Boundaries

The discontinuity of the lattice structure at the grain boundaries (GB) causes a change in electronic properties of materials in these regions. In spite of the apparent lack of information relating the electronic properties to the lattice structure in the grain boundary region, the factors influencing the energy band structures at the grain boundaries can be divided into three interactive categories[41]. They are : (1) lattice strain caused by the lattice mismatch at the GBs; (2) dangling bonds; (3) enhancement or depletion of available impurities in the boundary region. Some experimental results[42] suggest that the dangling bonds are the major defects at the GB that influence the electronic properties. A research paper on the calculation of the energy states caused by dangling bonds was

published by Heine[39]. The properties of the extra energy states induced by these factors will decide the behavior of the carriers on the GB and in its neighboring regions.

Many experiments have been conducted to measure the interface state properties at the grain boundaries, an extensive review of which can be found in the paper written by Grovenor[43]. Several conclusions can be drawn from these experimental results:

1. The measured results are diversified and strongly depend on the measurement methods adopted.
2. The interface state density ranges from about 10^9 to $2x10^{15}$ $cm^{-2}eV^{-1}$.
3. The distributions of the energy levels could be uniform, U-shaped continuous, localized at midgap or Gaussian centered at some point(s) in the energy gap.
4. The cross section of these states ranges from 10^{11} to 10^{14} cm^2.

Since the properties of the interface states of grain boundaries are not well defined by experimental data, many authors just use their own interface states model to carry out theoretical calculations. In Card and Yang's paper[44], the properties of grain boundary interface states are assumed to be the same as that of surface states of semiconductors[40, 45 46], which are characterized by a specific energy level, ϕ_0. Fossom and Lindholm[47] treated the grain boundaries as surfaces characterized by distributions of donor $N_{ST}^{D}(E)$ and acceptor $N_{ST}^{A}(E)$ surface states within the bandgap. The details of $N_{ST}^{D}(E)$ and $N_{ST}^{A}(E)$ are ignored in their calculations. In Seager's model[48], the interface states distribute uniformly above (for n-type materials) or below (for p-type materials) the Fermi level. A Gaussian distribution of interface states was considered in Joshi and Bhatt's work[49]. In Green's work[50], the details of the grain boundary interface are

ignored. Although all these models are different from each other, some of the common features can be concluded as follows:

1. There is an energy level ϕ_0, to which if the Fermi level equals, the total net charge on the interface will be 0.
2. The state distribution can be defined by a specific function.
3. The net charge on the interface states will be negative if the Fermi level is higher than ϕ_0, otherwise the net charge is positive.

These common features will be the basis of our modeling of the device based on multi-grain materials.

4.3.2 Extra energy levels introduced by impurities

The impurities in the semiconductor can introduce impurity energy levels. Although many types of element impurities can cause extra energy levels in the bandgap[51], only several of them, such as Fe, H, Al, Ni and Cu are of interest to semiconductor industry. This is because the other elements are either not easy to incorporate into the semiconductor during processing or the energy levels related to these elements do not act as active recombination centers or trapping levels. The properties of the energy levels related to those "trouble-making" elements will be discussed separately in the following paragraphs.

Iron:

Due to their similar electronic structures, transition atom (TA) (such as Fe, Co, Cr, Ni, Cu etc.) impurities in semiconductors are expected to be alike in electronic properties[52]. Among them, the properties of iron atoms in Si were investigated most extensively.

Iron in semiconductor has been extensively studied, both experimentally and theoretically, in the past thirty years. A review of these works is given by Istratov, Hieslmair and Weber recently [53]. Iron can exist in Si as an interstitial and as complexes with other defects[53]. The interstitial Fe will introduce a donor level at $E_T \approx E_V + (0.375 \pm 0.015)$ eV[54] at room temperature. The hole capture cross-section of interstitial iron can be written as[53 55 56 57] (in cm^{-2}):

$$\sigma_p(Fe_i) = (3.9 \pm 0.5) \times 10^{-16} \times \exp(-\frac{0.045 \pm 0.005 eV}{k_B T}) \quad (4.1)$$

Where, k_B is the Boltzmann constant, and T the temperature.

The electron capture cross-section of Fe was measured[58 59] as $\sigma_n = 4 \times 10^{-14}$ cm^{-2}.

Since interstitial iron is positively charged in p-Si at room and slightly elevated temperatures, it tends to form pairs with negatively charged defects, such as shallow acceptors. More than 30 complexes can be formed between iron and other defects, and about 20 deep levels are associated with these complexes. The positions of these energy levels vary from about Ev+0.07 eV to Ec-(0.26±0.03) eV[53]. They could be either donor levels or acceptor levels. The hole capture cross section ranges from 3.9×10^{-16} to 2×10^{-13} cm^{-2}, while the electron capture cross section can range from 1.5×10^{-16} to $4 \times 10^{-13} cm^{-2}$.

Ni:

Nickel is one of the most poorly understood TA impurities in Si. The reported energy values of electrically active nickel-related levels in Si are highly controversial[60 61 62 63 64 65], as summarized in Figure 4.4. The measured cross sections range from 2.7×10^{-15} cm^2 to around 10^{-20}. Nickel has high diffusivity in Si, so most of Ni impurities will concentrate close to the surface of the silicon.

Cu:

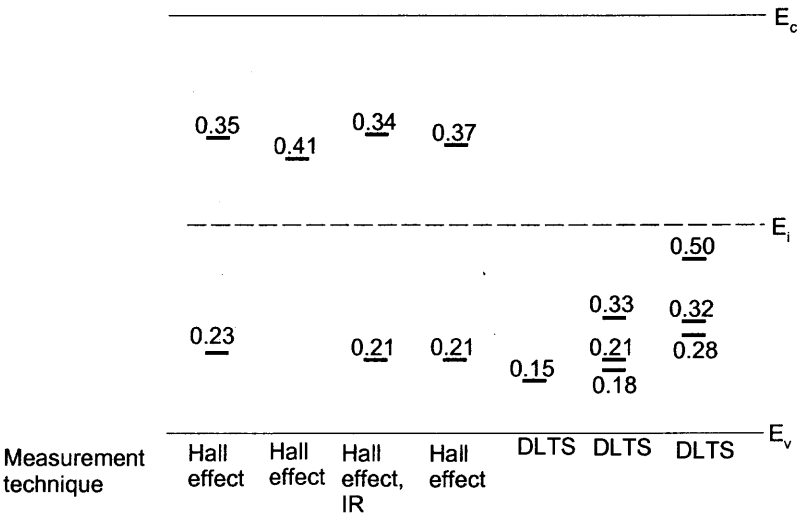

Figure 4.4. Measured energy levels introduced by Ni impurities in Si.

The recombination activity of interstitial copper is not very clear [66]. The cross-section of interstitial copper is about 10^{-17} cm^2. It is expected that the energy level introduced by copper is shallow donor-like[66] copper is not very clear . Copper will also induce several other acceptor-like energy levels inside the bandgap of Si[67], but their recombination properties are not clear. Like iron atoms, copper atoms will form pairs with other atoms in the Si. Precipitates of Cu can cause more severe problems to materials and the devices. On the other hand, because of the high diffusion coefficient of Cu in Si, copper, like Nickel, tends to form surface-near precipitates[68]. Thus the bulk properties of Si will not be degraded by the Cu impurities too severely.

O:

Since the oxygen is incorporated at elevated temperatures during growth, at lower temperatures, the supersaturated oxygen will diffuse and agglomerate into electrically active thermal donors (TDs)[69]. The electrical properties of these TDs strongly depend on the thermal history of the sample[70] [71] [72]. It has been observed that for annealing temperatures ranging from 350°C to 550°C, two families of TDs will be formed: one

having the characteristics of thermal double donor (TDD)[73]; The other consists of single donor with shallower energy levels called shallow thermal donors (STDs)[74 75 76] or ultra-shallow TDs[77]. The energy levels introduced by oxygen often act as traps inside the semiconductor[78]. The interface states at the SiO_2/Si interfaces have important effects on surface recombination. But the mechanisms involved are not very clear.

4.3.3 When the defects are clustered

When the defects are clustered, it is expected that the potentials introduced by different defects may couple with each other if they are close enough spatially. Therefore, some second-order extra energy levels or energy-band-like structure shall be generated.

4.3.4 Recombination centers and Traps:

A defect level may have a "normal" capture rate for one kind of carriers, but an unusually small capture rate for the other. Once this defect level has captured a carrier it "prefers", it takes a longer time for the level to capture another subsequent carrier in order to complete recombination sequence. This energy level is considered as a "trap"[78] in which the carrier captured will introduce extra charges to the local area.

4.3.5 Summary–A general picture of defect energy trapping level in PV Si

As we have seen in the preceding part, the characteristic of the energy levels created by different kinds of defects can be very different from each other. However, we can still draw a general picture of defect energy levels as described in the following:

1. A defect level can be either donor-like or acceptor-like. These two kinds of energy levels can exist in the materials at the same time. But one energy level cannot be both

donor like and acceptor like. Statistically, the amount of donor-like and acceptor-like energy levels should be same.

2. Statistically, the state density of these energy levels can be assumed to be uniform in the band gap since there are many different energy levels being contributed by various sources such as dislocations, impurities and GBs.
3. Defect-generated energy levels are localized inside the materials. The carriers trapped by these levels will not move as freely as the carriers in conduction band (for electrons) and valence band (for holes).
4. The carriers trapped by these energy levels can generate extra charges inside the materials and devices. Since we assume that the amount of two types of energy levels (donor-like and acceptor-like) is same, the net charges on these states should have same sign as that of majority carriers. In the neutral region of the sample, these charges will be compensated by the dopants around them. The entire sample is thus electrically neutral.
5. Normally, the majority carriers trapped by these energy levels will be only a very small part of the total amount of majority carriers. Therefore, the recombination of majority carriers has only negligible influence on the distribution of majority carriers. In the equilibrium state, this recombination will not change the shape of energy bands (include Fermi levels) in semiconductors. On the other hand, the recombination of the minority carriers does have strong influence on the distribution of minority carriers. Normally, the effect of this recombination can be symbolized by minority carrier lifetime.

6. However, in a region that has very high density of trapping levels (for example, the grain boundaries), the majority carrier recombination cannot be ignored. The loss of majority carriers in this region induces the flow of majority carriers from the neighboring regions. This will cause the bending of energy bands around these regions of high defect densities.

4.4 Minority carriers lifetime study of large area defect materials

4.4.1 Introduction

Minority carrier lifetime is one of the most important material parameters in PV semiconductors (also in microelectronic materials). Both Isc and Voc of the device depend strongly on the minority carrier lifetime. In large area non-uniform materials, the carriers can have different lifetimes in different areas of the material and the lifetime could change dramatically over a very small area. The minimum area over which a measuring instrument can give meaningful readings is limited by the precision of the instrument. If the lifetime of the minority carriers changes over a region with area smaller than the minimum area that the instrument can measure precisely, the measured minority carrier lifetime is the effective lifetime over the smallest measurable area of the instrument[79]. To increase the throughput and lower the cost during manufacturing, only large area lifetime measurement is performed for quality control in the production line of solar cells. The lifetime measured in this way is also the effective lifetime over a large area. In this section, we will analyze the properties of effective lifetime in large area non-uniform materials. The models and methods developed in this section will be extended to device modeling in the next section.

The measured effective lifetime of the minority carriers in non-uniform materials depends on the various properties of the material, such as the "real" lifetime distribution in the materials, the surface conditions in the materials, and the interface conditions and so on. The relation between the effective lifetime of the materials and these properties will be discussed in this section. Furthermore, depending on how the minority carriers are generated, the carrier distribution and decay profile can also change, which will yield different effective lifetimes. This phenomenon will also be discussed in this section.

Two major methods are used in the semiconductor industry to measure the minority carrier lifetime — Surface photovoltage (SPV) measurement and photo conductance decay (PCD) measurement. SPV result depends on the amount of steady state carriers while the PCD method measures the carrier decay inside the sample. The analysis in this section will also provide insight into the lifetime measurement of large-area non-uniform materials.

4.4.2 Methodology

Sample Model Considered

The configuration of the samples considered in the calculation is shown in Figure 4.5. This sample can have at least 2 grains, which have different properties, as shown in this figure. There is also recombination on the surface of the sample and at the interfaces of different regions.

To analyze the minority carrier behavior in these multi region samples, we can categorize the regions inside the sample into the following four types according to the amount and properties of defects level inside different regions. Inside different types of regions,

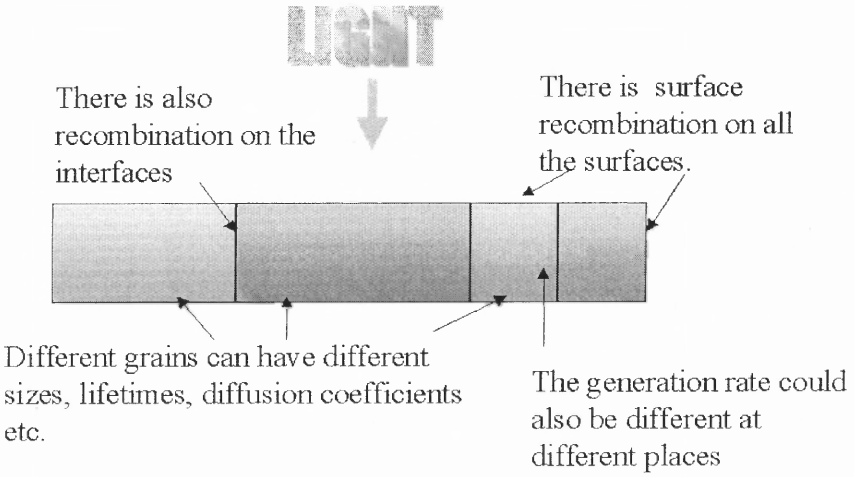

Figure 4.5. A schematic showing the sample investigated in lifetime and device properties analysis

different mechanisms will control the carrier behavior. At the interfaces between these regions, the boundary conditions are also different:

Type I region - The regular regions: In these regions, the recombination of the majority carriers can be neglected, and the extra charges introduced by defect levels are in such a small amounts that they can be neglected.

Type II region - The regions that have extra charges: In these regions, the recombination of majority carriers can be neglected, but the extra charges introduced by defect levels in these regions cannot be neglected.

Type III region -The "dead" regions: In this region, almost all the carriers (both majority and minority carriers) will be recombined. In the modeling, the details of carrier distribution inside this type of regions are ignored because these region do not contribute any free carriers into the system. This type of regions can include grain boundaries or other defect rich regions.

Type IV region: In type IV regions, some of the majority carriers can be recombined. As a result, the Fermi levels in this region will be different from the Type I regions with the

same doping concentrations. Because of the high density of defect levels in type IV regions, it is quite possible that there are also extra charges inside them.

Basic equations

The 2-D continuity equation of the minority carriers inside semiconductors can be written as[51]:

$$\frac{\partial n}{\partial t} = D\left(\frac{\partial^2 n}{\partial^2 x} + \frac{\partial^2 n}{\partial^2 y}\right) + \mu E(x,y)\left(\frac{\partial n}{\partial y} + \frac{\partial n}{\partial y}\right) + \mu n\left(\frac{\partial E}{\partial y} + \frac{\partial E}{\partial y}\right) - \frac{n - n_0}{\tau} + G(x)e^{-\alpha y} \quad (4.2)$$

Where, n is the concentration of minority carriers (either electron or hole), D and α are the diffusion and absorption coefficients, respectively, μ is the mobility of the carriers, E is the electric field possibly involved, τ is the "real" lifetime of the carriers in the local region considered. G is a constant that represents the relation between generation rate and the incident light. D, τ and μ can be different in different regions of the materials.

In regular regions (type I regions), the electric field *E(x,y)* is 0. But in the regions of type II or type III, which have extra charges, these charges will induce electric field inside this region and hence *E(x,y)* will not be 0.

Boundary / Interface conditions

Since we are dealing with multi-region samples, there are two different boundaries – the boundaries of the entire sample, and the boundaries of each region inside the samples. To avoid any confusion we will call the boundary conditions at these two different boundaries as "boundary condition" and "interface condition" respectively.

At the boundary of the sample, the boundary condition is:

$$D\frac{n}{\vec{n}} = Sn \quad (4.3)$$

Where, S is the surface recombination velocity, and all the other symbols have their usual meanings.

At the interfaces between different regions, the interface conditions will be different depending on how the sample model is configured, as described in the following part.

If the sample model has type I or II regions only with grain boundaries between each other, and the grain boundaries can be treated as a surface with specific recombination velocities, at the interfaces, the following interface condition applies:

$$n_1 = n_2 \tag{4.4}$$

$$D_1 \frac{\partial n_1}{\partial \vec{n}} - D_2 \frac{\partial n_2}{\partial \vec{n}} = S n_{1or2} \tag{4.5}$$

Here S is the "effective" surface recombination velocity.

However, if we treat the grain boundaries as a defect rich region (a type III region) with finite width, or there are type III regions other than grain boundaries existing in the samples, the boundary conditions will be different (Figure 4.6). Assume that the

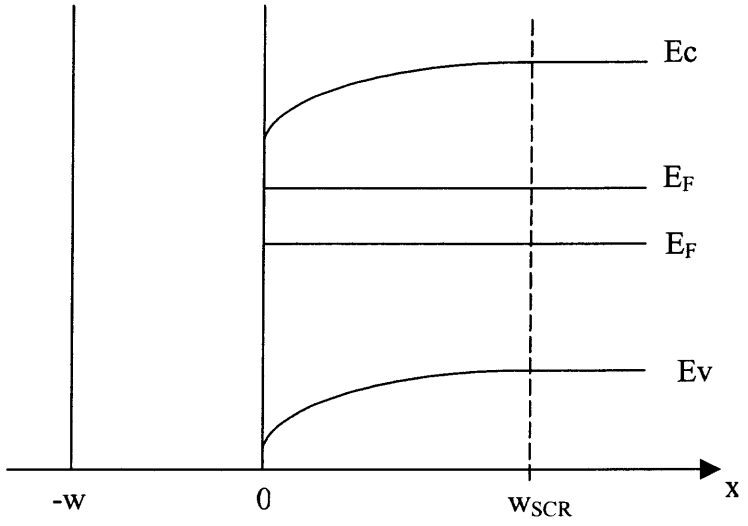

Figure 4.6. The energy band model used for boundary condition analysis around a type III region.

lifetimes of electrons and holes are τ_e and τ_h respectively in type III region. By extending the algorithm of Fossum and Lindholm47 to bulk region, the electron flow (in p-type samples) at the edge of the interface space-charge region can be written as:

$$F_n \approx \frac{1}{4}\frac{w}{\sqrt{\tau_p \tau_n}}\sqrt{N_A * n}, \tag{4.6}$$

Where, w is the width of the "region-like" grain boundaries or the type III region, N_A the doping concentration and n the electron density at the edge of the interface space-charge region.

In fact, in quasi-natural region,

$$F_n \equiv D\frac{dn}{d\vec{n}} \tag{4.7}$$

Interface condition (4.6) is nonlinear. But, in the case of high injection[47], this boundary condition can be written as:

$$D\frac{dn}{d\vec{n}} \approx \frac{1}{4}\frac{\sqrt{\tau_p \tau_n}}{w}n \tag{4.8}$$

At the interface between type IV regions and type I or type II regions, since the Fermi levels are different in these two different regions (IV / I, IV / II), the interface can be treated as a high-low junction. To simplify the problem, this kind of interface will not be considered in this thesis.

Fitting of effective lifetime

In these calculations, the continuity equations are solved to determine the time-dependent minority carrier distribution. Then the total number of generated minority carriers, N, as

a function of time t can be determined. The following definition of the effective lifetime τ_{eff} is used to fit the data in order to determine τ_{eff}:

$$N = N_0 e^{\frac{t}{\tau_{eff}}} \tag{4.9}$$

Where, N_0 is the initial amount of extra minority carriers generated, which is determined by the solution of the steady-state continuity equations. N_0 has the same meaning throughout the text in this thesis. In most cases, the fitting R_{sqr} is larger than 0.99.

Programming

To accommodate the diversity of regions in large-area non-uniformity materials, finite element method (FEM) is used to solve the differential equations. The basic element in the mesh is a rectangle. The density of the mesh is input by the user.

The code of the calculation engine is written in both ANSI C++ and JAVA. The current interface is written in Microsoft® Visual C++™ 6.0. The object-oriented programming (OOP) is also introduced to this program for easier upgrades and maintenance. The mesh, the elements and all the related functions are objects in the program. This feature makes the program compatible with the next-generation network-oriented programming language (for example, JAVA). The program possesses the potential to be developed to an Internet server based commercial modeling software.

As a Windows based software, this program is also user friendly. The user can actually draw his/her region configuration in the Windows. All the material properties and other parameters can be input and edited through the interface. Then, all the results (distribution of the carriers, the depletion of the total number of carriers as function of

time and so on) will be saved automatically according to the project name chosen by the user.

Since there are many data analysis and visualization software available in today's market, this type of data modules are not included in the software. All the output results are in simple ASCII format, which is acceptable in any data processing software.

4.4.3 Results and discussion

The calculated results presented here concern the influence of different material parameters and carrier generation conditions on the effective lifetime of the materials. The effective lifetime is defined in eq.(4.9). Since we assume that the carrier distribution in the sample reaches steady state before the light is turned off, it is expected that the N_0 in eq.(4.9) will be different for different sample configurations. The N_0 under different conditions will also be discussed in some cases. Except otherwise specified, the term "carriers" used here refers to minority carriers only.

The influence of the surface recombination and absorption coefficient on the effective lifetime:

The surface recombination can influence the properties of semiconductor materials strongly even for single crystalline wafers. Figure 4.7 shows the calculated effective lifetime of a uniform sample. The width of this sample is 1cm and its thickness is 300μm. The "real" lifetime of this sample is 10^{-4} s. From this figure, we can see that the effective lifetime can be only 50% of the real lifetime when the surface recombination velocity is 100 cm/s, which is normal in as-grown Si wafers. This indicates that the

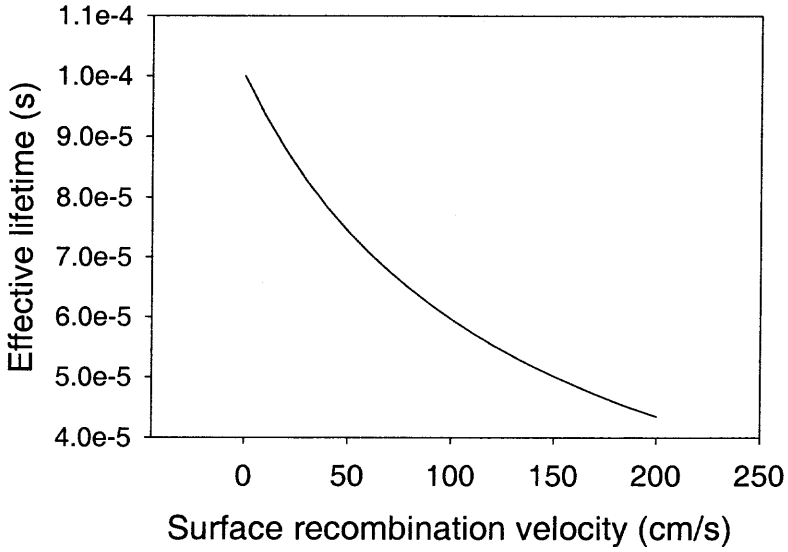

Figure 4.7. Calculated effective lifetime as a function of surface recombination velocity for a single-region sample.

surface recombination can lower the effective lifetime of the minority carriers in the material significantly.

Depending on the wavelength of light used for carrier generation, the distribution of the photon generated minority carriers can be quite different because the absorption

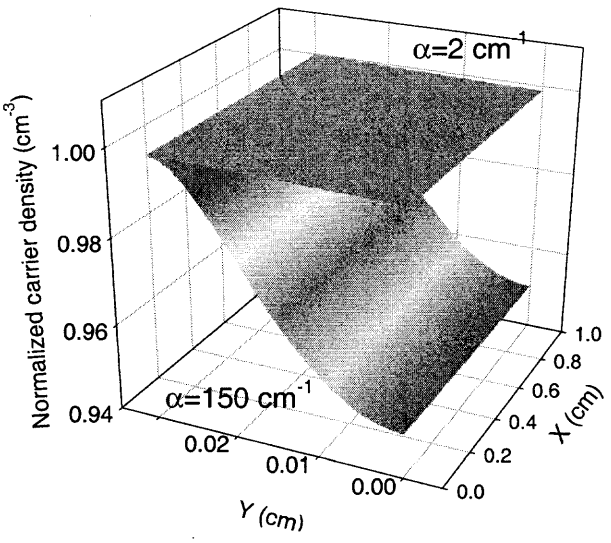

Figure 4.8. The normalized carrier density distribution inside single-region samples with different absorption coefficients.

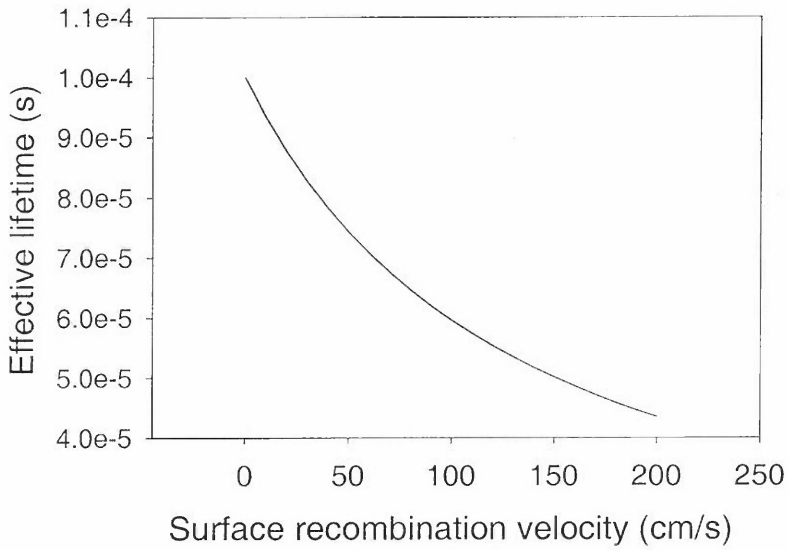

Figure 4.7. Calculated effective lifetime as a function of surface recombination velocity for a single-region sample.

surface recombination can lower the effective lifetime of the minority carriers in the material significantly.

Depending on the wavelength of light used for carrier generation, the distribution of the photon generated minority carriers can be quite different because the absorption

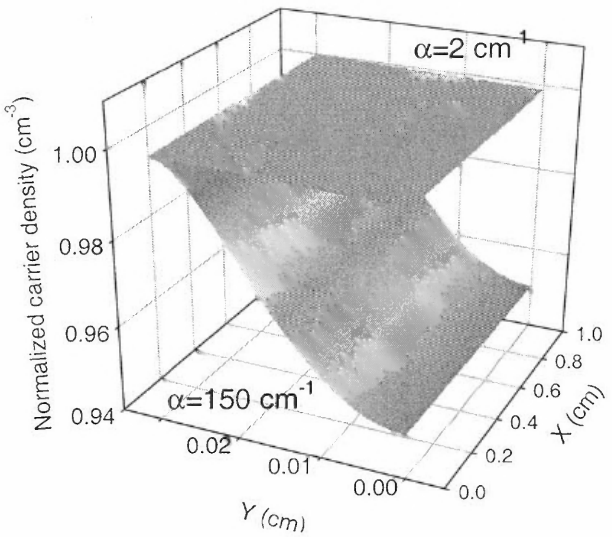

Figure 4.8. The normalized carrier density distribution inside single-region samples with different absorption coefficients.

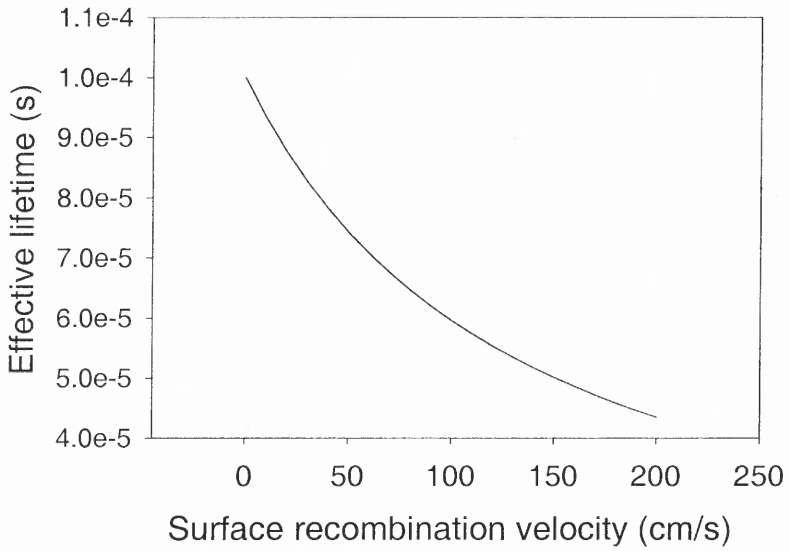

Figure 4.7. Calculated effective lifetime as a function of surface recombination velocity for a single-region sample.

surface recombination can lower the effective lifetime of the minority carriers in the material significantly.

Depending on the wavelength of light used for carrier generation, the distribution of the photon generated minority carriers can be quite different because the absorption

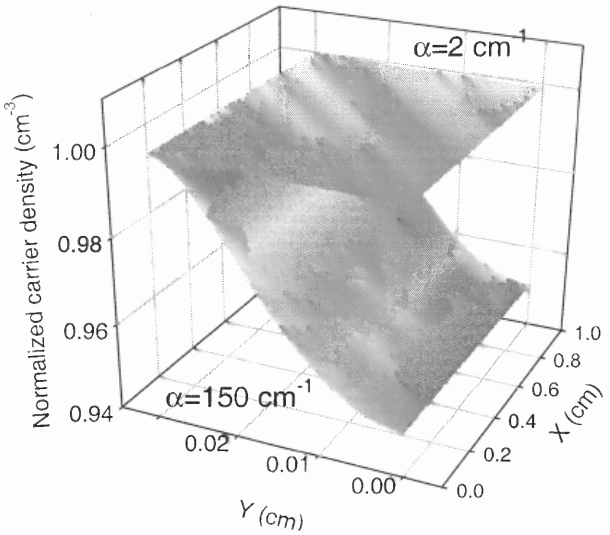

Figure 4.8. The normalized carrier density distribution inside single-region samples with different absorption coefficients.

coefficient of Si can change dramatically at different light wavelengths. Figure 4.8 shows the distribution of the carrier density when the absorption coefficient is 2(corresponding to the light with wavelength less than 1 μm) and 150 (for light with wavelength of >0.6 μm) respectively. Here, the carrier density inside the sample is normalized with respect to the carrier density at the light-incident surface. The sample considered here has the same dimension as the one considered in Figure 4.7. The surface recombination velocity is 0. It can be seen that when the absorption coefficient is large, the carriers are more likely to be generated near the surface. Thus, it is expected that the surface recombination will have stronger influence on the distribution profiles of carriers generated by longer wavelength light. In other words, if we use longer wavelength light to generate the carriers, total carrier amount at the steady state will be more strongly influenced by the surface recombination.

The results shown in Figure 4.9a verify this estimation. This figure shows the steady state carrier amount N_0 as a function of the absorption coefficient (α) and the surface recombination velocity (SRV). It can be seen that when α becomes larger, N_0 changes faster with SRV.

Figure 4.9b shows the fitted time decay constant as a function of α and SRV. The effective lifetime does not change too much with absorption coefficient. This is because when the light is turned off, the recombination and diffusion in the sample decide the carrier decay. As long as the diffusion length is big enough, the decay time constant will not depend on the initial distribution of the carriers, which strongly depends on the absorption coefficient of the samples.

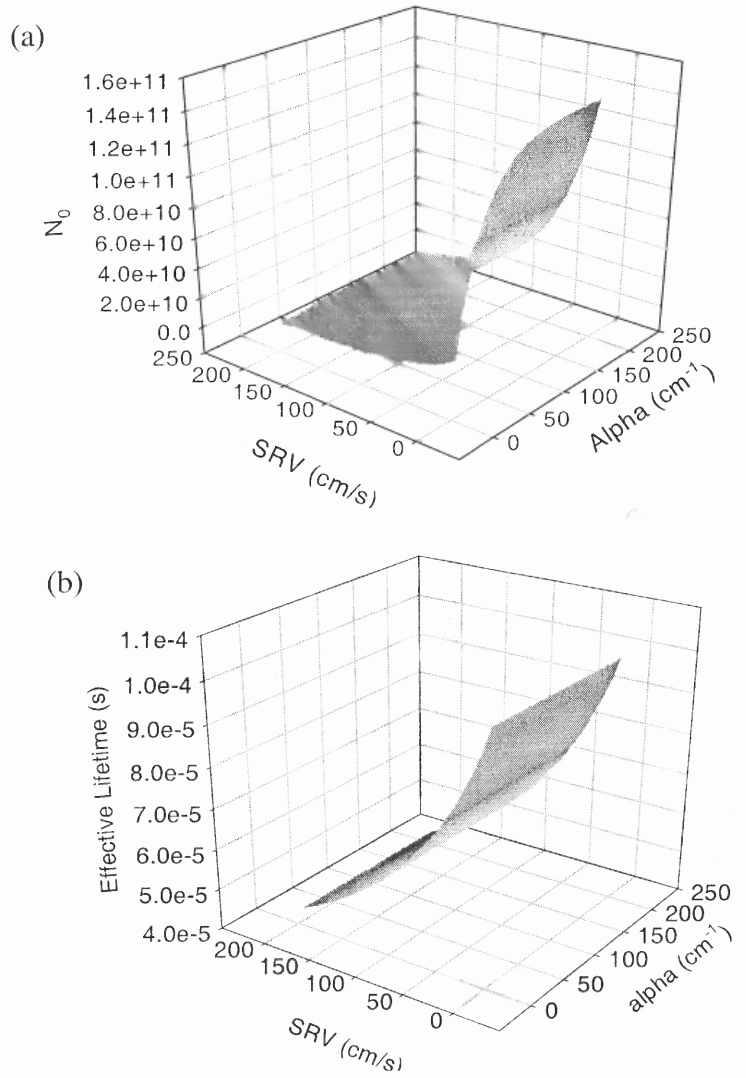

Figure 4.9. Calculated (a) N_0 and (b) effective lifetime as functions of SRV and alpha for a single region sample.

The carrier decay in non-uniform materials:

Before taking up the study of the effective lifetime of minority carriers in non-uniform materials, it is instructive to consider the carrier decay profile in it. To simplify the calculation, we first investigate the simple structure shown in Figure 4.10.

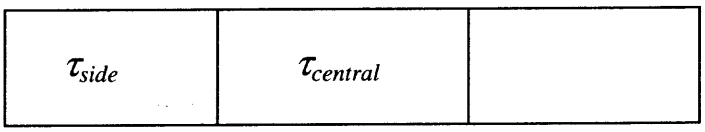

Figure 4.10. A three region non-uniform sample considered in lifetime analysis.

This sample has three regions. The carrier lifetime of the central region is different from that of two side regions. The thickness of the sample is 300 μm, and the width is 1 cm. All the parameters considered have values typical of PV materials. The steady light illuminates the sample from the topside to generate minority carriers. When the equilibrium state is reached, the light is turned off. The distribution of the carriers, the total amount of carriers and its decay profile after the light is turned off will be studied here.

Figure 4.11 shows a time decay curve of the total amount of carriers in the samples after the light stops illuminating the sample. The time axis is in log scale. From this figure, it

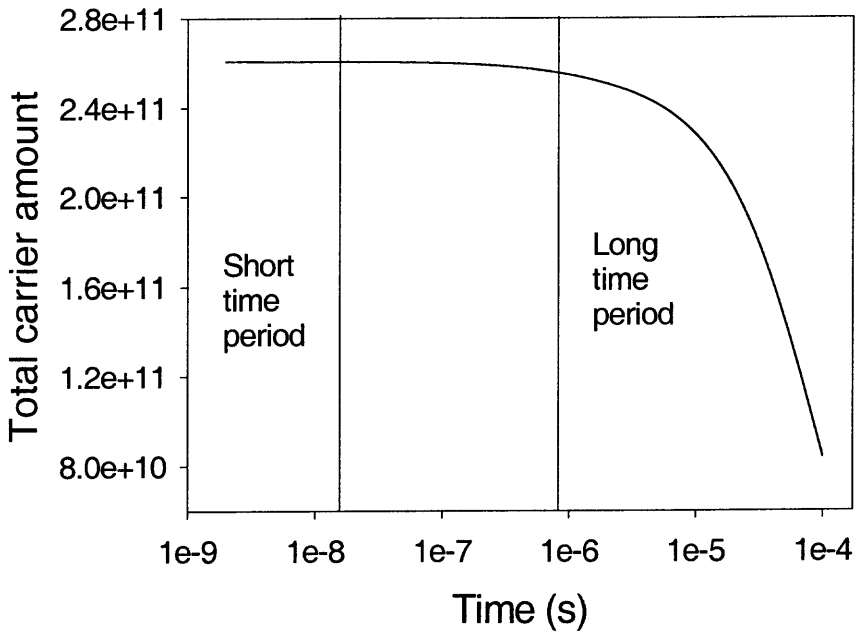

Figure 4.11. The total carrier number inside the sample as a function of time from very short to long time.

can be seen that the decay curve can be divided into two parts with different ramps. This phenomenon is also observed in experiments. It implies that the decay of carriers in the samples follows two different rules as follows. (1) In short time period, the carrier decay is decided by the recombination in the short-lifetime region; (2) In longer time period, it is decided by the carrier exchange between two different regions and the lifetime of the longer lifetime area. Here "short time period" refers to the time period shorter than 10^{-8}s after the light is turned off, and "long time period" refers to the time period longer than 10^{-6}s after the light is turned off.

The explanation of the carrier behavior in the short time period is straight-forward. Figure 4.12 shows the fitted time decay constant (effective lifetime) as a function of the lifetime of the central region ($\tau_{central}$) in the sample structure shown in Figure 4.10. From Figure 4.12, one can see that the effective lifetime in the short-time period is close to the lifetime of the central area. This can be explained by studying the carrier amount

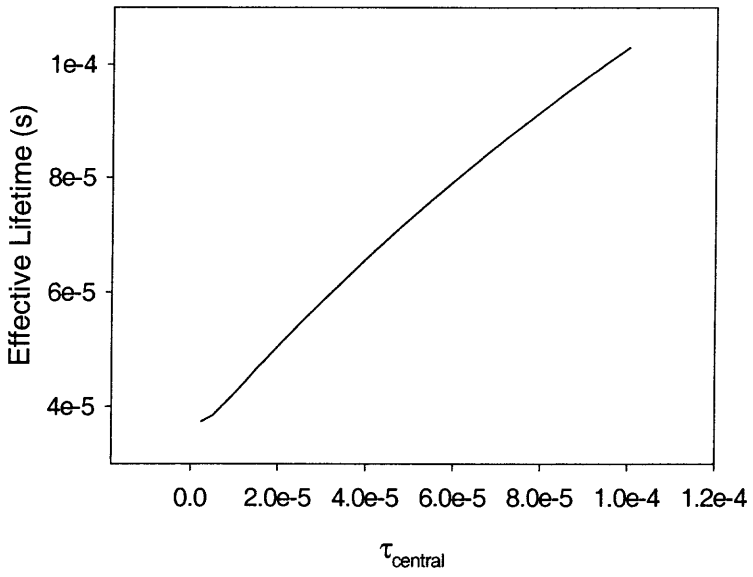

Figure 4.12. The calculated effective lifetime as function of $\tau_{central}$ in 3-region sample.

changing as a function of time in different regions inside the sample. Figure 4.13 shows the normalized total number of carriers $N(t)/N_0$, where $N(t)$ is the total carrier number inside the central or side regions at time t, as function of time . It can be seen that, in short time period, the total carrier number inside two side regions hardly changes from the initial amount, but the carrier amount inside the central region will decrease by almost 10% in just 10^{-8} s. Therefore, the reduction in the total amount of carriers in the whole sample is mainly caused by the reduction of carriers inside the central area, which follows function $N_0\exp(-t/\tau_{central})$. However, the decay time constant is not exactly equal to the $\tau_{central}$ because the carrier lost in the side regions also has some effect on the decay of total carrier amount in the entire sample.

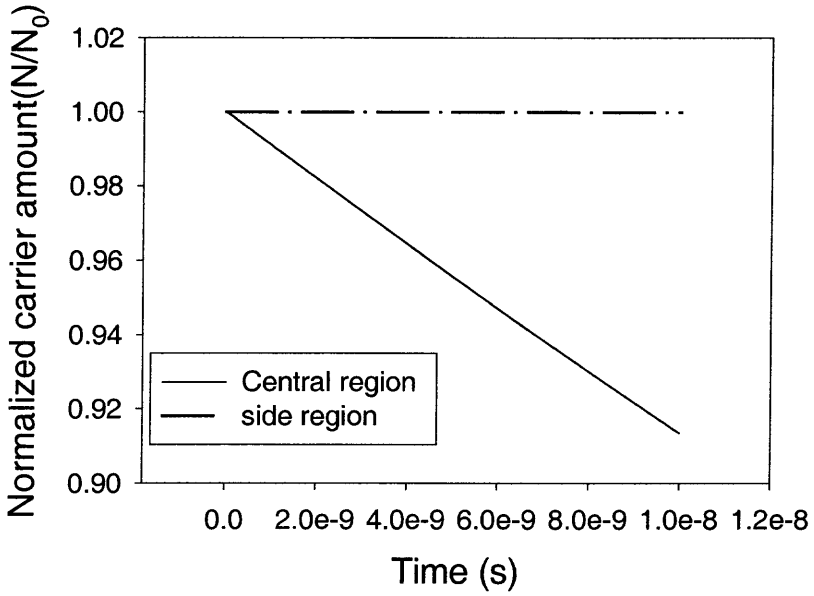

Figure 4.13 .The time decay curve of normalized carrier amounts in central and side regions of the three-region sample.

For the decay happening over the long time period, some unusual results show up. Figure 4.14 shows the fitted effective lifetime as a function of the ratio of the lifetimes in central to that in side region with changes in the area of the central region. Contrast to the intuition, the effective lifetime of the carriers will not decrease monotonically when the lifetime of the central area decreases.

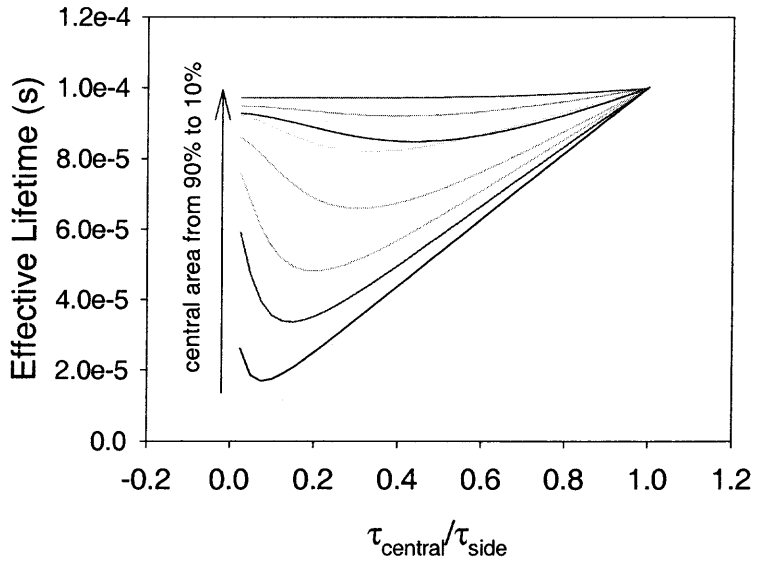

Figure 4.14. The calculated effective lifetime as a function of $\tau_{central}$ / τ_{side} and the area ratio of central region to the whole sample.

Two events occur when the carriers in the sample start to decay after the light is turned off: the carrier recombination in the three different regions (including the recombination at the surface) and the exchange of carriers between the regions. At different time period, these events will play different roles in the decay of the amount of carriers. We have seen that right after the light is shut off, the decay is mainly decided by the carrier recombination in the central region, which has shorter lifetime. But with the elapse of time, the carrier recombination in the side regions and the carrier flow start to become more important in the decay of the total amount of carriers.

If the carrier lifetime in the central region is very short compared with that in the side regions, the amount of carriers in short-lifetime region will be too small to be counted in the total carrier number in long time period. In this case, the carrier decay in the whole sample mainly depends on the "real" lifetime of the side area and the quantity of carriers flowing to the central region. Since the real carrier lifetime in the side regions will not change during the decay, the variation of the effective lifetime in this condition will be caused by the changing of the carrier flows between two regions — the smaller the flows are, the longer is the effective lifetime. To explain the results in Figure 4.14, the carrier flow from the side region to central region as a function of time and the lifetime of side area is calculated. The sample structure considered is the same as that shown in Figure 4.10. The results are shown in Figure 4.15. There is a peak that occurs close to the center of the domain considered. This indicates that the carrier flow between the two

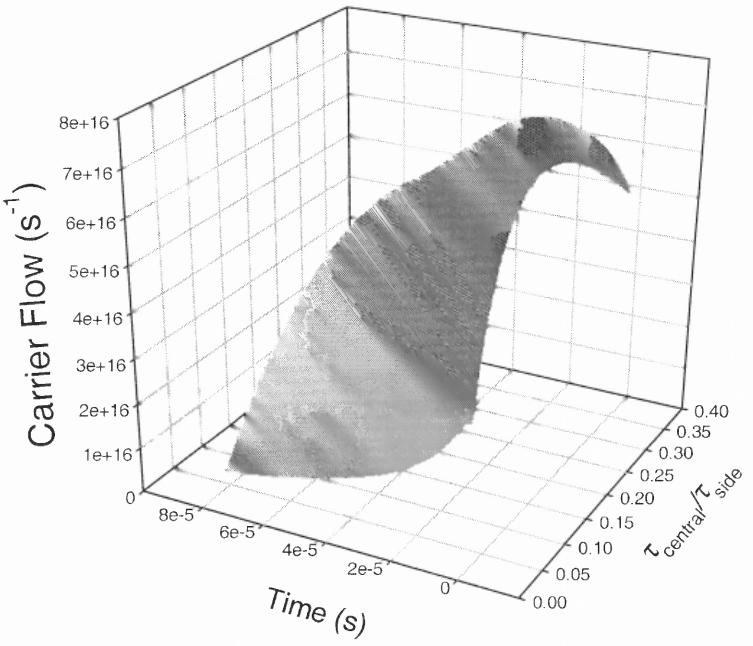

Figure 4.15. The carrier flow from side region to central region as functions of time and $\tau_{central} / \tau_{side}$.

regions will not change monotonically as the carrier lifetime and time change. When the time exceeds some value, the carrier flow will become smaller for reduced carrier lifetime. This explains why the effective lifetime will not always decrease when the lifetime of the central region decreases.

Several important conclusions can be drawn from the above analysis:

1. When two regions with different lifetimes exist in the sample and if the difference between the two lifetimes is large, the decay of the carriers in the whole sample will have two different effective lifetimes in the short-lifetime and long-lifetime period.
2. The decay in the short time period is mainly decided by the lifetime of the short-lifetime region.
3. The decay in the long time period depends on the carrier decay in the long lifetime region and the exchange between two regions mentioned before. The uncertainty of the carrier flows between different regions will make this value unpredictable and even meaningless.
4. The large-area carrier effective lifetime will not provide information on the lifetime of regions with very short lifetimes in non-uniform materials.

Influence of Non uniformity:

The sample considered here has ten grains. Five of these ten grains have longer lifetime τ_0 (=10^{-4}s) and the others have lifetime of $b*\tau_0$ (Figure 4.16), where b changes from 0.05 to 0.4. The calculated effective lifetime as a function of coefficient b is shown in Figure 4.17. As expected, the effective lifetime will become shorter as the factor b becomes larger, and the relation between them is almost linear.

τ	b*τ	τ	b*τ	τ	b*τ	τ	b*τ	τ	b*τ

Figure 4.16. A ten-grain sample considered in calculation.

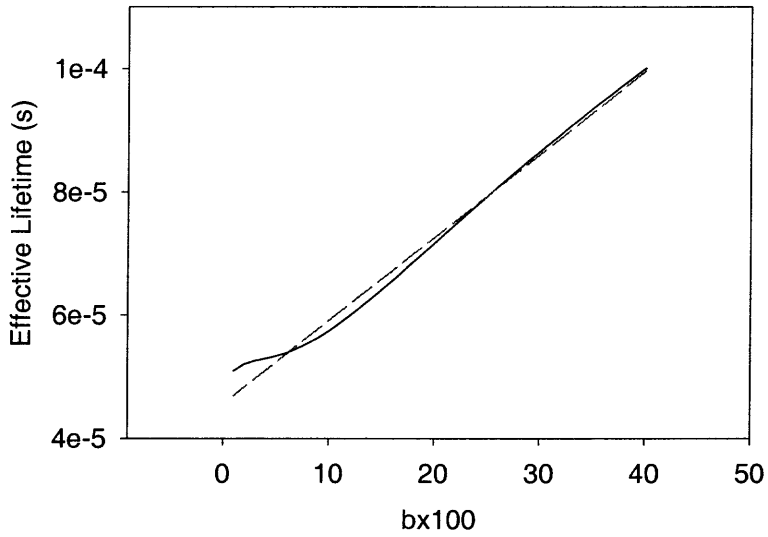

Figure 4.17. Calculated effective lifetime as a function of coefficient b in Figure 4.16 (solid line). The dashed line is a linear fitting of the calculated results.

Influence of defect distribution

Another interesting case is to see the influence of defect distribution pattern on the effective lifetime of materials. It has been known that in most PV materials, the defects exist in the sample as defect clusters. The primary concern here is the difference between the effective lifetime of a material with uniform defect distribution and a material with defect clusters.

The samples considered here are shown in Figure 4.16 and Figure 4.10. In one sample, 5 defect regions whose lifetime is $b*\tau_0$, are uniformly distributed in a 10-region sample similar to that considered in the previous example. In another sample, the short-lifetime region, whose lifetime is also $b*\tau_0$ (τ_0 is the lifetime in side regions), is concentrated in

the central part of the sample. The total area of the short-lifetime region is same in both cases.

The calculated results are shown in Figure 4.18. From this figure, we see that the effective lifetime is longer if all the short-lifetime regions are concentrated in one place. This is because the total carrier amount flowing from the long-lifetime regions to the short-lifetime regions is smaller in this configuration. Thus more carriers will stay in long-lifetime regions.

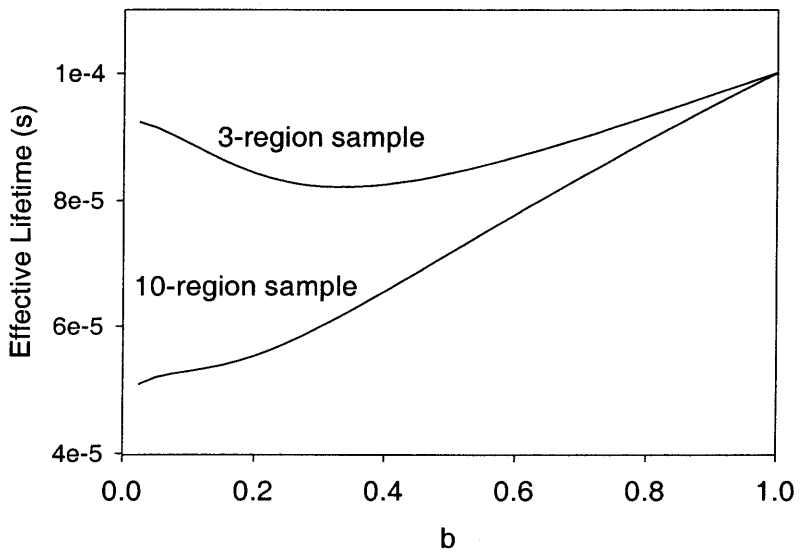

Figure 4.18. A comparison of the calculate effective lifetime as function of b in a 3-region sample shown in Figure 4.10 and a 10-region sample shown in Figure 4.16.

Scanning of the light beam

The previous analysis has shown that if the incident light is illuminating the entire surface of the sample, the effective lifetime calculated from the decay of the total amount of carriers will not reflect the localized properties of non-uniform materials. Suppose we want to measure the distribution of the lifetime over a large-area which consists of many different regions. Then, in order to get the localized lifetime in a uniform region in the sample, we can measure the carrier decay in this region. However, measuring the total

carrier amount in a small part of the sample is difficult, especially if this area is very small. An alternative way to carry out the measurement is to use a small light beam to scan over the sample and then measure the total amount of carriers and its time-decay curve, as shown in Figure 4.19. The light beam is directed at one spot on the sample till the carrier distribution reaches the steady state; then the light is turned off; the time decay of the total number of the carriers in the whole sample is measured. The light beam will then move to the next spot to repeat the same procedure. Here, we will check the feasibility of this light beam scanning method.

Figure 4.20a shows the carrier effective lifetime as the light beam moves through the surface of the sample. This methodology is illustrated in Figure 4.19. The three grains are of same size; the lifetime in the central region is 10^{-6}s, and in the other two regions, it is 10^{-4}s. The sample considered here has zero surface recombination. From Figure 4.20a,

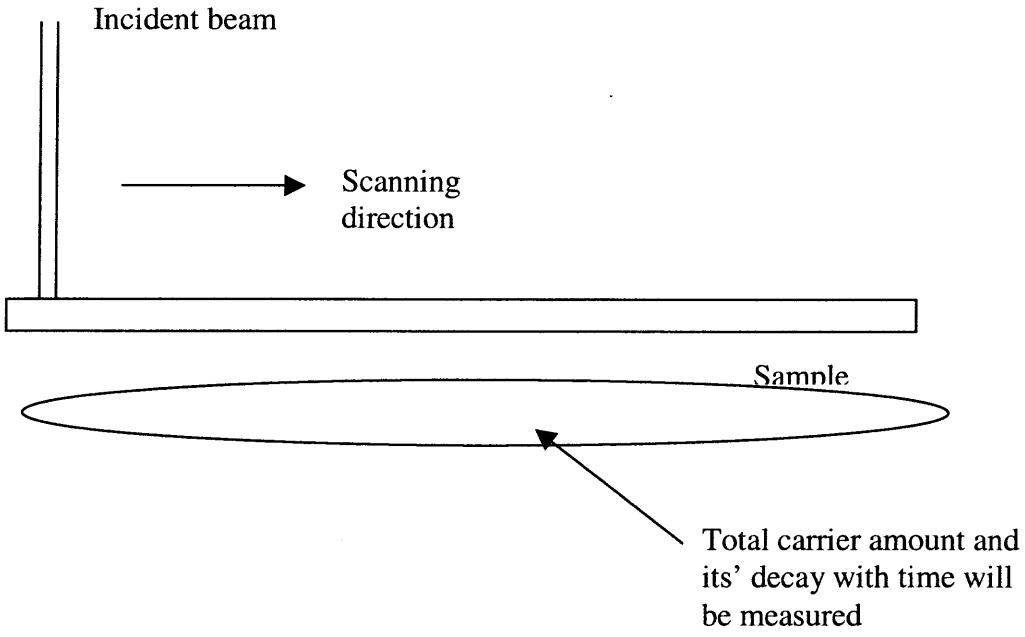

Figure 4.19. A schematic showing the beam-scanning method proposed in the text.

we can see that if the light beam is small enough, this method can yield precise information on the carrier lifetime of the beam incident area. Therefore, if the equipment that can measure the carrier decay is available, this scanning method can give precise information of the lifetime distribution of a large area sample.

Figure 4.20b shows the change of N_0 when the beam is illuminating the different spots on the sample. It can be seen that the N_0 measured this way has explicit relations with the "real" lifetime of different regions. The N_0 measured, when the beam is incident on the side regions, is exactly 100 times of the measured N_0 when the beam is incident on the central region.

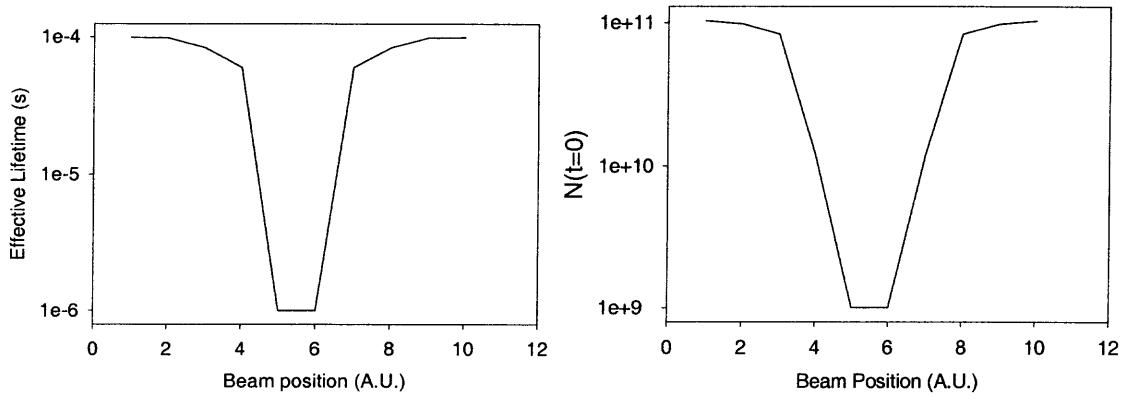

Figure 4.20. The calculated effective lifetime (left) and N_0 (right) as a function of beam position when the beam scanning over a 3-region sample. The beam size is 1 unit in the figure.

Summary: lifetime of minority carriers in multi-region Si

From the previous analysis, the following conclusions on the minority carrier lifetime in PV semiconductor materials can be reached:

1. The effective lifetime of the nonuniform materials is a very ambiguous concept. It not only depends on the exact lifetime in uniform region of the materials, but also

depends on the geometry of the sample, the surface conditions and the measurement methods.

2. In non-uniform materials, the effective lifetime over a large area relies on both the real lifetime in different regions and the amount of the carrier exchanged between these regions.
3. The scanning light beam / total carrier decay measurement method could be a precise tool to determine the "real" lifetime distribution in non-uniform materials. Both scanning SPV and scanning PCD are good candidates for this purpose.
4. The SPV measurement technique strongly depends on both the surface recombination and the absorption coefficient of the samples. The result of PCD measurement is influenced only by surface recombination.

4.5 Effects of defects on the p-n junction

To investigate the effects of the defects on the solar cells, it is natural to start with the investigation of the influence of defects on p-n junctions, which is the "engine" of semiconductor solar cells. Although most of the solar cells modeling softwares available commercially use sophisticated method to solve coupled continuity / Poisson equations in order to get the I-V characteristics of the device[80], in this thesis, we will use the depletion approximation of the p-n junctions. This model can help us to explore device physics though at a tolerable expense of numerical accuracy.

In section 4.4, we have categorized different regions in the material into four types. The carrier behavior inside these different regions in the materials was also studied. When a p-n junction is fabricated using these materials, all the equations, including boundary

conditions, still apply in the quasi-neutral region (QNR) of the p-n junction. However, the depletion regions(or space charge regions(SCR)) in different types of material need to be treated differently:

SCR inside type I regions should have the same behavior as the SCR in normal p-n junctions. In type II or type III regions, since there are extra charges (other than the dopant ions) and they are opposite to the charges of dopant ions, the net total charge should be less than that in the region without extra charges. The most apparent effect of the charges trapped in the p-n junctions may be the change of the width of the depletion region. This change can be easily determined by Schockley model:

$$w_{d.r.} = \sqrt{\frac{2\varepsilon_{si}(N_A + N_D - 2N_x)(V_{bi} - V)}{e(N_A - N_x)(N_D - N_x)}} \tag{4.10}$$

Where, Nx is the extra charge density trapped in the Si. This value is the same in n-type and p-type region because we assume that the amount of defect energy levels is the same in these two regions. In this program, we leave this variable as an adjustable parameter. The recombination current inside the space charge region due to type IV region can be written as (again, following the algorithm of Fossum and Lindholm[47]):

$$J \approx \frac{1}{4}\frac{w}{\sqrt{\tau_p \tau_n}} n_i \exp(\frac{qV}{nkT}), \tag{4.11}$$

Where, w is the width of the defectr rich region, and n_i is the intrinsic carrier concentration.

4.6 Modeling of the defects in Solar Cells

4.6.1 The model

The model used for device analysis is the combination of the models discussed in the last two sections, as summarized in Figure 4.21. The 2-D multi-region samples have the same configurations as those investigated in section 4 (see Figure 4.5), except that a p-n junction is presented. The doping profiles are also assumed to be the same in every region in the material although the depletion region formed may vary in different regions.

For simplicity, the metal contacts are considered as surfaces that have finite surface recombination velocities[81]. The top contact is assumed to be transparent so that the complex boundary conditions caused by the metal fingers / bus bars can be avoided.

Since we are only considering the double side polished samples here, the optical modeling is fairly simple; the exponential decay profile of the generation will be adopted.

The calculation of I-V characteristics of the device follows the normal depletion-region approximation model. The continuity equation is solved first to get the minority carrier distribution in the p-type and n-type quasi-neutral regions respectively. Then the current density generated in these regions is calculated from the carrier flow at the boundary of depletion region. The recombination / generation current density inside the depletion region is treated using the model developed in the last section; this current density is added to the current density generated in quasi-neutral regions. The integration of the current density over the surface of the device gives the total current generated by the device.

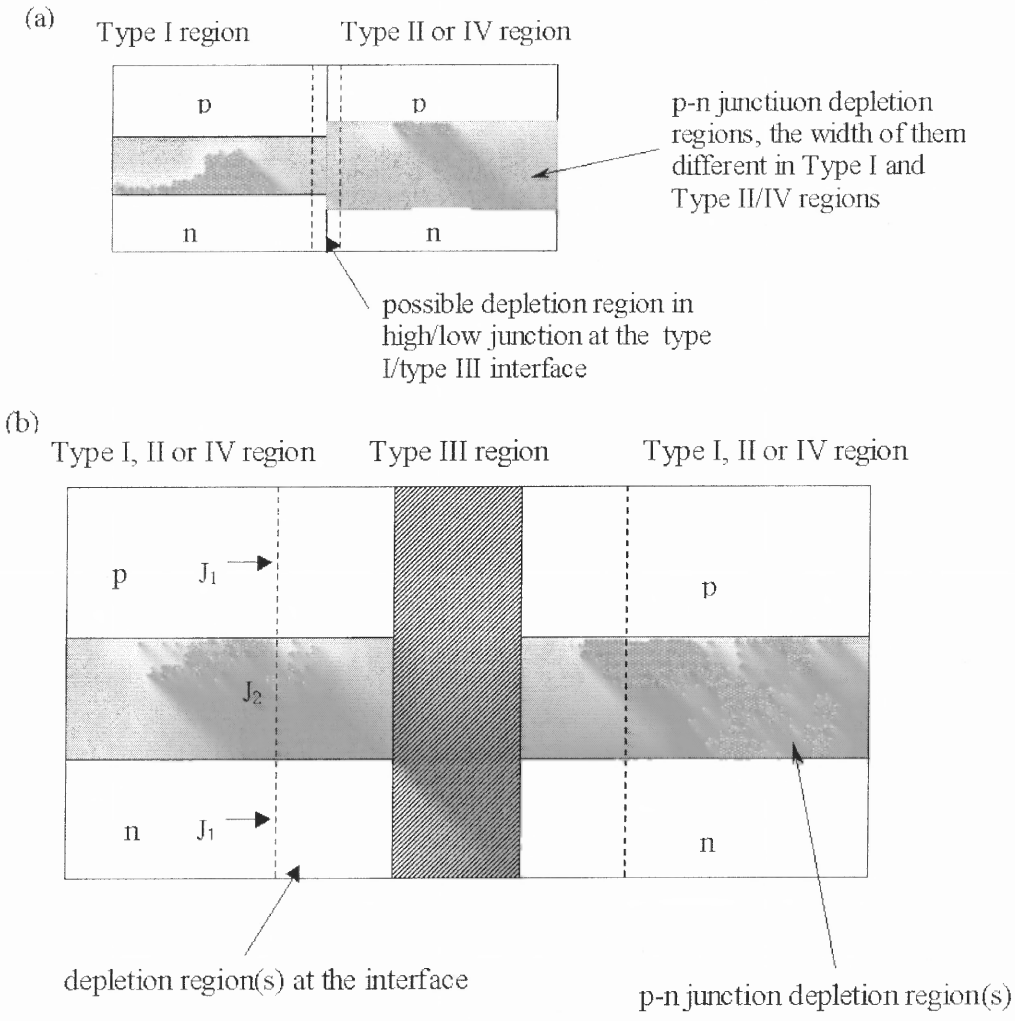

Figure 4.21. The proposed model of different regions in p-n junction built on non-perfect materials. (a) the model of Type I, II, IV region and relation between them inside a device. (b) the junction at the interface of Type I, II, IV region and Type III region. J_1 and J_2 and given by equation (4.8) and (4.11) respectively. The distribution of carriers inside type III region is not considered.

4.6.2 Programming

The finite element method is used to solve the continuity equations. The basic components of the finite element model are similar to those used in section 4.4. But, since the objects involved are different now, the interface of the software looks different

from that of the lifetime modeling program – a property page is added for user to input the parameters of p-n junctions.

4.6.3 Results and discussion

In this sub-section, some typical cases in the design of thin film μc-Si solar cells will be considered to verify the influence of defects on the properties of the solar cells. Since the current software is not able to calculate the optical properties of the device, the generation rate is a parameter input by the user; the Jsc calculated here is not comparable to the real device characteristics.

The influence of minority carrier lifetime on the solar cells

In this case, we consider the relation between the cell performance and the minority carrier lifetime of the materials. Here, only single crystal uniform materials will be investigated. The parameters used in calculation are shown in Table 4.1 (all parameters are defined in equation (4.2)).

Table 4.1. The parameters used in first set of calculation

G (s^{-1})	α (cm^{-1})	D (cm.s)	S (cm/s)	p-doping	n-doping
4.3963e+017	751.8062	50	0	10^{17}	10^{16}

Figure 4.22 compares the I-V characteristics of a 10 microns thick cell with minority carrier lifetime of 10^{-4}s and 10^{-6}s respectively. It can be seen that the Jsc for these two configurations are almost the same. This is because, for thin film, the amount of carriers collected by the cell will not change as long as the diffusion length of the minority carriers is greater than the junction depth. On the other hand, the Voc will drop more

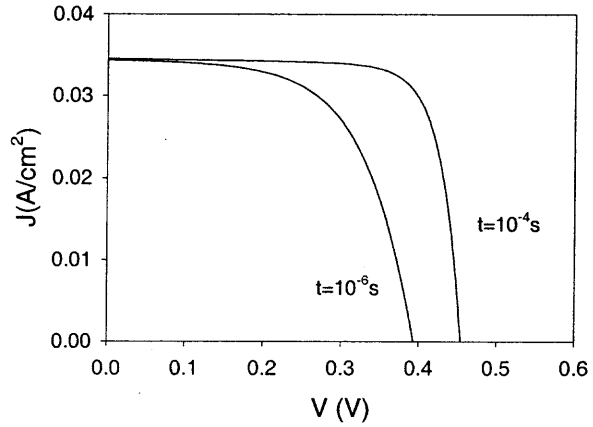

Figure 4.22. The I-V characteristics for different lifetime. The sample thickness is 10 μm.

when the lifetime becomes shorter; this is because Voc is mainly decided by the recombination inside the depletion region. This recombination strongly depends on the lifetime of minority carriers.

However, the situation will be different for thick cells. Figure 4.23 shows the I-V characteristic of two cells that also have lifetime of 10^{-4}s and 10^{-6}s respectively but the cell thickness here is 200 μm. It can be seen that both Jsc and Voc will drop drastically when the lifetime decreases.

From this analysis, we can conclude that thin film cells have better tolerance for low-quality materials. This is also an advantage of using thin film structures.

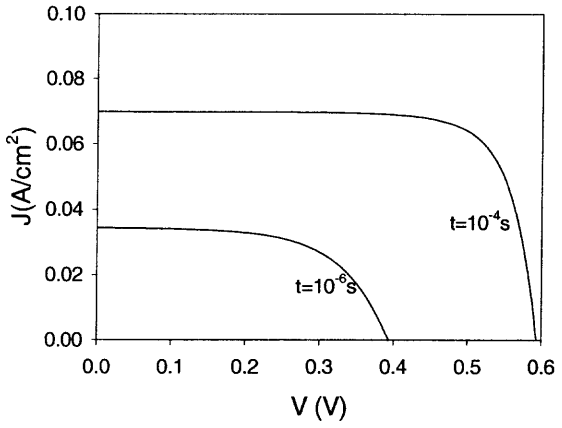

Figure 4.23. The I-V characteristics for different lifetime when the sample thickness is 200 μm.

The grain size of a μc-Si solar cell

One of the characteristic parameters of multi-crystalline Si is its grain size. In this example, we will investigate the influence of the grain size on the performance of the solar cells fabricated using μc-Si.

To limit the number of variables in this calculation, we assume that all the grains are the similar to each other. This assumption also brings other benefits to the calculation – since all the grains are similar, no net carrier flow will exist between grains at steady state. Therefore, the current collected by the device is just the summation of the current collected by each grain in the sample. The calculation time can be greatly reduced. The parameters used in this calculation are shown in Table 4.2.

Table 4.2. The parameters used in second set of calculations

G (s^{-1})	α (cm^{-1})	D (cm.s)	Junction depth	p-doping	n-doping
1e+018	100	50	0.5 μm	10^{18}	10^{17}

Figure 4.24 shows the calculated I-V characteristics of micro-crystalline (μc)-Si thin film solar cells with different grain sizes, where the interface recombination velocity is 100cm/s. From this figure, it can be seen that the larger the grain size, the better the performance of the device. Furthermore, when the grain size is larger than 1 μm, the decreasing of the grain size will cause the degrading of the Voc but the Jsc will not change too much. When the grain size is too small (<0.5μm), the Isc will also start to drop quickly as the grain size becomes smaller.

Detailed results on the change of Jsc and Voc are shown in Figure 4.25. It can be concluded that, to get device with satisfactory Jsc and Voc, the grain size of μc-Si thin film solar cell should be several microns.

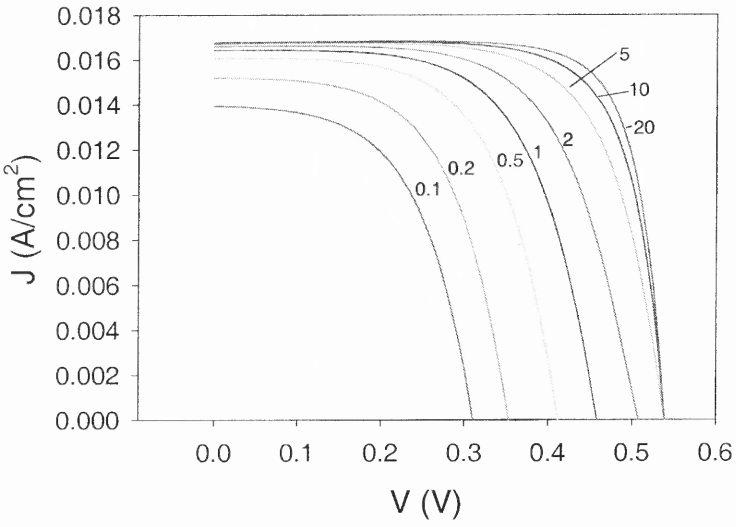

Figure 4.24. The calculated I-V characteristics foe different grain sizes of a 10-μm-thick cell. S=100. The number represents the grain size (in μm) corresponding to the curve at the lower-left side of the number

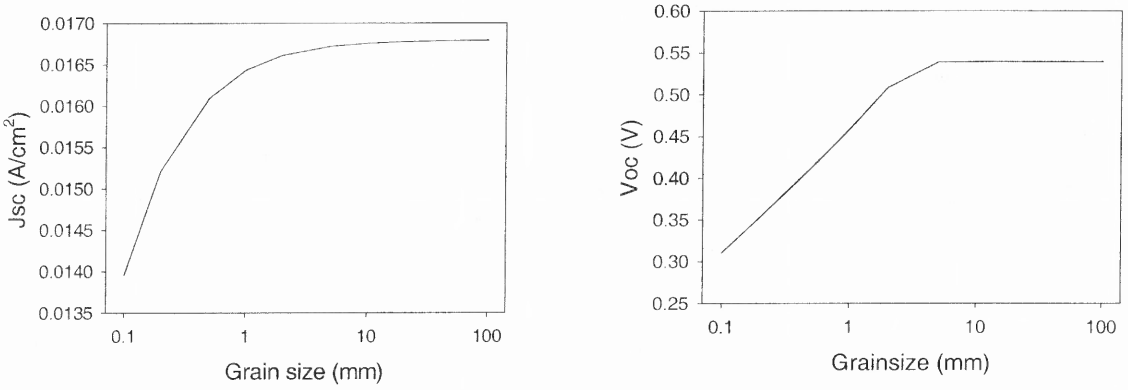

Figure 4.25. Calculated Jsc, Voc as functions of grain size of the cell considered in Figure 4.24.

The influence of grain boundaries

In this case, we will discuss the influence of the interface recombination on the performance of the cells. In Figure 4.26, I-V results of samples with different grain sizes are presented. This figure is similar to Figure 4.24, but in this case, the interface recombination velocity is 1000cm/s.

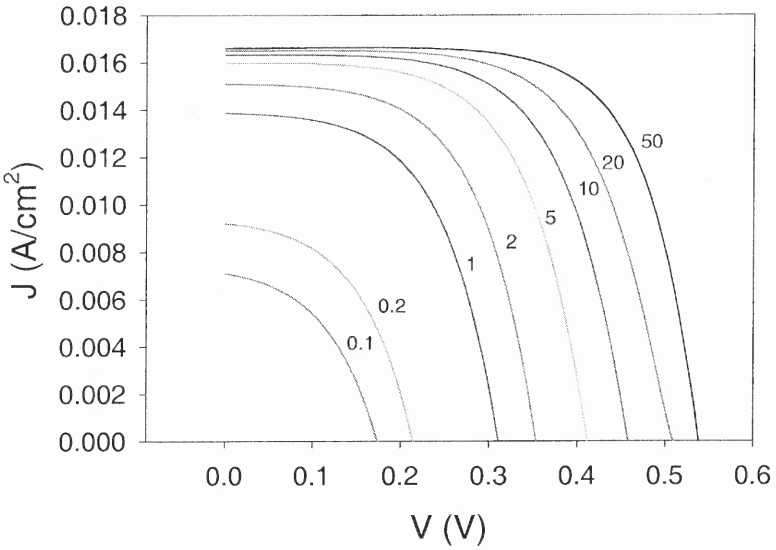

Figure 4.26. The calculated I-V characteristics for the same cell considered in Figure 4.24. But the interface recombination velocity here is 1000 cm/s. The number represents the grain size (in μm) corresponding to the curve at the lower-left side of the number

From this figure, we can see that the surface recombination has very strong influence on the device performance especially when the grain size is small. Therefore, the passiviation of the grain boundaries is very important for μc-Si thin film solar cells.

Detailed results on the influence of the grain boundary recombination are shown in Figure 4.27. Figure 4.27a is for a 5-μm-grain-size sample, and Figure 4.27b is for a 0.5-

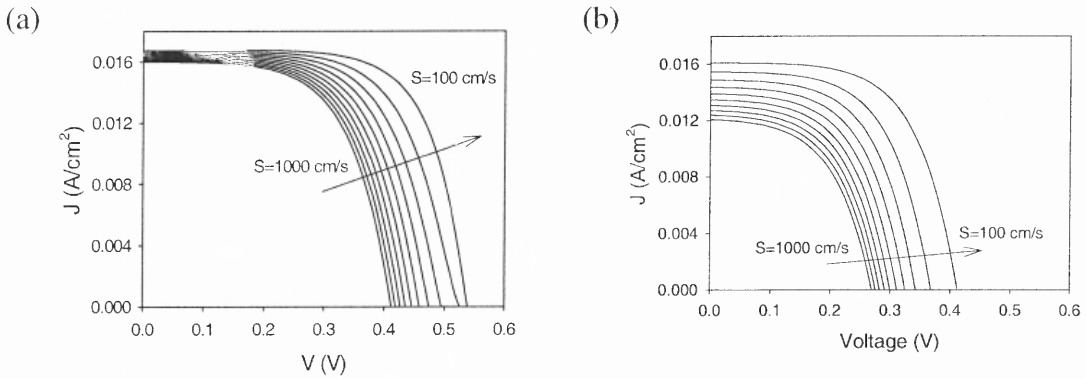

Figure 4.27. The calculated I-V charaters for different grain boundaries SRVs. In the figures, S changes from 1000cm/s to 100cm/s in different curves. The grainsize considered is (a) 5 μm, (b) 0.5 μm.

μm-grain-size sample. It can be seen that, for larger grain size, the recombination at the grain boundaries will mainly degrade Voc, but Jsc will not decrease too much by increasing surface recombination velocity (SRV) at the grain boundaries. But when the grain size is reduced, Jsc will also drop fast as the SRV increases.

Influence of defect distribution

In this case, we consider the influence of the defect distribution on the I-V characteristics. Two sample configurations will be investigated here. In one sample, the short-lifetime region is concentrated at the center of the sample (as shown in Figure 4.10), while in the other sample, the same area of short-lifetime region is distributed uniformly in every alternate region in a 10-region sample, as shown in Figure 4.16.

Figure 4.28 shows the calculated I-V characteristics of these two samples. From this figure, we can see that the performance will be better when the defects are confined to one region in the cells.

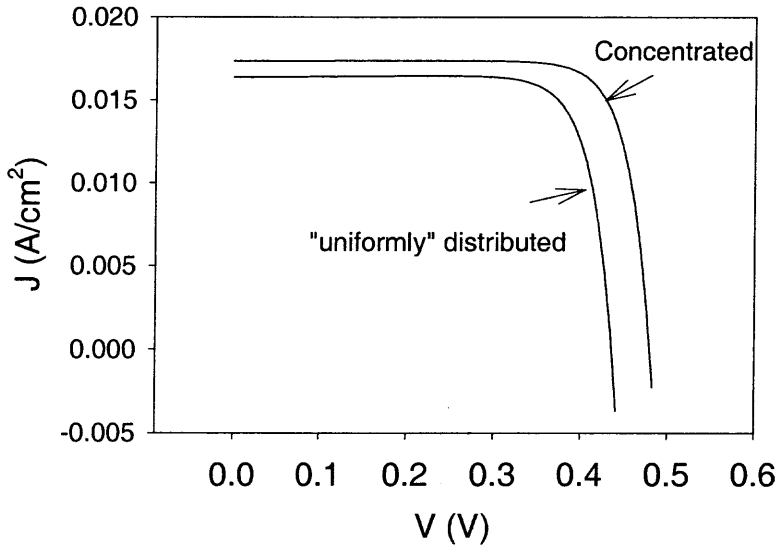

Figure 4.28. Comparison of calculated I-V character of two samples. In one sample, the short-lifetime area is concentrated at the center of the sample. In another sample, this area is divided into 5 regions and uniformly distributed in a 10-region sample

The uniformity of generation

The light trapping techniques can generate a non-uniform photon distribution inside the semiconductor layer. Therefore, the photon-generated carrier density distribution will also be non-uniform. The influence of this kind of non-uniformity on the device performance will be studied in this example.

Figure 4.29 shows the calculated I-V characteristics of two different samples. In one sample, the minority carriers are uniformly generated in the entire sample while in the other one, the same amount of carriers are generated in only the central part of the sample. From Figure 4.29, it can be seen that the I-V characteristics of these two samples *are* different – the Jsc and Voc of the "concentrated generation" sample are smaller than those of "uniform generation" sample. This result implies that during the optical design of the solar cells, the generation distribution (so the light intensity distribution) inside the cells should also be considered.

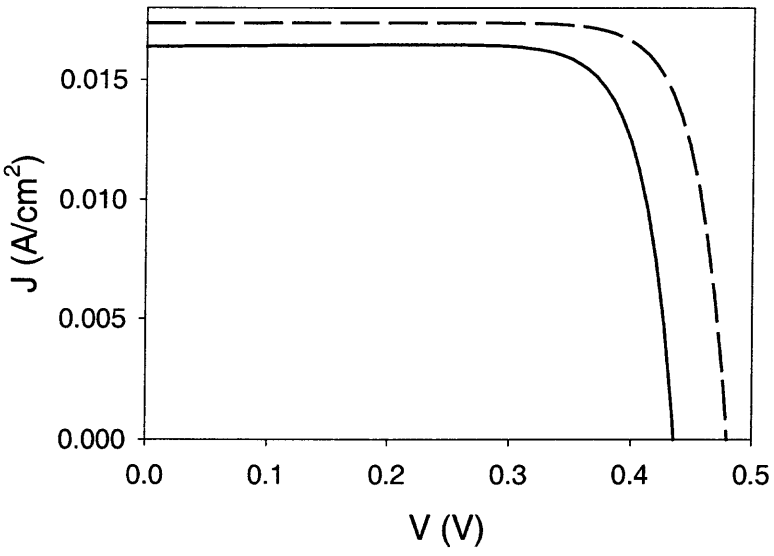

Figure 4.29. The calculated I-V characteristics by different generating distribution. In one sample (represented by dashed curve), the generation is uniformly distributed inside the sample. In the other one (solid line), the same amount of generation is concentrated in only central region

4.7 Summary – The least-acceptable material quality of our cells

From the analysis in this chapter, the following conclusions on the electrical design of the cell structure proposed in chapter 1 can be reached:

1) The thin film μc-Si should have a grain size larger than 1μm, 10μm grain size is desirable.
2) In each grain, the defects should be such that the minority lifetime would be larger than 10^{-6}s to get acceptable Voc, although Jsc will not drop substantially as the lifetime becomes even shorter.
3) At the grain boundaries, the recombination velocity should be less than 1000 cm/s; it will be ideal if S<100cm/s.
4) The defect area should be limited to one region instead of being distributed in the sample.

CHAPTER 5

FABRICATION OF μc-Si FILM SOLAR CELLS

5.1 Introduction

The previous chapters have described the design considerations and the technical requirements of NREL thin-film Si solar cell. The major processing steps required to build such a cell are: 1) deposition of a-Si film with a subsequent conversion into large-grain (grain size > film thickness) μc-Si with back contact, 2) formation of p-n junction, and 3) formation of front contact. Among these steps, the most important (and the most difficult) is the crystallization of the Si thin film. The difficulties are due to the following requirements:

1. The grain size of μc-Si should be from several microns to 10 microns. To get the μc-Si thin film with this grain size, the conventional crystallization methods, which imply the use of thermal annealing, require temperatures higher than 500°C and/or very long processing time. However, since our objective is to use low-cost glass as a substrate, such high temperatures are not compatible with the properties of the glass that has a softening point of about 550 °C. Hence, a new method to crystallize Si thin film at low temperature and short time needs to be developed.
2. As pointed out in the previous chapter, the defect density inside the thin film should be as low as possible to get acceptable devices. It is therefore important to consider the method to prepare a film that has low defect density at fairly low cost.

The proposed approach to reduce the crystallization temperature is to invoke semiconductor-metal reactions. These reactions have drawn a lot of attention in recent

years. The most attractive result of these reactions is that certain metals can bring about crystallization of the a-Si film (so called metal induced crystallization (MIC)) at much lower temperatures than that required by simple thermal annealing. Consequently, MIC can potentially be employed for making cost-efficient thin film micro-crystalline Si. The literature contains several references to MIC, but the experimental results vary greatly. It has been shown that MIC can start at temperatures as low as 150°C[82]. Different grain sizes, from several tenths of microns to several microns have been reported. However, most of the studies conducted so far are concentrated on MIC of sub-micron-thick Si films. In some cases, the processed samples have high concentrations of Al in Si. Very little information is available in the literature that deals with the effects of metal on relatively thick (several microns) Si film samples (in which the amount of Al is much less than that of Si). The applications of this technique on device fabrication are also rarely found.

In our study, we will attempt to explore the answers to the following questions:

1. Can we apply Al induced crystallization on the sample that has much less Al than Si? How can we improve processing to get large grains?
2. Would such a process be different from a typical thermal annealing? Are there any different mechanisms involved?
3. Can the Al level inside the Si be controlled so that one can form an alloyed back contact for a BSF and have an acceptable level of Al in the bulk of the film?

This chapter will be organized in the following way: we will review the published work on crystallization / grain enhancement of Si thin film; then discuss results of our experiments aimed at low-temperature crystallization and grain enhancement. The

mechanisms involved in the processing will be discussed. Then the results of the cells fabricated using the materials developed will be presented.

5.2 Overview of crystallization techniques

5.2.1 Direct Growth of Poly-Si thin films:

Here "direct growth" refers to the process in which the μc-Si thin films are deposited directly instead of carrying out the crystallization / grain enhancement procedure after the a-Si thin film is deposited. Chemical vapor deposition (CVD) is employed by most researchers for direct growth of thin μc-Si film. Although the films deposited by this method can be 100% crystallized, their grain size are too small (≤100Å). The thickness of the Si film on glass grown by this method cannot be too large because Si films thicker than 1μm will peel off due to stress.

Different techniques are used in direct-growth method to help enlarge the grain size of μc-Si. Bergmann etc.[83] reported a two-step CVD process to make the large grain poly-Si thin film on their specially-developed glass. In the first step, low-pressure CVD using disilane at temperature of 450 °C serves to deposit a-Si; this a-Si layer is then annealed at temperature around 600 °C for 10 hours. The poly-Si film thus obtained is used as the seed for a second epitaxial deposition using atmosphere pressure CVD from trichlorosiliane. Typically, the second layer can be several-micron-thick and is deposited at 1000 °C. The grain size is about several microns.

5.2.2 Grain Enhancement of a-Si thin films:

Annealing:

When an a-Si film deposited on substrate is subjected to a thermal anneal for an extended period of time, crystallization ensues and grain size of the film increases with time and temperature. Because this process does not require melting of the Si, it is called solid phase crystallization. The grain enhancement in this process results from a movement of grain boundaries activated by the heating. An increase in the time or temperature or both can further promote the grain growth. The major drawback of thermal annealing process is that it requires long processing time or high temperature (>1000°C). A typical annealing process will take 20-40 hours[84]. Different kinds of technologies, including using surface-textured substrate, doped a-Si layers etc., are used in the annealing process to reduce the processing time and processing temperature. These technologies accelerate the velocity of grain enhancement either by introducing seeds or activating the grain boundary movement using impurities.

Metal-Induced Crystallization (MIC):

One of the ways to convert a-Si to poly-Si is by metal induced crystallization. A metal layer is deposited on the film of a-Si, and the structure is annealed. The effects of several kinds of metals, such as Sb, Au, Al, Pd, Ti and Ni have been studied. The metal induced crystallization process sounds promising in the formation of thin film poly-Si on the glass substrates because of its low processing temperature and short processing time. However, there is a serious draw-back that will prevent its usage from the fabrication of TFT devices: the metal contamination of the Si layer induced by the intermix of metal and Si. For some kinds of metals, including Pd and Ni, this problem was reported to be solved by utilizing metal induced lateral crystallization (MILC)[85], where crystallization was shown

to extend into a metal free lateral area after the MIC. The grain size up to several microns was obtained. The performance of the final TFT devices was also acceptable.

Zone-Melting Recrystallization(ZMR):

In Zone-Melting Recrystallization, a narrow zone on the surface of the sample is melted with heating. The whole film is recrystallized with moving this melted zone around the surface. A range of energy sources, including strip heaters, electron beams and radio-frequency (RF) heaters has been used. Because the thin film is heated to the temperature around the melting point of Silicon (~ 1200 °C), this method is not suitable for the crystallization of the a-Si film on the normal glass substrate. For other kinds of low-cost substrates (like metallurgical Si, carbon etc.), it is also a challenge to prevent the impurity diffusion from substrates to the thin film.

Ishihara[86] et. al. reported impressive results of solar cells fabricated on the poly-Si thin film obtained by ZMR technology. They use a thin layer of SiO_2 on the Si substrate as a stopping layer for impurity diffusion. The sample was heated up to about 1200 °C by a line-shaped heat source of carbon strip just above the sample in vacuum. (100) dominated surface was obtained with a scanning speed at $0.2mm \cdot s^{-1}$, the grain size of millimeter to centimeter order was reached.

Laser-induced crystallization:

XeCl excimer laser recrystallization (ELR) and annealing (ELA) of a-Si has been studied extensively in recent years. Although most works are concentrated on the usage of this method in the thin film transistor (TFT), it is also used in solar cells.

In laser recrystallization, depending on the power of the incident light, the part of the thin film under illumination can be either in liquid phase (melted totally) or in liquid + solid

phase (partly melted). Although in ELR, the temperature in the thin film could be higher than the melting point of Si, the temperature of the substrate could be much lower because short-pulse laser is used in this process. This is a major difference between ZMR and ELR. By placing thin oxide layer and/or nitride layer between the substrate and a-Si, both the heat diffusion from the thin film to the substrate and the impurity diffusion from the substrate to the thin film can be dramatically reduced. Other alternatives to improve the quality of the film, such as using pre-patterned a-Si, multiple-steps laser processing etc., are also suggested. TFT fabricated using XeCl excimer laser recrystallization with excellent overall performance are reported.[87] At present, the solar cells formed by laser crystallized Si can achieve conversion efficiencies close to 9%.

Solid phase crystallization processing using excimer laser annealing (ELA) combined with rapid thermal processing (RTP) is also reported.[88] The ELA treatment can be at a temperature of 550 °C. μc-Si thin films with grain size up to several microns can be created. However, limited by the high cost of equipment, ELA method is not suitable for low cost thin film solar cell fabrication.

Some parameters of these methods are summarized in table 5.1.

Table 5.1. Comparison of different crystallization methods

Method	Processing Temp. (°C)	Processing Time	Metal Contamination
CVD growth	1000	> 10 hours	No
Annealing	500	20-40 hours	No
ZMR	1200	quick	No
MIC	<500	quick	Severe
LIC	>1000	quick	No

5.3 Experimental details

It is thus clear that the approaches described in last section are not suitable for low-cost thin film solar cell fabrication. In this section, we describe the application of optical processing for metal-induced crystallization and grain enhancement. The details of our experiments will be reviewed. These details include the equipment configurations, the sample structures and the characterization methods used in the experiments. Optical processing is used for the crystallization and grain enhancement steps of a-Si. Compared to traditional thermal processing, the temperature profile in optical processing is much more flexible. The processing time is also much shorter. Optical processing also provides other benefits because of optics-related effects involved in the processing.

In optical processing, a sample consisting of a-Si deposited on an Al/Cr coated glass substrate, is illuminated with light that is rich in the infrared (IR) content. The incident light is partly absorbed in the semiconductor and the metal layers resulting in thermal heating and a concomitant increase in the sample temperature. Some of the photons reaching the Si-Al interface can produce a number of effects. One of these effects (although not fully proven) is believed to be the introduction of point defects (vacancies) during such a process. Presence of the vacancies helps in a rapid grain growth. Thus, the proposed process involves nucleation that initiates at the Al-Si interface followed by growth of grains assisted by injection of vacancies.

5.3.1 Processing equipment configuration

Optical processing furnace (OPF) is used in optical processing. Figure 5.1 shows the operating principle of optical processing. The IR-rich light is incident on the thin film sample to carry out the anticipated reactions in the sample. The processing chamber is

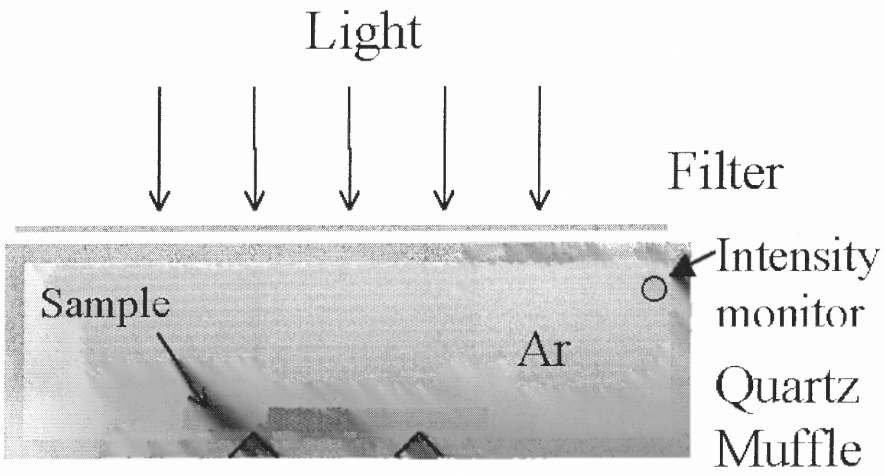

Figure 5.1. Operating principle of optical processing furnace.

filled with Argon during processing. A typical temperature-time profile is shown in Figure 5.2. Figure 5.3 shows the system configuration of the optical processing furnace. The user can adjust the input signal of the power-controlling unit through the computer, and thus control the light power profile. The temperature is monitored using an Omega DP41-TC temperature indicator; this indicator also sends temperature readings to the computer, which also monitors all the other important parameters in the system during processing. Normally, a process can have six time segments, so different processing recipe can be applied for different purpose. By finely tuned input parameters, the sample temperature fluctuation can be less than 5°C if the user wants to use constant temperature in some specific time segment.

A thermal process furnace is also used for thermal processing. This furnace uses the a resistor heating system. An Electromax® V plus general-purpose single-loop controller made by Leeds and Northrup instruments controls the temperature. The long time temperature fluctuation is less than 5° C.

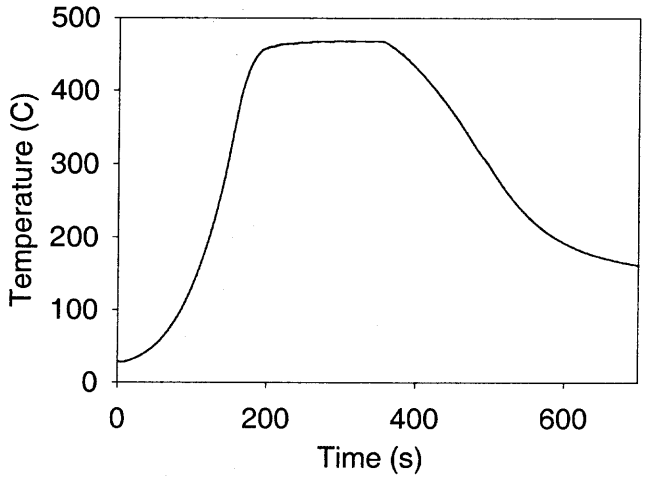

Figure 5.2. A typical temperature profile used in optical processing

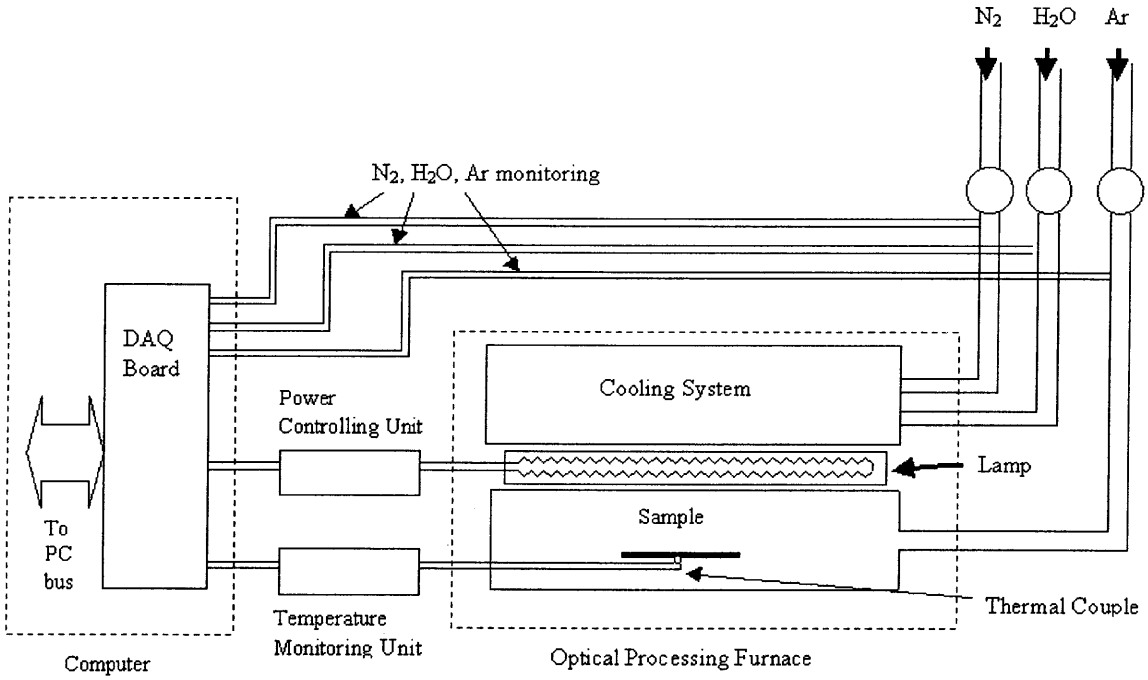

Figure 5.3. System configuration of optical processing furnace.

5.3.2 As-deposited sample structures

Various sample structures are used for different purposes in this project. Two kinds of substrates are used: quartz, and crystalline silicon. The thin films are grown using different methods: hot-wire CVD(HWCVD), plasma-enhanced CVD(PECVD). Both the HWCVD and PECVD systems are developed by MVsystem, Golden, Colorado. The thickness of the films range from 2 μm to 10 μm. The deposition temperatures of the samples are also different. The details of the deposition conditions and configurations of these samples are listed in Table 5.2. In this table, the samples are grouped according to their deposition conditions. In each group, every sample is labeled with a 2-digit number, such as 11, 12, 21, 22.

Table 5.2. The as-deposited sample structures

Sample group	Structure	Deposition method	Growing temp. (°C)
HW54	2μm μc-Si / 1μm Al / 100A Cr / Qtz	HWCVD	600
HW55	2μm μc-Si / 1μm Al / 100A Cr / Qtz	HWCVD	500
HW143-1	2μm a-Si / 1μm Al / c-Si	HWCVD	300
HW143-2	2μm a-Si / 1μm Al / 100A Cr / Qtz	HWCVD	300
HW161	10μm a-Si / 2 μm Al / 100A Cr /Qtz	HWCVD	<400
HW162	10μm a-Si / 2 μm Al / 100A Cr / Qtz	HWCVD	~500
HW163	10μm a-Si / 2 μm Al / c-Si	HWCVD	~500
HW164	6μm a-Si / 2 μm Al / 100A Cr / Qtz	HWCVD	<250
HW165	3μm a-Si / 2 μm Al / 100A Cr / Qtz	HWCVD	<100
PE1	3μm a-Si / 2 μm Al / 100A Cr / Qtz	PECVD	~190
PE2	6 μm a-Si / 2 μm Al /1μm Ag/ 100A Cr / Qtz	PECVD	~200

5.3.3 Processing procedures

The samples are processed at different conditions. Figure 5.2 shows the typical temperature time profiles during processing. The detailed processing profile of a specific sample will be described when that sample is discussed. Since not every sample is

attached with a thermocouple, the temperature profile is measured by a sample that has a thermocouple and processed at same input-light-power profile (this profile can be controlled by the user). Normally, a processing profile has one or two time period(s) during which the temperature is almost constant. In this chapter, a processing profile is identified by this constant temperature(s) and the length of the corresponding time period(s). To avoid the cracking or explosion of the samples caused by sudden temperature change, in most cases, the sample was heated up and cooled down at a fairly slow speed (< 80°C/min) instead of a normal RTP profile – but still much faster than that of regular thermal annealing process.

Thermal processing is also used for comparison. The thermal process profile is set as close as possible to that of optical processing for comparable results. To simulate the fast temperature increasing pattern in OPF, the sample was pushed into already-heated thermal furnace at proper speed instead of leaving the sample inside the furnace and heating the furnace subsequently. Unless otherwise stated, all the "processing" referred to in this chapter is optical processing.

5.3.4 Characterization of materials

XRD, SIMS, SEM, TEM, optical microscope optical spectrometer are used in the characterization of the samples. XRD is suitable for qualitatively studying the crystallization[89]. It can verify a) the starting of the crystallization (the presence of the peak), b) the change of grain size when the grainsize is smaller than 1 μm (the width of the peak), and c) the change of the texture of the film.

The SIMS profile was used to determine the Si and Al distribution inside the samples. The morphology and grain structure of the samples were observed by SEM, TEM and

optical microscope. On some samples, the reflectance was measured by a Cary V spectrometer.

5.3.5 Testing-Device formation and characterization

After processing, the as-deposited film on most samples is converted into p-type layer. A thin n-type μc-Si layer was deposited on the sample using PECVD method to form a p-n junction; then a TCO layer was deposited through a mask over the n-type layer. The mask is utilized to assist in the distribution of the TCO layer on the Si thin film with fixed pattern (Figure 5.4). This design enables us to separate the devices at different area, and evaluate their properties separately. An I-V measurement system based on Keithly 238 High Current Measurement Unit was used to measure the basic I-V characteristics of the devices. The standard I-V measurement was done using NREL's standard AM1.5 simulators.

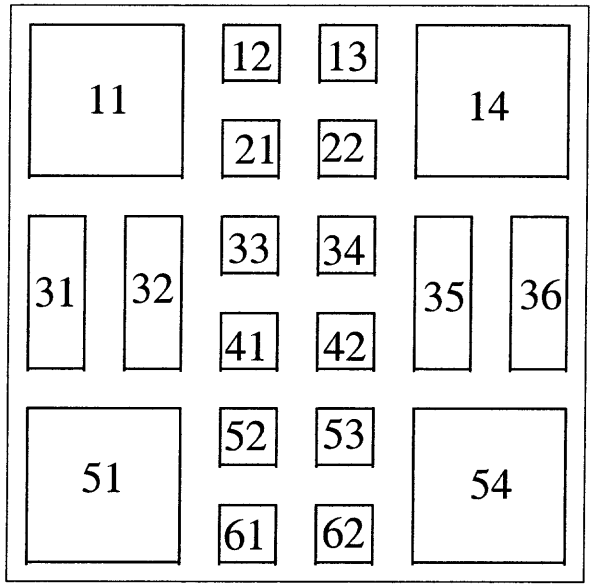

Figure 5.4. Schematic of the mask used for TCO layer deposition. The numbered areas are where the TCO was deposited. These numbers are used to identify the devices on the film.

5.4 Al-involved mc-Si fabrication at NREL

5.4.1 The properties of samples before processing

Because the a-Si depositions were carried out under different conditions, the as-deposited samples also have different degree of crystallization. These samples can be divided into three categories:

a) In the samples deposited at temperature less than 200°C and short deposition time, no crystallization happens during deposition. These samples include HW165-XX group and PE1-XX group. Figures 5.5 and 5.6 show the XRD spectra of two samples from

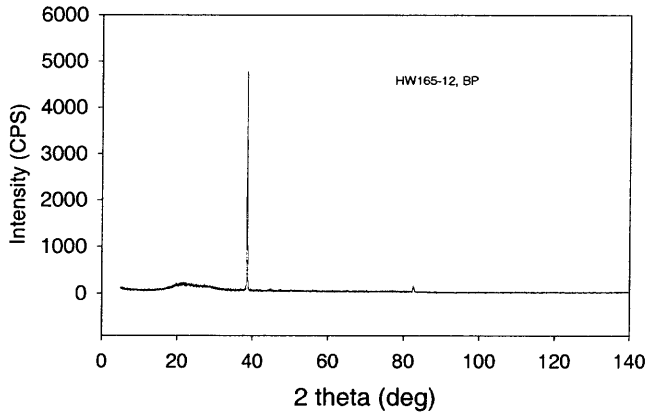

Figure 5.5. XRD spectrum of sample HW165-12, before processing, no structure from crystalline Si can be observed. Two visible peaks are from Al.

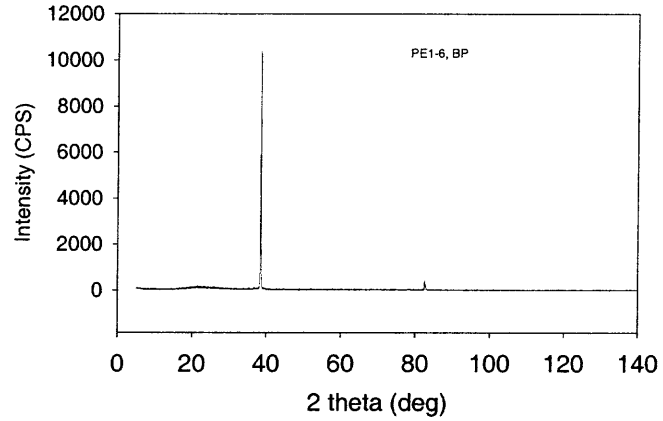

Figure 5.6. XRD spectrum of sample PE1-6, before processing, no structure from crystalline Si can be observed. Two visible peaks are from Al.

these two different groups. In these spectra, only the peaks from the Al can be observed; no diffraction peaks from Si show up.

b) For the samples deposited at temperatures less than 400°C (HW161 and HW164 group), very weak crystallization peak can be observed, as shown in Figures 5.7 and 5.8. This is because during the deposition, the relatively high temperature (~300C) and long time (>30 min) have already triggered the Al induced crystallization.

c) For the samples grown at temperatures around 500C (HW55-XX, HW162-XX

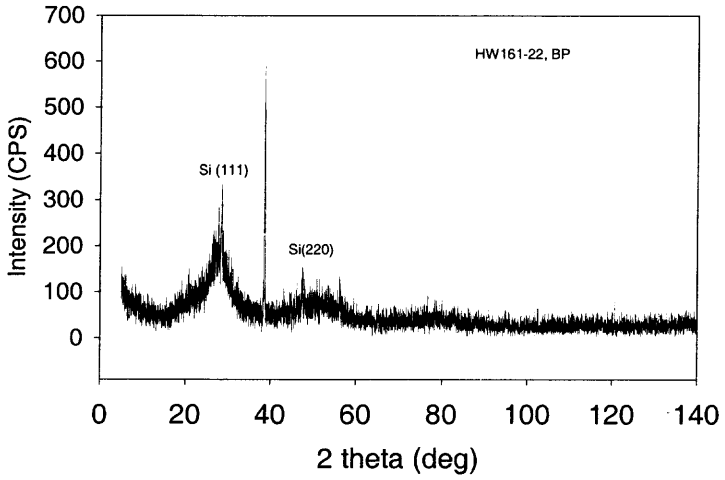

Figure 5.7. XRD spectrum of sample HW161-22, before processing, two peaks from Si can be observed.

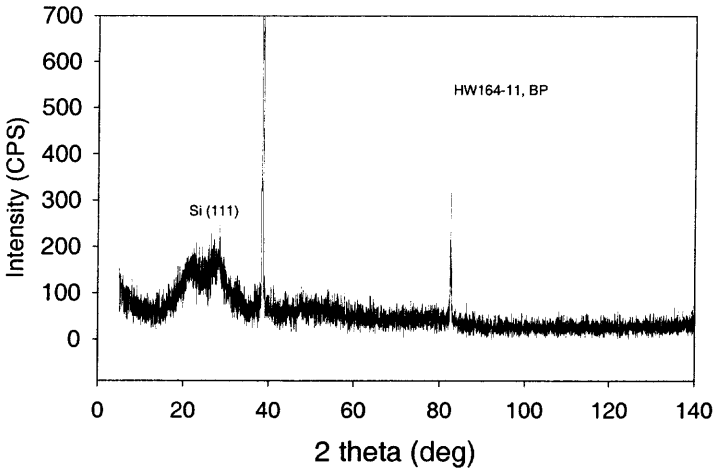

Figure 5.8. XRD spectrum of sample HW164-11, before processing, very weak Si (110) peak is visible in this spectrum.

groups), the XRD spectrum of one such sample is shown in Figure 5.9. Some peaks from Si (especially a strong Si <220> peak) can be seen in this spectrum. Since the relative intensities of these peaks do not follow the pattern of powder Si samples, the crystallinity of these as-grown samples is highly-textured.

d) For the samples grown at temperatures higher than 600C, strong peaks from Si can be observed in the spectrum (Figure 5.10 for sample hw54-xxx). The relative intensity of these peaks indicates that this sample is highly textured in Si <111> direction. On these samples, the Si is strongly crystallized. There is no apparent peak from Al in

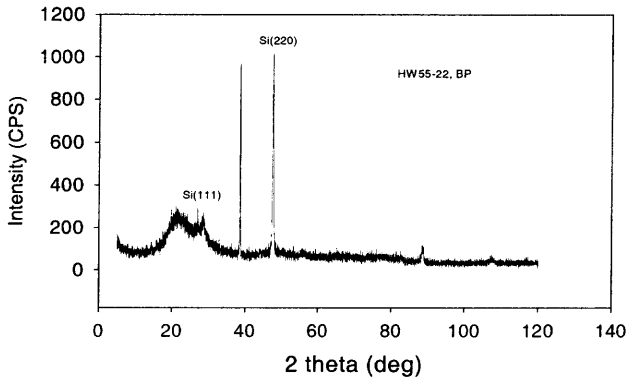

Figure 5.9. XRD spectrum of unprocessed sample HW55-22, a strong Si (220) peak can be observed in this spectrum.

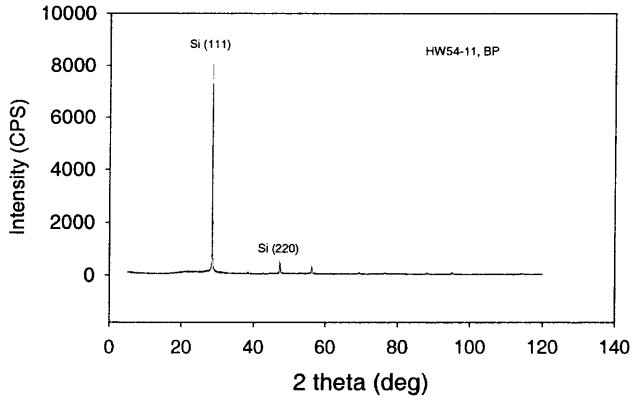

Figure 5.10. XRD spectrum of unprocessed sample HW54-11. This sample is already strongly crystallized before processing, and strongly textured in Si(111) direction.

this spectrum, which implies that the crystalline Al is consumed during the deposition. The films in this group of samples are just the mixtures of Si and Al.

5.4.2 The starting point of crystallization

To find out the lowest processing temperature at which the crystallization can happen, One non-crystallized as-deposited samples in HW165-xx group are processed at temperature around 200°C. Figure 5.11 shows the XRD spectrum of sample HW165-21 after a 4-minute-long optical processing. The processing temperature was 200°C. It can be seen that, with Al present, even at temperature as low as 200C, the <111> and <220> peaks from Si can be observed. This result indicates that Al induced crystallization of Si can start at very low temperature (<200 °C) during optical processing. However, as can be seen in Figure 5.11, the crystallization is still very weak at this temperature.

The other thick samples were already partly crystallized during the deposition (because of longer deposition time and higher deposition temperature. It is reasonable to expect that the crystallization also starts at very low temperature, at least in the region close to Si-Al

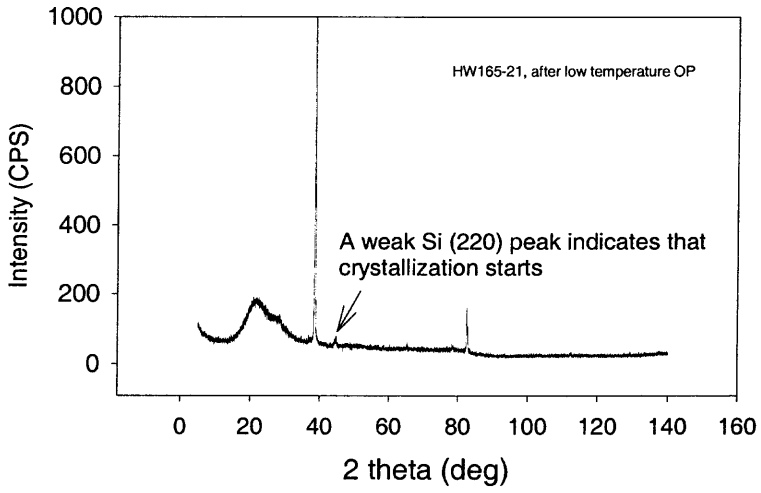

Figure 5.11. XRD spectrum of sample HW165-21 after a low temperature optical processing, the weak Si (220) peak shows that the crystallization starts during the processing.

5.4.3 The change of the peaks after processing

On the samples that are not crystallized before processing, obvious narrow peaks from crystallized Si can be observed in the XRD spectra after processing, as shown in the XRD spectra of HW165-11 before and after a 3-min-long, ~480°C optical processing(Figure 5.12 (a) and (b)). This indicates that the crystallization of a-Si can happen very easily in the sample structures and processing techniques that we are using.

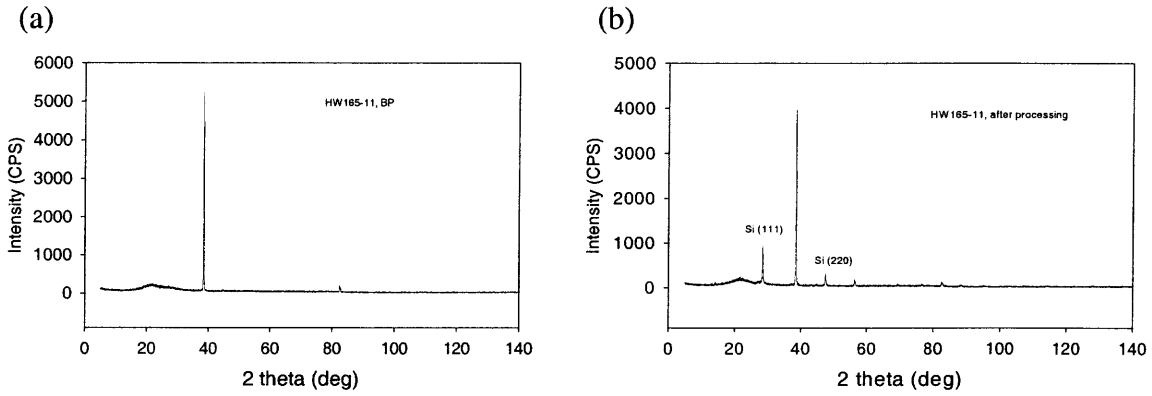

Figure 5.12. XRD spectrums of sample HW165-11, before (a) and after (b) processing. The apparent change of Si peak can be seen in these figures.

In the sample group HW54-XX, the samples are already strongly crystallized during deposition; thus no enhancement of crystallization can be seen in these samples, as can be seen in Figure 5.10 and 5.13, which show the XRD spectra of sample HW54-11 before and after processing respectively.

Figure 5.14 (a) and (b) show the XRD spectra of sample HW55-12 before and after a ~ 480 °C, 3 min processing. In this sample (also on the other samples in group HW55-xx), as been pointed out before, without processing, the crystallization was strongly textured in <220> direction. After processing, we can see that the intensity of the <111> peak becomes much stronger. This suggests that during processing, some new grains were formed, these grains can either be <111> textured or almost arbitrarily oriented (which is

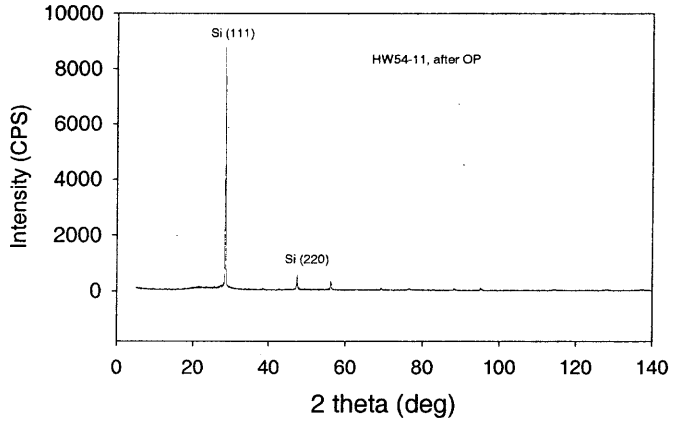

Figure 5.13. XRD spectrum of sample HW54-11 after optical processing. There are almost no changes in the peaks from the XRD spectrum of the unprocessed sample (Figure 5.10).

more likely, as we will see later). The intensity of <220> peak also increased more than 200% after processing. The increase of <220> peak could be from two sources: first, more <220>-oriented grains are created during processing; second, the original <220>-oriented grains were enlarged during processing. We believe that the second one is the major source of increasing in Si <220> peak because the newly-generated grains during processing are more likely to be arbitrarily-oriented, the amount of <220> oriented grains in them is not enough to increase the intensity of <220> peak by 200%.

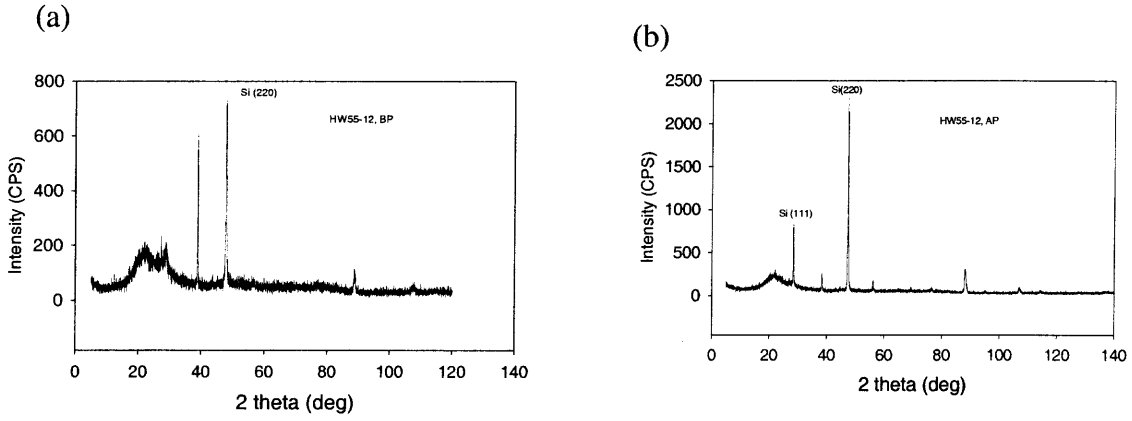

Figure 5.14. XRD spectrums of sample 55-12, before (a) and after (b) processing. The apparent change of Si (111) and Si (220) peaks can be seen in these figures.

As to the samples in sample groups HW16x-xxx, they are very weakly crystallized before processing, drastic changes can be observed in the XRD of these samples. In most cases, the relative intensities of the peaks show that the crystallization on the samples are almost arbitrarily distributed with a weak <111> texturing structure. The details of the change of crystalline in these samples will be discussed in the following section.

5.4.4. The effect of high temperatures

To compare influence of different processing temperatures on the samples, a set of 10-μm-thick samples are processed at 4 different temperature ranges but with about same time duration (3 minutes): 465~470 °C, 475~485 °C, 485~495 °C, 495~505 °C. Figures 5.15, 5.16, 5.17 and 5.18 compare the XRD spectra of these samples. It can be seen that in the XRD spectrum of HW161-12, not only the Si <220> and Si <111> peaks are much stronger than the other samples; several peaks form other Si crystalline structure also appear. This indicates that the crystallization is much stronger in this sample. A

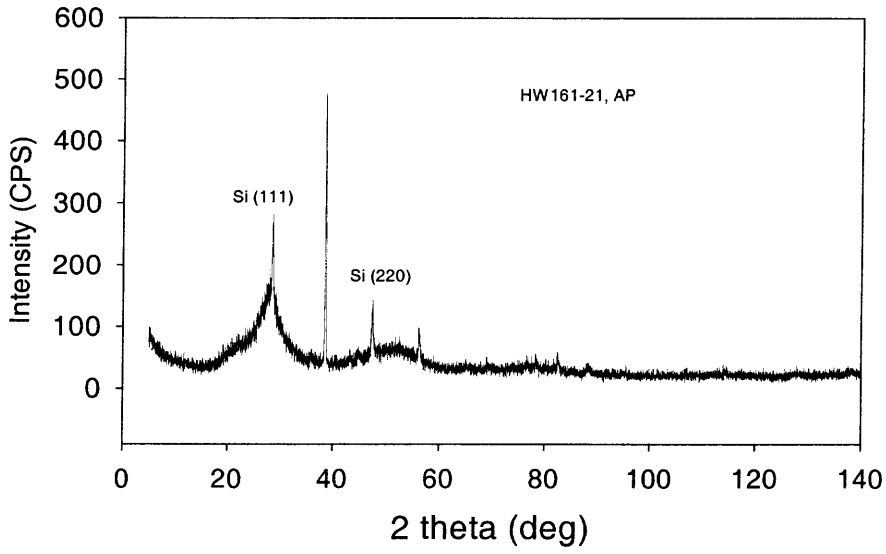

Figure 5.15. XRD spectrum of sample HW61-21, after processing

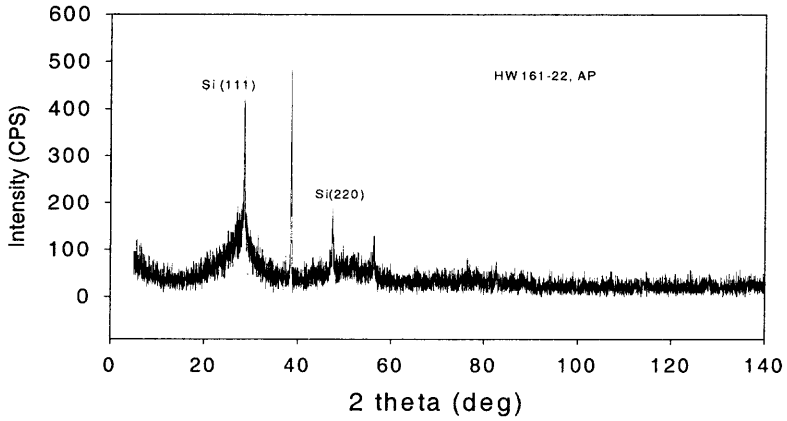

Figure 5.16. XRD spectrum of sample HW61-11, after processing

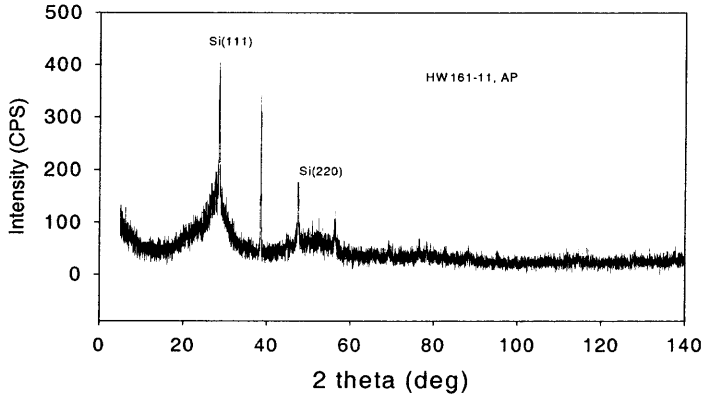

Figure 5.17. XRD spectrum of sample HW61-11, after processing

summary of processing temperature and the intensities of <111> and <220> peaks in XRD of these samples is listed in Table 5.3. From these figures and table, it can also be seen that the grains generated during processing is almost arbitrarily oriented. This is also true for other non-crystallized HW165X-XX samples.

Table 5.3 The intensities of different peaks in XRD spectrums of processed HW161-XX samples

Sample name	Processing temperature (°C)	Intensity of Al peak (CPS)	Intensity of Si<220> peak	Intensity of Si<111> peak
HW 161-21	458~463	470	143	285
HW 161-11	465~470	360	180	400
HW 161-22	485~490	470	193	421
HW 161-12	495~500	300	600	1240

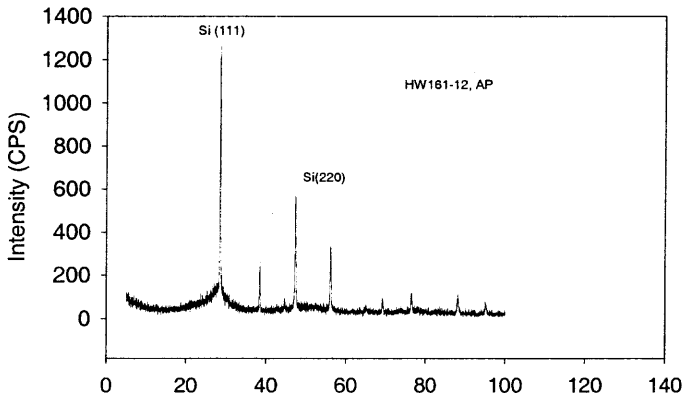

Figure 5.18. XRD spectrum of sample HW61-12, after processing

From these figures and table we can also see that when the processing temperature is around than 495~500C, the intensity of both peaks will increase dramatically (>300%), as summarized in Figure 5.19.

This conclusion suggests that there is a critical temperature, around 495~500 °C, in the process of Al-induced crystallization / grain enhancement. Above this temperature, the crystallization can be much stronger. Thinner samples (HW164-xx group, which have 6-μm-thick a-Si, and were processed at similar temperature ranges.) also show the same trend, as shown in Figures 5.20, 5.21 and 5.22 and in Table 5.4.

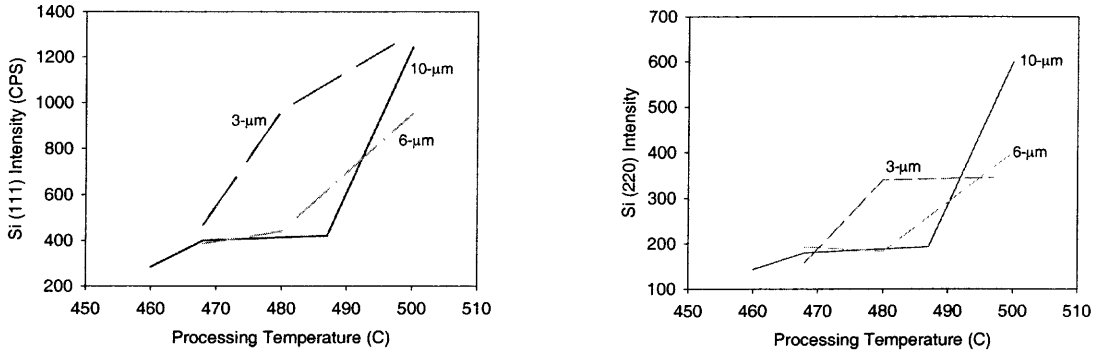

Figure 5.19. Summary of Si (111) and Si (220) peaks in the XRD spectrums of processed samples in HW16x-xx groups. The numbers inside the figure indicates the thickness of the sample referred to.

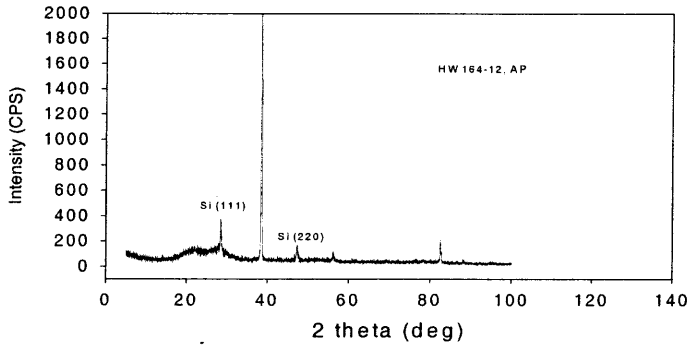

Figure 5.20. XRD spectrum of sample HW164-12, after processing

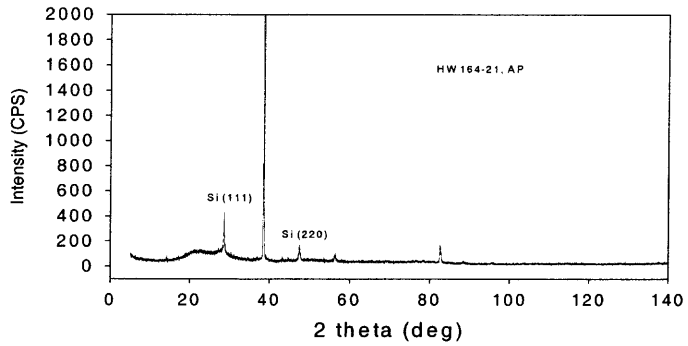

Figure 5.21. XRD spectrum of sample HW164-21, after processing

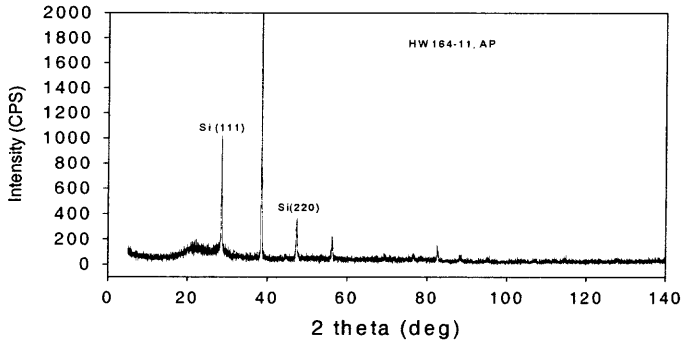

Figure 5.22. XRD spectrum of sample HW164-21, after processing

Table 5.4. Intensities of different peaks in XRD spectrums of processed HW164-XX samples

Sample name	Processing temperature (°C)	Intensity of Al peak (CPS)	Intensity of Si<220> peak	Intensity of Si<111> peak
HW 164-12	465~472	5100	193	386
HW 164-21	465~472	4800	183	440
HW 164-11	500~505	300	400	950

To find out the Al distributions in these samples processed under different conditions, SIMS measurement was done on processed HW164-xx group samples. The results are shown in Figures 5.23, 5.24 and 5.25. It can be seen that in sample 164-11, which was processed around 500C and strongly crystallized, Al goes much deeper into the Si layer. The Al:Si balance point (the point where the concentration of Al and Si are almost equal to each other) is also much closer to the Si surface.

Another observation can be made from the SIMS profile of the HW164-xx group samples

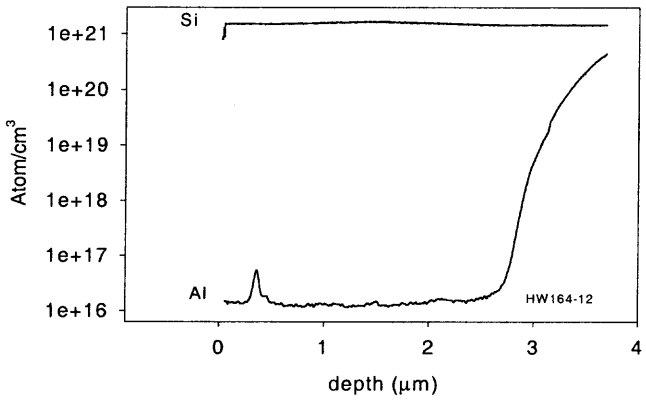

Figure 5.23. The SIMS profile shows the Si and Al distribution inside thin film of sample HW164-12, after processing

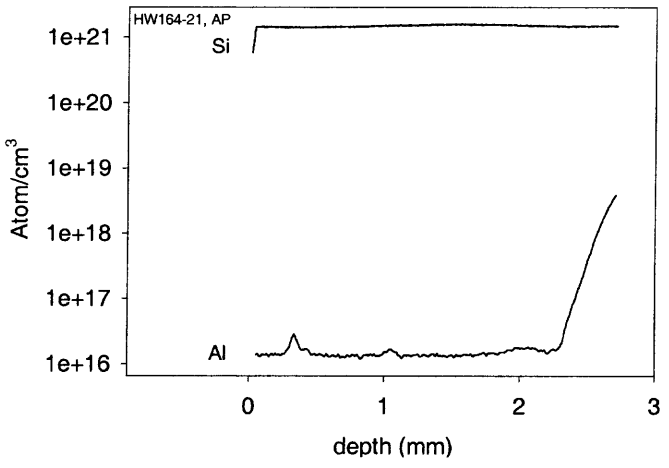

Figure 5.24. The SIMS profile shows the Si and Al distribution inside thin film of sample HW164-21, after processing

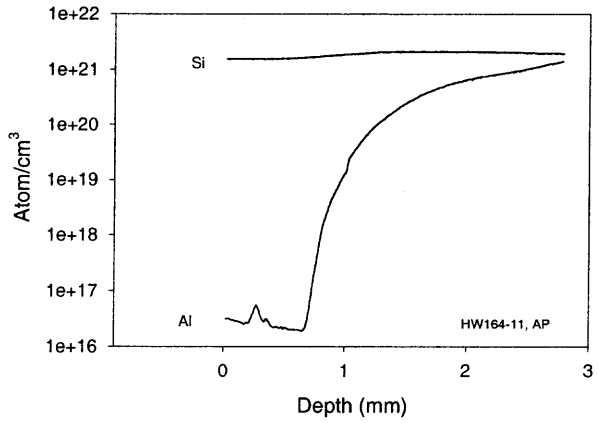

Figure 5.25. The SIMS profile shows the Si and Al distribution inside thin film of sample HW164-11, after processing

is that the strong intermixing and diffusion can exist at same time in the Al-Si system. In Figure 5.25, the distribution of the Al inside Si layer near the surface of the film follows the diffusion pattern, but it becomes almost constant when the depth becomes larger.

In sample group HW165-XX, the "turning point" of crystallization is not so obvious. Figures 5.26, 5.27 and 5.28 show the XRD spectra of this group of samples after processing. The peak intensities of these spectra are summarized in Table 5.5. It can be seen that the "turning point" of these samples (although not so apparent) is around 480

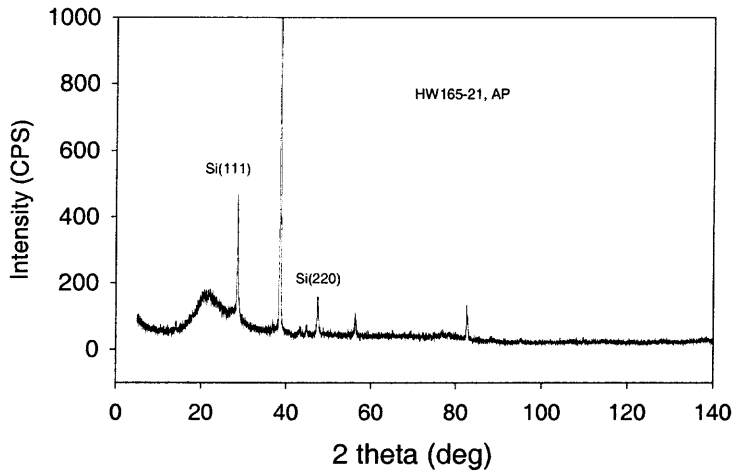

Figure 5.26. XRD spectrum of sample HW165-21, after processing

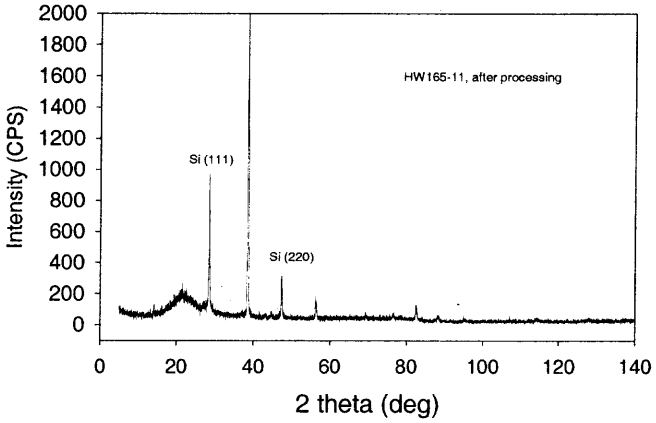

Figure 5.27. XRD spectrum of sample HW165-11, after processing

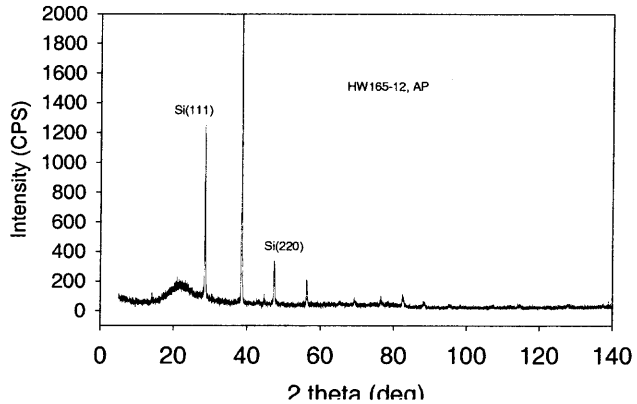

Figure 5.28. XRD spectrum of sample HW165-12, after processing

°C. SIMS result for sample HW165-21 (Figure 5.29) shows that the concentrations of Al and Si are close to each other (ratio of Al to Si is larger than 1:100) over the entire thickness of the film. This indicates that the crystallization in this sample was accompanied by strong mixing of Al and Si.

Table 5.5. Intensities of different peaks in XRD spectrums of processed HW165-XX samples

Sample name	Processing temperature (°C)	Intensity of Al peak (CPS)	Intensity of Si<220> peak	Intensity of Si<111> peak
HW 165-21	465~470	4700	159	468
HW 165-11	480~485	4000	340	966
HW 165-12	495~500	2950	345	1255

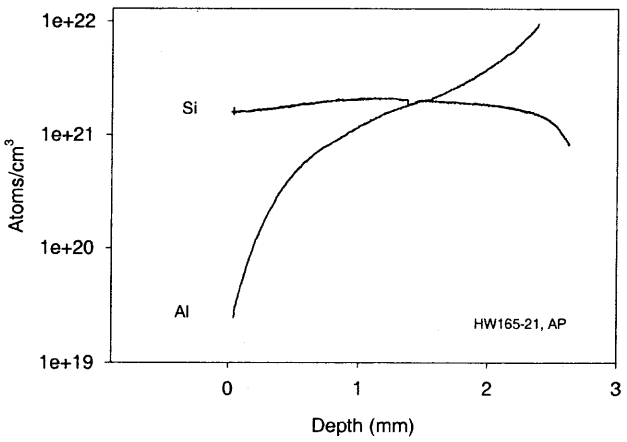

Figure 5.29. The SIMS profile shows the Si and Al distribution inside thin film of sample HW165-21, after processing

5.4.5 The effect of thin film quality

During the experiment, we found that no crystallization occurred on the PE1-XX group under the processing conditions considered in this study. However, after processing, reflectance measurement shows that the reflectivity in short wavelength range (<1 μm) of these samples increased to almost 0.70(Figure 5.30). Normally, the reflectivity of Si/Al sample (measured from Si side) in this wavelength range is only 0.30~0.40. The Al at the surface of the film may cause this high reflectivity. The image under optical microscope shows that these samples have a lot of "pinholes" in the film before processing (Figure 5.31). It is quite possible that the Al just migrated to the thin film surface because of these "pin-holes" instead of having crystallization reactions with the Si film. The reason why Al did not induce any crystallization in these samples is not clear.

5.4.6 Summary of experimental results

From the results described in the previous section, the following conclusions can be made:

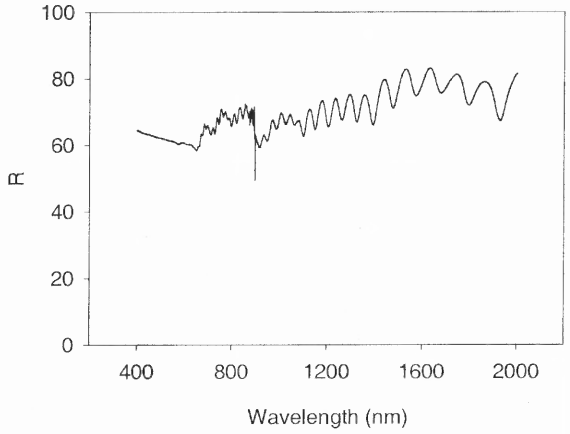

Figure 5.30. Measured reflectance spectrum of sample PE1-7, after optical processing

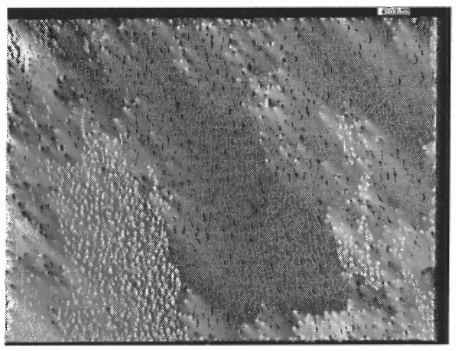

Figure 5.31. Image shows "pinholes" on the surface of PE1-xx group sample

1. In as-deposited samples, the crystallization will start when the deposition temperature is high and/or the deposition time is long enough. However, the as-deposited samples are usually not fully crystallized even if the deposition temperature is high (~500°C).
2. The crystallization will happen in thick film Si at fairly low temperatures (~200° C), even in the case that the total Al content is much less than that of the total Si in the whole sample. This starting temperature is close to the reported crystallization starting point of sub-micron-thick film Si samples. This low-temperature crystallization may occur in the neighboring region of Al-Si interface, which is relatively Al-rich. However, the crystallization at this point is very weak because the amount of crystallized Si is small and the grain size is tiny.

3. By comparing the samples deposited at different temperatures and processed at different conditions, it can be seen that although the crystallization does start at very low temperatures, strong crystallization happens at fairly high temperature. Crystallization becomes stronger with an increase in the processing temperature.

5.5 Discussion: The mechanisms involved in Al induced crystallization

Different mechanisms are proposed to explain Al induced low temperature crystallization of a-Si. Most authors believe that the strong mixing of Al and Si will induce the process of a-Si transforming into crystalline Si. Some representative mechanisms are:

1) Interstitial metal diffusion-induced reduction in activation energy of Si dissociation[90].

   The interstitial metal atoms in Si can change the Si-Si bonding from covalent to metallic at the interface and contribute to a large reduction of activation energy for c-Si formation.

2) The formation of Al silicide[91]

   Some authors believe that metal silicide plays a very important role in the crystallization procedure. The procedure can be written as:

   a-Si+Metal ->Metal silicide->poly-Si+metal

   Although the formation of silicide from other metals has been verified by many authors, so far only one author has reported the direct evidence of the formation of Al silicide during the Al+a-Si reactions. However, the reason why metal silicide can yield crystalline Si is still not clear.

3) Electric field enhanced inter-diffusion[92]

   Some authors think that the crystallization follows this route: prior to crystallization internal energy in the a-Si is released by the intermixing of metal and Si. The release

of internal energy results in bonding states in the *a* phase becoming like those in the *c* phase. The intermixing of some metals (include Al) will be enhanced because the relative eletronegativities between these metals and the Si is strong.

We do agree that strong Si-Al inter mixing will accelerate the crystallization process for a-Si. However, for thick samples, we believe there are other mechanisms involved in the process of Crystallization / Grain Enhancement. The arguments are:

a) The strong mixing (where the concentrations of Si and Al are close) may not happen over the entire depth of thick samples. In sub-micron samples, during the reaction, the Si and the Al can even penetrate each other, which is observed by most studies in this field. However, in thick samples, limited by the Al amount, the strong mixing will happen in only a limited region around the Al-Si interface. In our samples, the evidence of strong mixing, including the penetration or high concentration of Al inside Si film, do not show up over the entire thickness of the sample. As shown in the SIMS profile of samples HW164-12(Figure 5.23) and HW164-21(Figure 5.24), the concentration of Al in Si film is usually 2~4 orders of magnitude less than Si. However, the crystallization is still strong in these samples.

b) The electric field is not able to penetrate the intrinsic Si (which has very high ε) layer very deep. Thus, the electric field assisted Si-Al mixing inside thick Si film samples is not likely to happen.

c) Aluminum silicide is formed at 150°C to 250°C and deformed at 350°C. However, with our RTP-like processing, in which the time period in 150°C to 250°C temperature ranges is very short (less than 30s), it's unlikely that the silicide will be formed, at least the amount of silicide is very small. Therefore, the formation of

silicide may not be the necessary process in the Al induced crystallization. The silicide-involved theory also cannot explain as to why the crystallization becomes much stronger in thick samples when the temperature is higher than 500 °C

Based on these arguments, we propose our explanation of the Al induced crystallization and grain enhancement of thick samples as follows:

1. During the process of crystallization, two events occur: formation of tiny c-Si seeds (nucleation) and growth of c-Si grains (grain enhancement). Although the later can happen only after the first event, they can exist at same time and compete with each other during the Si-Al reaction. At low temperatures, the nucleation will be the major process. With long processing time, more a-Si will be transformed into crystalline Si (but in very tiny grains) by the reaction between a-Si and Al at low temperatures. However, nucleation can happen at only very close to the Si/Al interface, where strong intermixing is possible. At high temperatures, the grain enhancement process will dominate the process and help the enlargement of grains in the thick samples.
2. We believe that Al will not only accelerate the nucleation step; it will also help the grain enhancement step (but at much lower concentration) by diffusion into Si layer. Although this assumption cannot be verified, the grain boundary movement caused by interdiffusion of atoms (diffusion induced grain boundary movement, DIGM) in the binary system has been observed in some other materials. The SIMS profile of the crystallized sample shows that the Al atoms can diffuse into Si film deep during processing.
3. In higher temperature optical processing, although the monitored temperature is lower than the eutectic point of Al-Si system, the melting in the local regions close to Al-Si

interface may occur. This local melting will cause very strong crystallization at the interface area. This crystallization can be much stronger than the crystallization induced by Al-Si intermixing at solid state. The local melting at Si/Al interface is even more likely to happen in optical processing, in which the samples are heated from inside. This local melting could be the reason why the "turning point" of crystallization (Figure 5.19) exists because melting can only start at temperatures higher than some value.

4. In optical processing, the diffusion of Al in Si can be enhanced (compared to conventional thermal processing at same temperature). This will accelerate the crystallization procedures discussed above.

In summary, the crystalline / grain enhancement process in thick samples during optical processing can be formulated as follows:

The strong inter diffusion induced nucleation => Al-assited grain-growth / crystallization continues;

In high-temperature optical processing => local melt of interface => much stronger crystallization and grain/enhancement.

5.6 The primary device performance

Six processed thin film samples: HW161-21, HW161-12, HW161-22, HW165-11, HW54-22 and HW55-22 were used for device fabrication. The process of making the device has been described in the previous section. As has been illustrated in Figure 5.4, multiple devices are made on each thin film sample, these devices are characterized individually.

1. Voc analysis

Table 5.6 lists the Voc of devices on 4 samples. On the other 2 samples, no Voc was detected on any of the devices. Several observations can be made from table 5.6:

1) The highest Voc reached in these samples is 280 mV,
2) On average, the devices around the center area (35,22,21,32,52,53) have higher Voc than the other devices. However, the devices at the central area, which was processed relatively more strongly, do not have good output.
3) The output of the strongly crystallized samples, HW161-11 and HW 165-11, is not among the best results.

Table 5.6 Measured Voc of different devices on different samples

Sample name-> Deveice ID	HW161-21	HW161-12	HW161-22	HW165-11
11	0.030	0.211	0.081	0.007
12	0.199	0.066	0.076	0.001
13	0.130	0	0.280	0.006
14	0.006	0.159	0.210	0.004
21	0.202	0.004	0.251	0.002
22	0.001	0	0.268	0
31	0.015	0.180	0	0
32	0	0.196	0.232	0
33	0.050	0.002	0.016	0
34	0.180	0	0.007	0
35	0.220	0.271	0	0.003
36	0.01	0.002	0	0
41	0.090	0	--*	0
42	0.170	0.178	--	0.001
51	0	0.170	--	0
52	0.001	0	--	0
53	0	0.246	--	0
54	0.003	0.023	--	0.02
61	0	0	--	0.02
62	0.003	0	--	0.02

* the film was blown away during the p-n junction formation.

2. I-V characteristics of the device

Figure 5.32 shows the measured I-V characteristics of a device formed on HW161-22. It can be seen that the current measured on this device is very low, and this I-V curve shows that there is large series resistance existing in the device and measurement circuit[81]. The origin of these large series resistors can be:

1) The Al layer was totally mixed with Si; no pure Al was left under Si layer. Thus, the back contact resistance is much larger than that of the normal metal contact.
2) The probe used in measurement can also introduce large contact resistance in the circuit.
3) The surface of the p-type film may be oxidized during sample processing/handling.

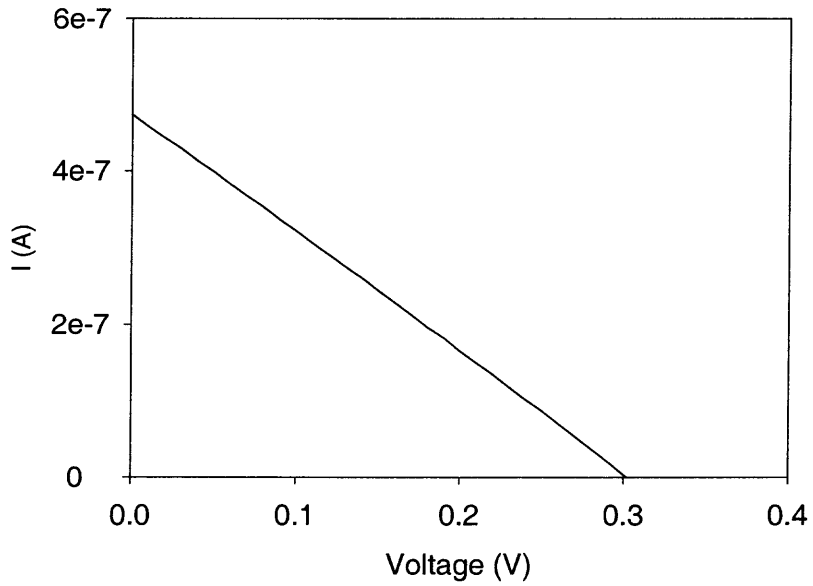

Figure 5.32. Measured I-V curve of device 35 on sample HW161-21.

CHAPTER 6

CONCLUSIONS AND FUTURE WORK

In this thesis, the following tasks have been accomplished:

1. The design of thin-film μc-Si solar cells

We have found that the proper thickness of the thin film μc-Si cell should be more than 10μm. The surface/interface configuration of the device should be front-side textured/back-side planar or double side textured.

A model and corresponding software were developed to calculate the minority carrier lifetime and I-V characteristics of large-area non-uniform materials /devices. We found that the effective lifetime of minority carriers measured in large-area materials may not be suitable for an indication of material quality. Small beam scanning method usually can provide precise information on minority carrier lifetime distribution in large-area materials. To get acceptable devices, the grain size of thin film μc-Si should be larger than 1 μm for 10-μm-thick Si film; the device performance will not be improved much when the grain size is larger than 20μm for thin film devices.

2. The Al induced crystallization was studied in detail

We have found that the Al involved crystallization can start at very low temperatures. The crystallization will become stronger with higher temperature. For thick samples (thickness~10μm), there is a turning point of the crystallization around 500C. For processing temperature higher than this point, the crystallization becomes much stronger. The reason for this behavior may be that the a-Si/Al interface is melted at this

temperature. It is found that crystallization of Si in a-Si/Al system is always accompanied by intermixing and diffusion of Al and Si. The crystallized materials always have the lattice structure of crystalline Si.

3. Primary solar cells were made based on the μc-Si crystallized using Al induced crystallization.

We have made some primary devices using the μc-Si film crystallized using optical processing. The highest open circuit voltage under AM1.5 is about 280mV. However, very weak current can be drawn from these devices. The reason for this is because of large series resistance existing in the system.

However, there is still a lot of work to be done to complete this project, such as:

1. The combination of optical software and electrical software

In the software developed in this thesis, the optics-related part (generation rate of carriers) was input by the user. However, in a real device, this part is decided by the structure and optical design of the cell. A complete PV modeling software should be able to calculate the optical properties of the device according to user designed structure combined with the electrical modeling module of the software. As mentioned in section 3.5, to get the "real" generation rate distribution inside the device, solving Maxwell equation is more practical than tracing the light inside the device. Since Maxwell equation is also a set of second order differential equations, the finite element engine developed in this thesis should be fairly easy to be extended for the solution of these equations.

2. The metal contact should be included in the device modeling

In the model developed, the metal contact is just a regular surface with finite surface recombination velocity. No front-contact pattern was considered. By using more complicated boundary configurations and boundary conditions, this problem can be solved.

3. More study on Al involved crystallization (AIC)

There are still many mysteries in the process of Al involved crystallization of a-Si, such as:

a). Is there a maximum grain size that this crystallization process can reach? Although in samples deposited at 600°C, no changes in XRD spectrum can be observed before and after processing, it may only be because the XRD will not show the difference when the grain size becomes larger.

b). From the current study, it can be seen that the mixing of Si/Al or diffusion of Al in Si always involves the process of crystallization. However, can we control the Al level inside the Si thin film while still obtain the benefits from the Al/a-Si reaction, such as high crystallization speed and low reaction temperature?

4. The device structure improvement

Although the open circuit voltage of the primary devices made in this thesis is acceptable though not satisfactory, the short circuit current is so low that these devices are almost not functional. As has been pointed out in section 5.6, the most possible reason is the back contacts of these devices which were damaged during processing. To solve this problem, a Ag layer is deposited in between Al and Cr, and, this should help to increase the conductivity of back contact.

On the other hand, if the Al concentration inside the Si layer cannot be controlled, since the Si/Al alloy formed using optical processing always has lattice structure of crystalline Si, we can always use this crystallized alloy layer as the seed layer for epi-growth of the Si layer to get high quality μc-Si film.

REFERENCES

[1] M. P. Thekaekara, *Data on Incident Solar Energy*, Suppl. Proc. 20th Annual Meeting Inst. Environ. Sci., (1974).

[2] Martin A. Green, *Solar Cells*, University of New South Wales, Sydney, Australia (1986).

[3] A. Goetzberger, Proceedings of Twenty-Sixth IEEE Photovoltaic Specialist Conference–1997, Anaheim, CA, p.1 (September, 1997).

[4] K. D. Smith, H. K. Gummel, J. D. Bode, D. B. Cuttriss, R.J. Nielsonand W. Rosennzweig, Bell System Tech. J., Vol. 42, p. 1765 (1963) .

[5] Swanson, Richard M., U.S. patent No. 4,234,352 (filed November 18, 1980).

[6] H.G. Rudenberger and B. Date, U.S. Patent 3,150,999 (filed February 17, 1961).

[7] Sopori, B. L.; Madjdpour, J.; von Roedern, B.; Chen, W.; Hegedus, S. S., Wagner, S., et al., eds. Amorphous and Microcrystalline Silicon Technology 1997: Proceedings of the Materials Research Society Symposium, 31 March - 4 April 1997, San Francisco, California. Materials Research Society Symposium Proceedings, Vol. 467. Pittsburgh, PA, Materials Research Society; p. 777 (1997).

[8] Martin A. Green, *Silicon Solar Cells-Advanced Principle & Practice,* Chapter 9, University of New South Wales, Sydney, Australia (1995).

[9] Bhushan Sopori, Jeff Alleman, Wei Chen, Teh Y. Tan, 6th Rapid thermal and integrated processing, Materials Research Society Symposium Proceedings, vol. 470, edited by Riley, T. J., p. 419(Apr. 1997).

[10] Chen, W., Sopori, B, Photovoltaics for the 21st Century, Proceedings of the Electrochemical Society International Symposium, Kapur, V. K., et al., eds., May 1999, Seattle, p. 145, Washington. Electrochemical Society Proceedings Vol. 99-11(1999).

[11] Bhushan Sopori, Laser Focus World, February 1998, p.159.

[12] Y. Zhao, X. Jiang, W. Wang, Z. Li, Y. Yu and X. Liao, Proceedings of Twenty Sixth IEEE Photovoltaic Specialist Conference –1997, p.569. (Anaheim, CA, September, 1997).

[13] C. Feldman, N. A. Blum, H. K. Charles, Tr and F. G. Satkiewia, J. Electron. Mater. , 7, p.309(1978).

[14] M.D. Efremov et al, Proc. SPIE, 2801, p. 263 (1996).

[15] M. Deguchi, S. Hamamoto, H. Sasaki, T. Ishihara, K. Sato and H. Namizaki, Technical Digest of the International PVSEC-5, p. 927, Kyoto, Japan, 1990.

[16] A. M. Barnet, I. W. Hall, W. A. Tiller, R. B. Hall and J. B. Mcneely, Proc. Of the 17th IEEE PV Specialists Conference, p. 747, Montreuxm, Switzerland (1984).

[17] W. J. P. van Enckevort and M. W. M. Graef, J. Electrochem. Soc. Solid State Sci. Technology, 128, 154 (1981).

[18] A. M. Barnet et al, Proc. Of the 10th EC Photovoltaic Colar Energy Conference, p. 302, Lisbon, Portugal(1991).

[19] D. J. Aiken, D. D. Smith, A. M. Barnett, presented on Twenty-fourth IEEE PVSC (1996).

[20] Yoshida, S., Hanada, T., Tanabe, S., Journal of Materials Science, 34, p. 267 (1999).

[21] Kobayashi, H. ; Mori, H. ; Ishida, T., Journal of Applied Physics v. 77 p. 1301 (1995).

[22] Rlf Brendel, in Proceedings of the 14th European Phovoltaic Solar Energy Conference(1995).

[23] K. J. Weber, K. Catchpole, M. Stocks, and A. W. Blakers, Proceedings of Twenty Sixth IEEE Photovoltaic Specialist Conference –1997, p.107(Anaheim, CA, September, 1997).

[24] T. Ishihara, S. Arimoto, H. Kumabe and T. Murotani, Progress in Photovoltaics: Research and Applications, vol. 3, p.105 (1995).

[25] A. Shah, J. Meier, P. Torres, U. Kroll, D. Fischer, N. Beck, N. Wyrsch, and H. Keppner, Proceedings of Twenty Sixth IEEE Photovoltaic Specialist Conference – 1997, p.569 (Anaheim, CA, September, 1997).

[26] C. Wang and G. Lucowsky, Proc. 21st IEEE PVSC, vol.2 , p. 1614 (1990).

[27] M. Faraj, S. Gokhale, S. M. Choudhari, and M. G. Takwale, Appl. Phys. Lett. 60, p. 3289 (1992)..

[28] Kenji Yamamoto, Takayuki Suzuki, Masashi Yoshimi and Akihiko Nakaijima, Jpn. J. Appl. Phys., vol.36, p. L569 (1997).

[29] Sopori, B. L.; Madjdpour, J.; von Roedern, B.; Chen, W.; Hegedus, S. S., Wagner, S., et al., eds. Amorphous and Microcrystalline Silicon Technology 1997: Materials Research Society Symposium Proceedings, Vol. 467. Pittsburgh, PA: Materials Research Society; p. 777 (1997).

[30] A. Geotzberger, Proc. 15th IEEE Photovoltaic Specialists Conference, p. 867, Orlando (1981).

[31] H. H. Li, J. Phys. Chem. Ref. Data 9, 561 (1980).

[32] G. E. Jellison, Jr. and F. A. Modine, J. Appl. Phys. Lett, 76, 3758 (1994).

[33] P. J. Timans, J. Appl. Phys., 74, 6353 (1993).

[34] K. Sato, Jap. J. Appl. Phys., 6, 339(1967).

[35] Bhushan Sopori, Wei Chen, Jamal Madjdpour, N. M. Ravindra, Journal of Electronic Materials. Vol. 28, p.1385 (1999).

[36] Bhushan Sopori, Jamal Madjdpour, Wei Chen, Proceeding of 2nd World Conference on Photovoltaic solar energy conversion, edited by Schmid, J., p. 152, Vienna, Austria (1998).

[37] H. F. Mataré, J. Appl. Phys. 56, p. 2605 (1984).

[38] Bhushan Sopori, Wei Chen, Karen Nemire, J. Gee, S. Ostapenko, S. Ashok, et al., eds. Defect and Impurity Engineered Semiconductors and Devices II, Materials Research Society Symposium Proceedings, Vol. 510, p. 505, San Francisco, CA (Apr., 1998).

[39] Volker Heine, Phys. Rev., 146, p.568 (1956).

[40] J. Bardeen, Phys. Rev., vol. 71, p.7171947).

[41] Carleton H. Seager, Ann. Rev. Mat. Sci., vol. 15, p.271 (1985).

[42] W. M. Johnson, D. K. Biegelsen, and M. D. Moyer, Appl. Phys. Lett., vol. 40, p. 882, (1982).

[43] C. R. M. Grovenor, J. Phys. C: Solid State Phys., 18, p. 4079–4119 (1985).

[44] Howard C. Card and Edwards S. Yang, IEEE Trans. Elec. Dev., vol. ED-24, p. 397 (1977).

[45] E. H. Rhoderick, J. Phys. D: Appl. Phys., vol. 3, p.1153 (1970).

[46] Voler Heine, Phys. Rev., vol. 138, p.A1689 (1965).

[47] Jerry G. Fossum and Fredrik A. Lindholm, IEEE Trans. Elec. Dev., vol. ED-27, p.692 (1980).

[48] Carleton H. Seager, J. Appl. Phys., vol. 52, 3960–3968 (1981).

[49] Dinesh Prasad Joshi and Devesh Prasad Bhatt, IEEE Trans. Elec. Dev., vol.37, 237–249(1990).

[50] Martin A. Green, J. Appl. Phys., vol. 80, 1515–1521(1996).

[51] S. M. Sze, *Physics of Semiconductor Devices*, 2nd edition, John Wiley & Sons, (1981).

[52] Alex Zunger, Ann. Rev. Mater. Sci., vol. 15, p.411 (1981).

[53] A. A. Istratov, H. Hieslmair and E. R. Weber, Appl. Phys. A, 69, p.13 (1999).

[54] H. Feichtinger, J. Waltl, A. Schwandtner, Solid State Commun., vol. 27, p. 867 (1978).

[55] H. Indusekhar, V. Kumar, Phys. Status Solidi A, vol. 95, p. 269 (1986).

[56] K. Wunstel, P. Wagner, Appl. Phys. A, vol. 27, p. 207 (1982).

[57] S. D. Brotherton, P. Bradlet, A. Gill, J. Appl. Phys., vol. 57, p.1941 (1985).

[58] J. Lagwoski, P. Edelman, A. M. Kontkiewicz, O. Milic, W. Henley, M. Dexter, L. Jastrzebski, A. M. Hoff, Appl. Phys. Lett. 63, p. 3043 (1993).

[59] G. Zoth, W. Berghola, J. Appl. Phys., vol. 67, p. 6764 (1990).

[60] S. K. Ghandhi and F. L. Thiel, Proc. IEEE 57, p. 1484 (1969).

[61] Y. Tokumaru, Jpn. J. Appl. Phys. 2, p. 542 (1963).

[62] W. B. Chua and K. Rose, J. Appl. Phys. 41, p. 2644 (1970).

[63] K. Graff and H. Pieper, in Semiconductor Silicon, edited by H. R. Huff, R. J. Kriegler, and Y. Takeishi (Electrochenical Society, Pennington, 1981), p.331. (1981).

[64] H. Indusekhar and V. Kumar, "Electrical properties of nikel-related deep levels in silicon", J. Appl. Phys. 61, p.1449(1987).

[65] S. J. Pearton and A. J. Tavendale, J. Appl. Phys. 54, p.1375 (1983).

[66] E. R. Weber, A. A. Istratov, S.A.Mchugo, H. Hieslmair, C. Flink, Recombination Lifetime Measurements in Silicon, ASTM STP 1340, edited by D.C.Gupta, F. R. Bacher, and W. M. Hughes, American Society for Testing and Materials, p. 18(1998).

[67] S. M. Sze and J. C. Trvin, Solid State Electron., 11, p.599 (1968).

[68] K. Graff and Pieper H., Semiconductor Silicon 1981, edited by H. R. Huff, R. J. Kriegler and Y. Takeishi, The Electrochem. Soc. 1981, p. 331 (1982).

[69] C. S. Fuller, J. A. Ditzenberger, N. B. Hannay, and E. Buehler, Phys. Rev. 96, p. 833 (1954).

[70] Y. Shimanuki, H. Furuya, I. Suzuki, and K. Maurai, Jpn. J. Apl. Phys. 24, p.1594 (1985).

[71] G. Fraundorf, P. Fraundorf, R. A. Craven, R. A. Frederick, J. Moody, and R. W. Shaw, J. Electrochem. Soc. 132, p.1710 (1985).

[72] K. Sakai, T. Yamagami, and K. Ojima, Appl. Phys. Lett. 74, p.1675 (1999).

[73] P. Wagner and J. Hage, Appl. Phys. A 49, p.123 (1989).

[74] H. Navarro, J. Griffin, J. Weber, and L. Genzel, Solid State Commun. 58, p.151 (1986).

[75] M. Suezawa, K. Sumino, H. Harada, and T. Abe, Jpn. J. Appl. Phys. Part 2, 25, p. L859 (1986).

[76] J. A. Griffin, H. Navarro, J. Webber, L. Genzel, J. T. Borenstein, J. W. Corbett, and L. C. Snyder, J. Phys C, 19, p. L579 (1986).

[77] D. Aberg, M. K. Linnarsson, B. G. Svensson, T. Hallberg, and J. L. Lindstrom, J. Appl. Phys. 85, p. 8054(1999).

[78] Guenther Zoth, ASTM STP 1340, edited by D.C.Gupta, F. R. Bacher, and W. M. Hughes, p. 328, American Society for Testing and Materials(1998).

[79] B. L. Sopori, W Chen, and Martha Symko, Recombination Lifetime Measurements in Silicon, ASTM STP 1340, edited by D.C.Gupta, F. R. Bacher, and W. M. Hughes, p. 328, American Society for Testing and Materials(1998).

[80] P. A. Basore, IEEE Trans. Electron Edevices, 37, p.337 (1990).

[81] J. J. Liou, *Advanced semiconductor device physics and modeling*, Artech House, Boston, MA(1994).

[82] M.S.Haque, H.A.Naseem, and W.D.Brown, J. Appl. Phys., 75, p.3928(1994).

[83] R. B. Bergmann et al, Semicond Sci. Technol., 12, p.224 (1997).

[84] T. Baba et al, Microcrystalline and Nanocrystalline Semiconductors, p. 895, Proc. of 1994 MRS Fall meeting, Symposium on Microcrystalline and Nanocrystalline Semiconductors, Pittsburgh, PA (1995).

[85] Seok-Woon Lee et al, IEEE Elec. Dev. Lett., 17(8), p. 407 (1996).

[86] T. Ishihara et al, Progress in Photovoltaics: Reasearch and Applications, 3, p.105 (1996).

[87] Min Cao et al, IEEE Trans. Elec. Dev. 43(4), p.561 (1996).

[88] M.D. Efremov et al, Proc. SPIE, 2801, p. 263 (1996).

[89] B. D. Cullity, *Elements of X-Ray Diffraction*, Addison-Wesley(1956).

[90] K. N. Tu, Appl. Phys. Lett. 27, p.221 (1975).

[91] M. S. Ashtikar and G. L. Sharma, "Silicide mediated low temperature crystallization of hydrogenated amorphous silicon in contact with aluminum", J. Appl. Phys. 78, p.913 (1995).

[92] Yuichi Masaki, Toshihiro Ogata, Hiroshi Ogawa and DavidI. Jones, "Kinetics of solid phase interaction between Al and a-Si:H", J. Appl. Phys. 76, p.5225 (1994).